Revisiting the Transonic Area Rule for Conceptual Aerodynamic Design

by

Francisco X. Armenta, Jr.

A Thesis Presented in Partial Fulfillment
of the Requirements for the Degree of
Master of Science

Approved April 2021 by the
Graduate Supervisory Committee:

Timothy Takahashi, Chair
Jeonglae Kim
Patrick Rodi

ARIZONA STATE UNIVERSITY

May 2021

ABSTRACT

The Transonic Area Rule, developed by Richard T. Whitcomb in the early 1950s, revolutionized high-speed flight because its insight allowed engineers to reduce and/or delay the transonic drag rise. To this day, it is the rationale behind "coke-bottle" sculpturing (indenting the aircraft fuselage at the wing-fuselage junction) to alter the cross-sectional area development of the body. According to Whitcomb, this indentation is meant to create a smoother transition of cross-sectional area development of the body and consequently would reduce the number of shocks on the body, their intensity, and their shock pattern complexity. Along with this, modeling of a geometry's transonic drag rise could be simplified by creating a comparable body of revolution with the same cross-sectional area development as the original geometry. Thus, the Transonic Area Rule has been advertised as an aerodynamic multitool.

This new work probes the underlying mechanics of the Transonic Area Rule and determines just how accurate it is in producing its advertised results. To accomplish this, several different wave-drag approximation methods were used to replicate and compare the results presented in Whitcomb's famous 1952 report[16]. These methods include EDET (Empirical Drag Estimation Technique)[4], D2500 (Harris Wave Drag program)[6], and CFD (Computational Fluid Dynamics) analysis through SU2[5]. Overall drag increment data was collected for comparison with Whitcomb's data. More in-depth analysis was then done on the flow conditions around the geometries using CFD solution plots.

After analysis of the collected data was performed, it was discovered that this data argued against Whitcomb's comparable body of revolution claim as no cases were

demonstrated where the comparable body and original body yielded similar drag rise characteristics. Along with this, shock structures and patterns were not simplified in two of the three cases observed and were instead complicated even further. The only exception to this observation was the swept wing, cylindrical body in which all shocks were virtually eliminated at all observed Mach numbers. For the reduced transonic drag rise claim, the data argued in favor of this as the drag rise was indeed reduced for the three observed geometries, but only for a limited Mach number range.

TABLE OF CONTENTS

Page

CHAPTER Page

APPENDIX Page

LIST OF TABLES

Table Page

LIST OF FIGURES

Figure Page

Figure Page

Figure Page

Figure Page

Figure Page

Figure Page

Figure Page

CHAPTER 1

INTRODUCTION

The Transonic Area Rule revolutionized high-speed flight since its development by Richard T. Whitcomb in the early 1950s[16]. The main purpose behind this method was to provide insight to reduce the transonic drag rise of an aircraft as it flies in the transonic regime (the Mach number range of approximately 0.8-1.2), thus allowing aircraft to travel at higher Mach numbers that it could not otherwise attain. Application of this area rule is shown in examples like that of the YF-102A[3] where, in conjunction with other propulsive system changes (larger engines, revised inlets), it became operable at supersonic conditions up to a verified speed of M~1.22.

When an aircraft moves through the air, it alters the flow passing over it. As the freestream flow approaches the aircraft it must either stop or change direction to pass over its surface. The points where the flow stops are high-static-pressure stagnation points. The flow that passes over the body, however, generally increases in speed often exceeding the freestream speed. When this occurs, the localized increase in speed is called a “super-velocity;” they cause a reduction in the local pressure of the fluid in comparison to the freestream pressure.

As the freestream Mach number increases, getting closer to the transonic regime, the local super-velocities over the surface of the aircraft may reach a point where they meet the speed of sound. When this occurs, the aircraft has reached its “critical Mach number.” Flight above this speed will develop regions of locally supersonic flow; which

may lead to the formation of shock waves where flow decelerates rapidly from supersonic speeds. This drastic change in flow is also associated with changes in pressures; projections of these pressure gradients in the fore-aft direction lead to what is known as “wave drag.” Note that not many but not all flows that decelerate from supersonic to subsonic speeds form a shock wave; a clever geometry can maximize the amount shock-free locally supersonic flow experienced by an aircraft.

It is this rapid increase in drag that Whitcomb sought to reduce and allow for a smoother transition to supersonic flight. He posited that the body of the aircraft would need to be made in such a way that the development of its cross-sectional area would need to be “smoother” to allow for this drag reduction. The claim was that this smoother cross-sectional area development would reduce the shock intensity and number of shocks experienced on an aircraft. In doing this, the aircraft would then experience a less drastic increase of wave drag[16].

Another claim of Whitcomb’s Transonic Area Rule is that two bodies of equivalent cross-sectional area development should exhibit the same transonic drag rise independent of where this area is placed (i.e. in the fuselage or wing sections)[16]. It is this concept that became the basis of the creation of wave drag estimation methods such as EDET and D2500 that will be discussed in further detail in this report.

Thus, it can be seen that the idea behind the “area rule” and the “equivalent body of revolution” has become the basis for many useful methods. This thesis asks “how accurate are Whitcomb’s claims.” More precisely, the purpose is to understand what is actually happening on the surface of aircraft with these rules applied. This thesis will

explore these concepts and develop more insight into how the Transonic Area Rule actually functions. It is with this in mind that this thesis then presents the following overarching questions:

1. Does the Transonic Area Rule achieve what it claims it does, and is it exact or approximate?
    a. Does an equivalent body of revolution produce the same transonic drag rise characteristics as the original wing-body combination?
    b. Does indenting the fuselage of a wing-body combination reduce the transonic drag rise experienced in a meaningful manner?
    c. Does indenting the fuselage of a wing-body combination reduce the number of shocks experienced and the intensity of them?
2. Are there any telltale signs of shock formation in subsonic solutions?
3. Are the shocks encountered able to be predicted by Küchemann's *CP** predictions?

This thesis will demonstrate that application of this area ruling to the original Whitcomb geometries does not yield the predicted results by using modern CFD and wave drag estimation methods. Along with this, it will explore the possibility of predicting shock formation by other means.

CHAPTER 2

PRIOR ART

In the field of aerodynamics, all concepts build on top of one another, gradually progressing the knowledge of fluid flow and how it can be used to our advantage. In the past there have been many new concepts added to this collection of knowledge in an attempt to simplify modeling, further understand flow behavior, or provide advantages to design. The Transonic Area Rule presented by Whitcomb is no different in this regard as it used many of the aerodynamics building blocks in its creation. It is for this reason that this report touches on all of the building blocks necessary to understand the depth of the Transonic Area Rule's functioning and the other concepts explored within this report.

a. Sources of Drag

At the very base level, drag can be defined as a force acting on an object in the opposite direction of its movement through a fluid. In the case of a stationary object within a fluid flow, drag is the force acting in the direction of the fluid flow on the object within it. The total drag experienced by this object can be broken up into several different contribution sources. At subcritical speeds, where there are no shock waves formed on the object, the sources of drag fall into two categories: viscous and inviscid. The viscous source of drag is called skin friction and relates to what can essentially be treated as "roughness" of the surface of the body. This "roughness," just as in any other source of friction, catches on the flow over the object's surface and distorts the flow so that it

experiences pressure and momentum losses downstream. The inviscid mechanisms that contribute to drag come from object geometry characteristics such as thickness, camber, and incidence. This kind of drag can be referred to as pressure drag and is generally found by integrating the pressures projected onto the object's surfaces and determining the net force acting in the opposite direction of movement through the fluid[1,9].

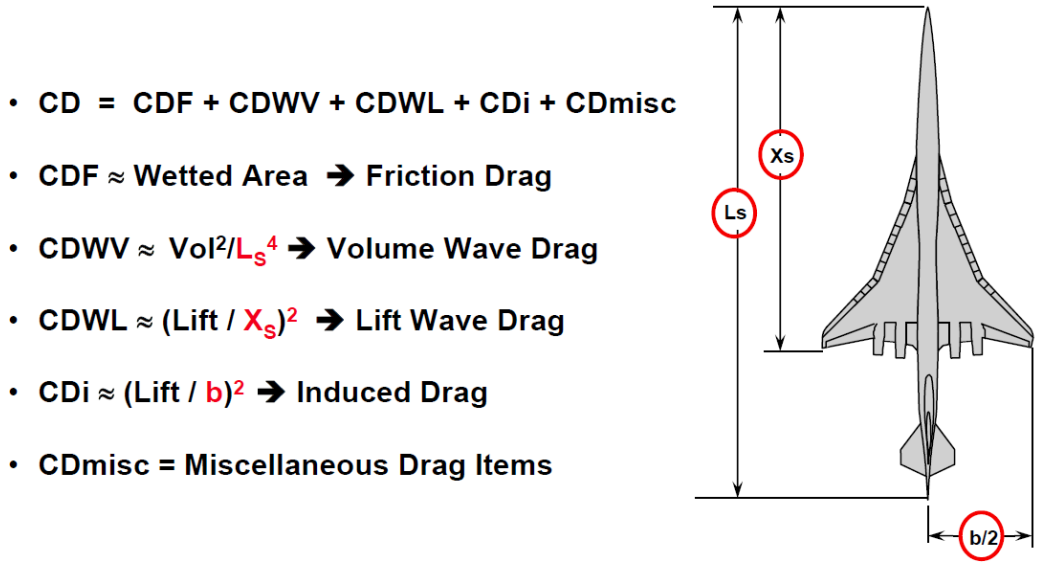

Figure 1. Drag Build-Up at Supersonic Speeds[9]

At supercritical speeds, however, the object travelling through the fluid has a possibility of developing shock waves on its surface which drastically alters flow conditions as the flow passes through it. Thus, these shock waves impact the pressure field around the object greatly, contributing more to the pressure drag referred to above. However, this extra drag contribution due to the presence of shock waves is typically referred to as "wave drag" and is the main quantity of interest in this report[1,9]. As shown

in Fig. (1) above, this can also be split into several different sources of contribution such as lift wave drag and volume wave drag. In the case of this report, only volume wave drag is taken into consideration as all models are at zero-lift angle of attacks.

b. Shock Waves

A shock wave is a very small region within a gas over which the flow conditions change drastically. The flow conditions that change are velocity, static pressure, total pressure, static temperature, and static density which are referred to as “jump conditions” in the NACA 1135 report. The types of shock waves demonstrated in NACA 1135 are normal shock waves, oblique shock waves, and the non-shock Prandtl-Meyer expansion fan.

A detached normal shock wave occurs when an inbound supersonic flow is forced to decelerate to subsonic speeds. This happens when the inbound flow suddenly encounters a “blunt” surface where the flow does not have enough time to easily travel around and must either slow to a stop (a stagnation point) or be slowed and travel around the surface at subsonic speeds. When this occurs, a detached normal shock develops forward of the blunt surface as is demonstrated in Fig. (2) below. These detached normal shocks may also occur in duct flows when supersonic inbound flows encounter “aerodynamically blunt” surfaces such as inlets lead to enforced subsonic conditions. This is demonstrated by the duct flow in Fig. (2) where the engine fan enforces a flow speed at a Mach number of approximately 0.3. A detached normal shock then develops forward of the engine inlet.

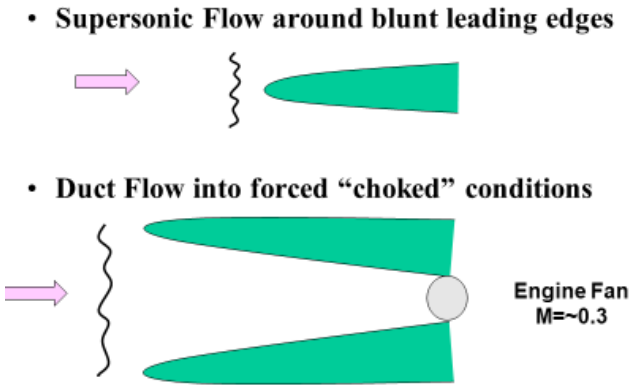

Figure 2. Development of Detached Normal Shock Waves Due to Aerodynamic Features

Normal shocks alter flow conditions in several ways as the flow passes over them, such as: increasing static pressure, increasing static temperature, increasing static density, and decreasing total pressure. The total temperature over a shock does not change, however, as the flow is compressed adiabatically over the shock (no heat is added or removed from the system). Along with this, the more supersonic the flow is before the shock, the more subsonic the flow is after the shock. This can be used to define the strength of a normal shock in comparison to others. These behaviors are shown in Fig. (3) below.

TABLE II.—SUPERSONIC FLOW

$\gamma = 7/5$

M or M_1	$\frac{p}{p_t}$	$\frac{\rho}{\rho_t}$	$\frac{T}{T_t}$	β	$\frac{q}{p_t}$	$\frac{A}{A_*}$	$\frac{V}{a_*}$	ν	μ	M_2	$\frac{p_2}{p_1}$	$\frac{\rho_2}{\rho_1}$	$\frac{T_2}{T_1}$	$\frac{p_{t_2}}{p_{t_1}}$	$\frac{p_t}{p_{t_1}}$
1.00	0.5283	0.6339	0.8333	0	0.3698	1.000	1.00000	0	90.00	1.000	1.000	1.000	1.000	1.000	0.5283
1.01	.5221	.6287	.8306	.1418	.3728	1.000	1.00831	.04473	81.93	.9901	1.023	1.017	1.007	1.000	.5221
1.02	.5160	.6234	.8278	.2010	.3758	1.000	1.01658	.1257	78.64	.9805	1.047	1.033	1.013	1.000	.5160
1.03	.5099	.6181	.8250	.2468	.3787	1.001	1.02481	.2294	76.14	.9712	1.071	1.050	1.020	1.000	.5100
1.04	.5039	.6129	.8222	.2857	.3815	1.001	1.03300	.3510	74.06	.9620	1.095	1.067	1.026	.9999	.5039
1.05	.4979	.6077	.8193	.3202	.3842	1.002	1.04114	.4874	72.25	.9531	1.120	1.084	1.033	.9999	.4980
1.06	.4919	.6024	.8165	.3516	.3869	1.003	1.04925	.6367	70.63	.9444	1.144	1.101	1.039	.9997	.4920
1.07	.4860	.5972	.8137	.3807	.3895	1.004	1.05731	.7973	69.16	.9360	1.169	1.118	1.046	.9996	.4861
1.08	.4800	.5920	.8108	.4079	.3919	1.005	1.06533	.9680	67.81	.9277	1.194	1.135	1.052	.9994	.4803
1.09	.4742	.5869	.8080	.4337	.3944	1.006	1.07331	1.148	66.55	.9196	1.219	1.152	1.059	.9992	.4746
1.10	.4684	.5817	.8052	.4583	.3967	1.008	1.08124	1.336	65.38	.9118	1.245	1.169	1.065	.9989	.4689
1.11	.4626	.5766	.8023	.4818	.3990	1.010	1.08913	1.532	64.28	.9041	1.271	1.186	1.071	.9986	.4632
1.12	.4568	.5714	.7994	.5044	.4011	1.011	1.09699	1.735	63.23	.8966	1.297	1.203	1.078	.9982	.4576
1.13	.4511	.5663	.7966	.5262	.4032	1.013	1.10479	1.944	62.25	.8892	1.323	1.221	1.084	.9978	.4521
1.14	.4455	.5612	.7937	.5474	.4052	1.015	1.11256	2.160	61.31	.8820	1.350	1.238	1.090	.9973	.4467
1.15	.4398	.5562	.7908	.5679	.4072	1.017	1.12029	2.381	60.41	.8750	1.376	1.255	1.097	.9967	.4413
1.16	.4343	.5511	.7879	.5879	.4090	1.020	1.12797	2.607	59.55	.8682	1.403	1.272	1.103	.9961	.4360
1.17	.4287	.5461	.7851	.6074	.4108	1.022	1.13561	2.839	58.73	.8615	1.430	1.290	1.109	.9953	.4307
1.18	.4232	.5411	.7822	.6264	.4125	1.025	1.14321	3.074	57.94	.8549	1.458	1.307	1.115	.9946	.4255
1.19	.4178	.5361	.7793	.6451	.4141	1.026	1.15077	3.314	57.18	.8485	1.485	1.324	1.122	.9937	.4204
1.20	.4124	.5311	.7764	.6633	.4157	1.030	1.15828	3.558	56.44	.8422	1.513	1.342	1.128	.9928	.4154
1.21	.4070	.5262	.7735	.6812	.4171	1.033	1.16575	3.806	55.74	.8360	1.541	1.359	1.134	.9918	.4104
1.22	.4017	.5213	.7706	.6989	.4185	1.037	1.17319	4.057	55.05	.8300	1.570	1.376	1.141	.9907	.4055
1.23	.3964	.5164	.7677	.7162	.4198	1.040	1.18057	4.312	54.39	.8241	1.598	1.394	1.147	.9896	.4006
1.24	.3912	.5115	.7648	.7332	.4211	1.043	1.18792	4.569	53.75	.8183	1.627	1.411	1.153	.9884	.3958

Figure 3. Normal Shock Table[1]

Oblique shock waves occur when an inbound supersonic flow is forced to turn outward and compress, as is demonstrated in Fig. (4). In this figure, the delta angle refers to the turning angle of the flow and the theta angle refers to the shock angle. On an aircraft body the flow can be forced to turn by the geometric features of it such as the fuselage, wing, or many others. Unlike the normal shocks shown in Fig. (2), oblique shock waves will typically remain attached to the feature causing deflection. These types of shocks behave similarly to the normal shocks in that they cause sharp changes in the flow conditions, but there are two directions in which these changes can go. First, there are weak oblique shock waves, which are more common, over which the supersonic inbound flow becomes less supersonic. The more supersonic the inbound flow is, the less supersonic the flow downstream of the shock is. Then there are strong oblique shock waves over which the supersonic inbound flow becomes subsonic (similar to a normal shock). These solutions are typically plotted as shown in Fig. (5) below.

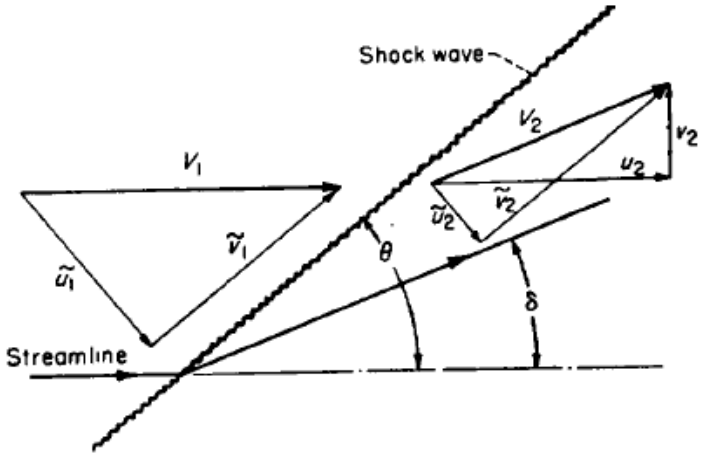

Figure 4. Development of an Oblique Shock Wave due to Turning of a Supersonic Flow[1]

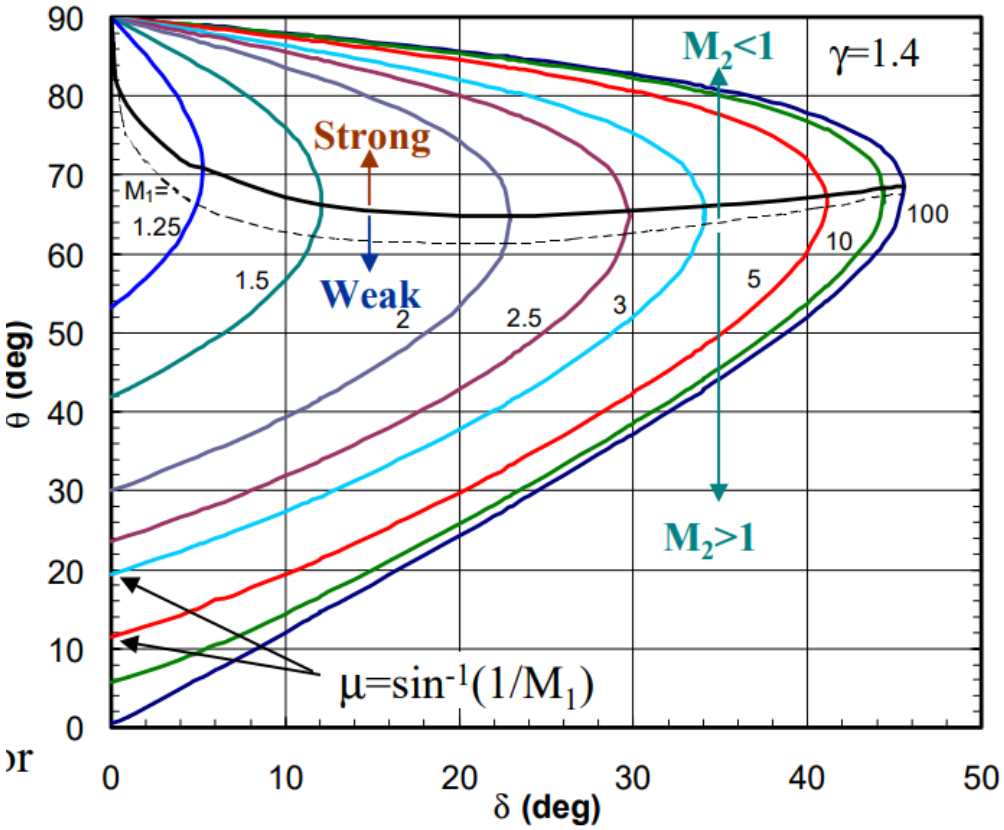

Figure 5. Strong vs. Weak Oblique Shock Waves

In Fig. (5) above, there is the mu equation which refers to the Mach cone angle which is modeled by the inverse sine of the reciprocal of the upstream (freestream) Mach number. Typically, it is the weak oblique shock waves that have shock angles that coincide with the expected Mach cone angle. Strong oblique shock waves, however, have greater shock angles that can reach up to 90 degrees (i.e. a normal shock). In either of these cases, however, the same flow condition changes occur: the static pressure rises, the static density rises, the static temperature rises, the total temperature remains unchanged, and the total pressure decreases. Another interesting aspect of these oblique shock waves is when supersonic flow is made to turn around a 3-D object such as a cone. In this case,

as is stated in NACA 1135, “if the bow shock wave is attached to an uninclined circular cone, the shock wave too has the form of a circular cone[1].” The behavior of these shocks is also governed by the oblique-shock relations. This is of particular interest for cases of aircraft with fuselages that have near circular cone noses.

Finally, though the Prandtl-Meyer Expansion fan is not a shock, it is a concept that is important for understanding the behavior of supersonic flows. These occur when an inbound supersonic flow is forced to turn inward around a sharp corner and expand isentropically, as is shown in Fig. (6) below. A feature that may cause this to occur is a fuselage boat-tail. These expansion fans alter flow conditions by: increasing the speed (i.e. downstream Mach number is greater than upstream), decreasing the static pressure (due to expansion), decreasing the static density, but the total pressure remains constant due to the isentropic nature of expansion fans[1].

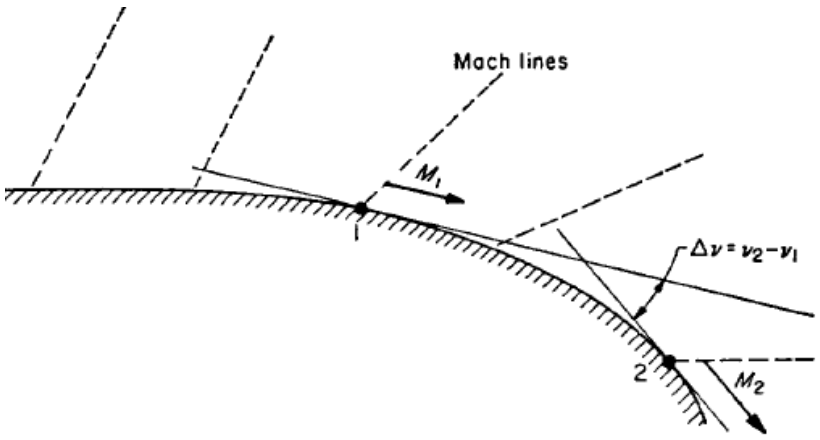

Figure 6. Prandtl-Meyer Expansion Shock Waves[1]

c. Flows That Trigger Shock Waves

In the previous section there was discussion of general types of flows that could trigger shock waves such as turning supersonic inbound flows outward (causing an oblique shock) or inward (causing a Prandtl-Meyer expansion shock). However, there are other features used on aircraft that can develop shock waves.

In Fig. (7) below, shock development is shown on the surface of a 2-D airfoil as Mach number is increased. In column b of this figure, there are plots of the ratio of local velocity to speed of sound vs the chordwise location on the airfoil. The O on these plots refers to the upper surface of the airfoil and the U refers to the lower surface. In the Mach 0.75 case, it can be seen that the surfaces both create super-velocities along their surfaces (local flow speeds greater than freestream) with the upper surface having some supersonic flow and smoothly becoming subsonic once more with no shock being created. In the Mach 0.81 solution a shock appears at the aft portion of the upper surface correlating with a local Mach number of approximately 1.2. This is demonstrated in the velocity plot as there is a rapid reduction in the local velocity to subsonic. As the freestream Mach number continues to increase, there is eventually shocks on both surfaces that gradually move aft to the tail of the airfoil. Once the shock waves have moved this far back, the local velocity over the whole surface of the airfoil is supersonic. Finally, at the Mach 1.4 case, a bow shock (detached normal shock) is developed forward of the nose of the airfoil with oblique shocks at the trailing edge of the airfoil and nearly all the airfoil surface having supersonic flow over it. Thus, it can be seen that 2-D airfoils

having area that blocks the inbound flow causes local velocities on the surface to increase beyond that of the freestream until shocks are developed.

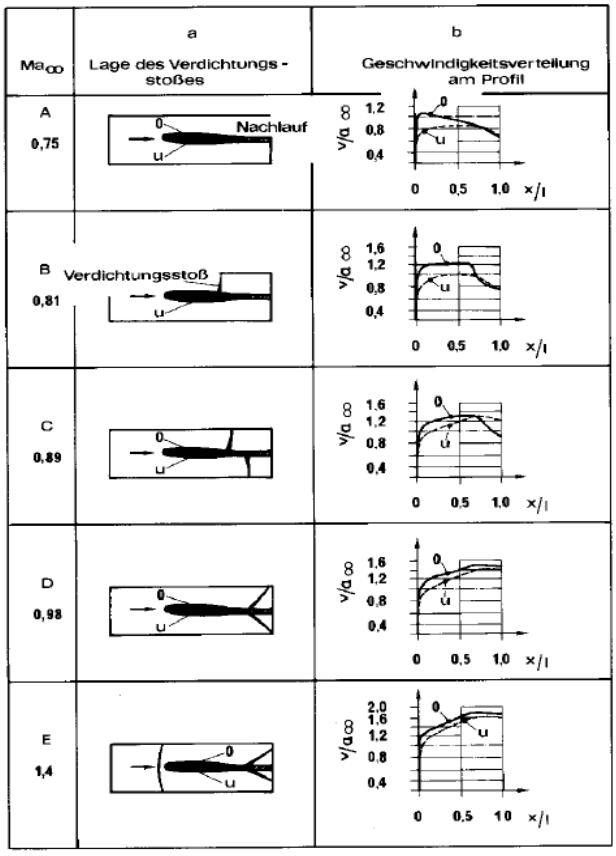

Figure 7. Shock Wave Development on a 2-D Airfoil[12]

If instead the case of a 3-D finite swept wing such as that shown in Fig. (8) below is considered, more complex behavior comes to light. In this case, Schlichting[12] discusses the correlation between Mach cone angles (a table showing the relation between Mach cone angles and freestream Mach number is shown in Fig. (8) below), leading and trailing edge conditions, and the types of shocks that coincide with these conditions. Schlichting shows that if the leading edge of a finite 3-D wing is swept far back enough

behind the Mach line and the trailing edge is also swept behind the Mach line, both edges would be subsonic with a shock developing toward the trailing edge. This shock would then coincide with the Mach line angle as is shown in case a in Fig. (8) below. In case b, there is a subsonic leading edge (behind the Mach line) and a supersonic trailing edge (ahead of the Mach line), where there appears to be no shock developing on the wing surface. Finally, case c shows a supersonic leading edge (not swept far enough to be behind the Mach line) and a supersonic trailing edge as well. In this case, a shock occurs toward the leading edge and coincides with the Mach line again[12]. Thus, 3-D wings with sweep complicate the development of shock waves even further as geometries can be adjusted to help avoid development of shocks even when freestream flow speeds exceed the speed of sound.

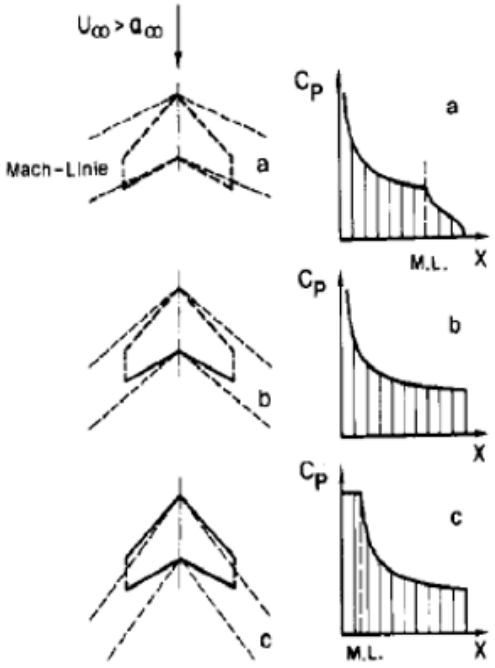

Figure 8. Shock Wave Development on a 3-D Swept Wing[12]

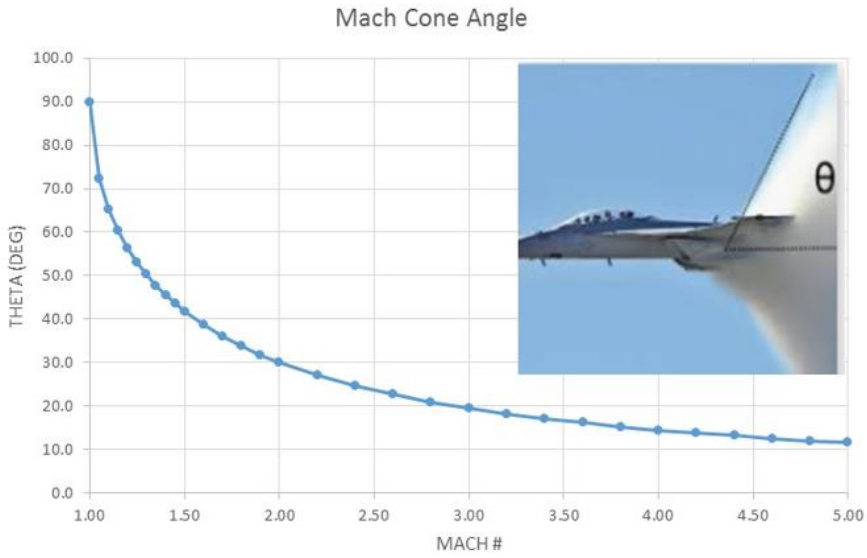

Figure 9. Mach Cone Angle as a Function of Freestream Mach Number

d. Critical Pressure Coefficient Predictions

It is beneficial to understand what aircraft geometries would cause development of shocks so that a real predictive capability may be developed. By understanding when a shock would occur for a given geometry at a given cruise Mach number, one could reshape the design of the aircraft to reduce the possibility of shock development and effectively increase the capable cruise Mach number. To obtain this understanding, von Karman[15] began by observing the concept of a "Critical Mach number." This critical Mach number would refer to the freestream Mach number that would coincide with the first occurrence of locally sonic flow on an object surface. Thus, at a certain Mach number, the object being observed would create local super-velocities that reach a Mach number of 1. The idea would then become that one could calculate the pressure coefficient that would coincide with the locally sonic flow. Eventually, further

development of this concept would lead to the critical pressure coefficient equation for 2-D flow:

$$C_p^* = \frac{p - p_0}{q} = \frac{2}{\gamma M_\infty^2}\left(\left(\frac{2}{\gamma+1}\right)^{\frac{\gamma}{\gamma-1}}\left(1 + \frac{\gamma-1}{2}M_\infty^2\right)^{\frac{\gamma}{\gamma-1}} - 1\right) \quad (1)$$

Thus, for 2-D flow, one could predict the onset of locally sonic flow by using this equation. The trend of this equation is shown in Fig. (10) below and shows that as the freestream Mach number is increased, the critical pressure coefficient value decreases until it reaches a value of 0 at a Mach number of 1. For 3-D flow, however, Küchemann explored the concept of how to predict the critical pressure coefficient of an infinitely long swept wing[8]. He developed his idea for an equation that would accurately predict this, and it is confirmed to be accurate by Kirkman and Takahashi[7]. This equation the becomes:

$$C_p^* = \frac{2}{\gamma M_\infty^2}\left(\left(\frac{2}{\gamma+1}\right)^{\frac{\gamma}{\gamma-1}}\left(1 + \frac{\gamma-1}{2}M_\infty^2\cos^2(\Lambda)\right)^{\frac{\gamma}{\gamma-1}} - 1\right) \quad (2)$$

This equation is modeled in Fig. (11) below and shows that the original critical pressure coefficient equation is "corrected" by the cosine of the wing sweep angle. This equation is meant to be an approximation of when a shock might occur due to a local pressure coefficient becoming more negative than the critical pressure coefficient. Thus, this does not guarantee a shock wave will form exactly once this pressure coefficient is reached on the surface of the observed object.

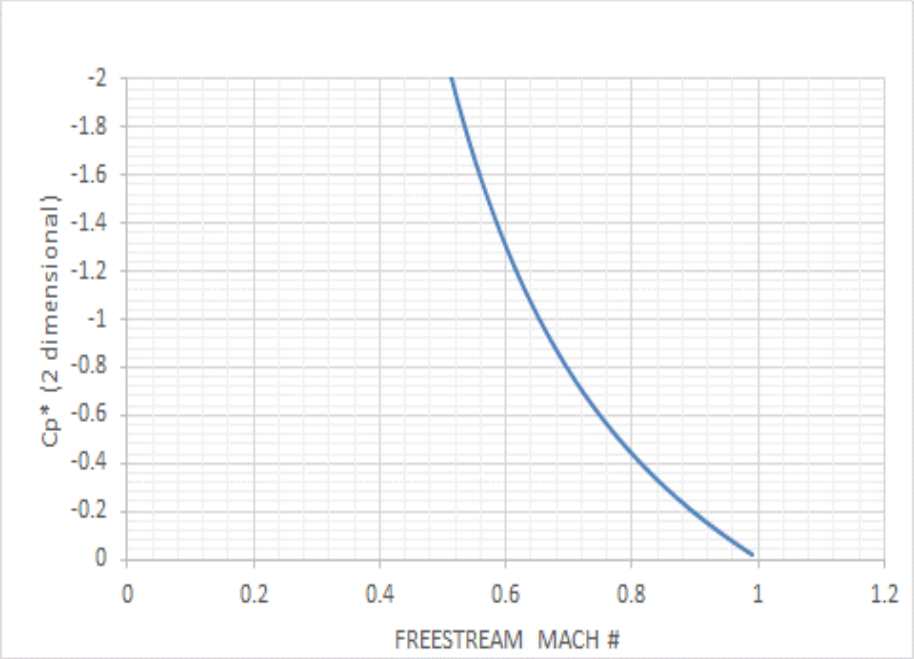

Figure 10. *Cp** for 2-D Flow

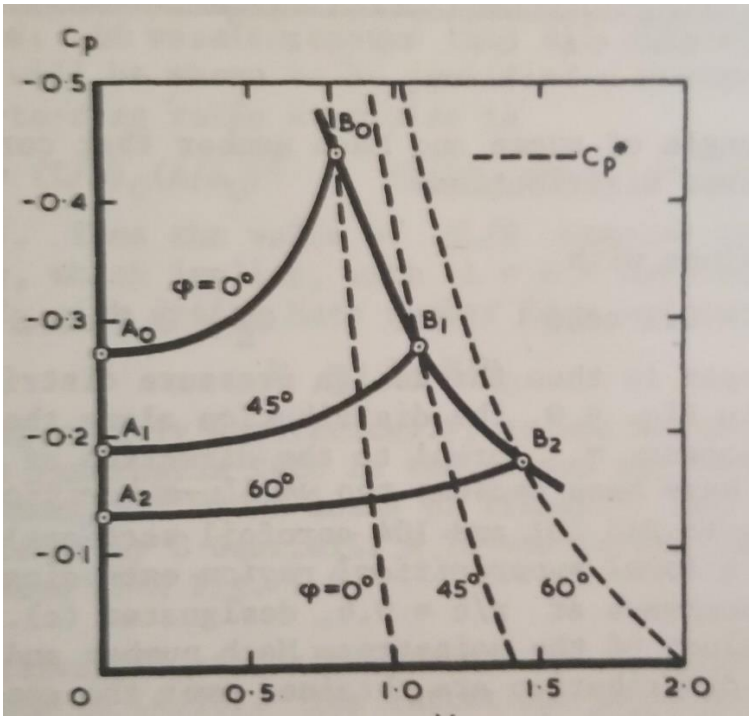

Figure 11. *Cp** for Infinite Swept Wings – after Küchemann[8]

e. The Transonic Area Rule

The basic idea behind the Transonic Area Rule is that an aircraft can avoid premature transonic drag rise, or at least delay it, by indented the body at the wing-body junction to create a body having equivalent cross-sectional area development to the original body. Another claim of this ruling is that the wing-body combination being observed has the same transonic drag rise characteristics as a body of equivalent cross-sectional area development, or a comparable body of revolution in this case[16]. To create a comparable body of revolution, cutting planes perpendicular to the flow of a zero-angle of attack body are passed through the areas where a wing is present. The cross-sectional area of the wing is then conglomerated into the body as a circular cross-section of greater area. This is demonstrated in Fig. (12) below where the original body on the left becomes the comparable body of revolution on the left due to the added cross-sectional area of the wings. To indent the bodies, the opposite process is done. Instead, the added cross-sectional area from the wings are subtracted from the body, leaving circular cross-sections with less area. This is shown in Fig. (13) below and the idea would be that the dark blue cross-sectional area in Fig. (14) would be equal to the cross-sectional area of the teal section. So, then the example shown for the unswept wing case shows that the comparable body on the right of Fig. (12) has the same cross-sectional area development as the indented body geometry on the right of Fig. (13). It should be noted, however, that though this is how the Transonic Area Rule is intended to work for indentation, it is not necessarily the "ideal" body for reduced wave drag. For the highest possible reduction in transonic drag rise, one would instead indent the body in such a way that the comparable

body of revolution from this new geometry would yield the Sears-Haack body (the commonly known aerodynamic shape for the lowest theoretical wave drag in supersonic flow).

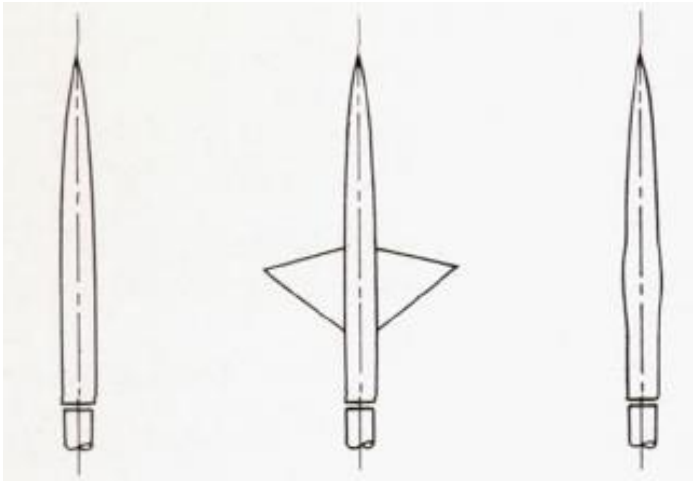

Figure 12. Unswept Wing, Cylindrical Body and Comparable Body Geometries[16]

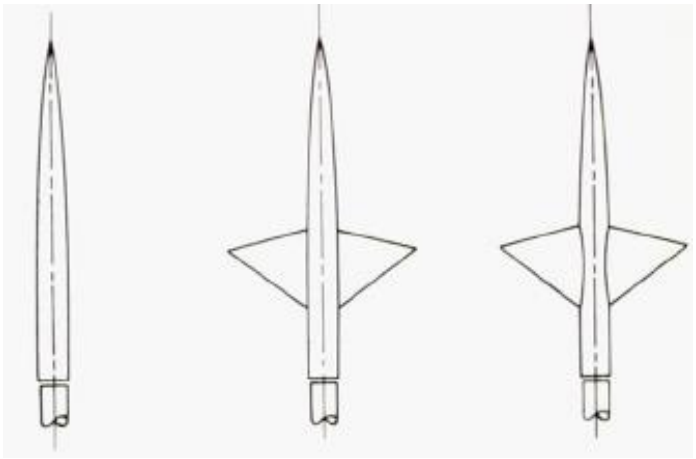

Figure 13. Unswept Wing, Cylindrical Body and Indented Body Geometries[16]

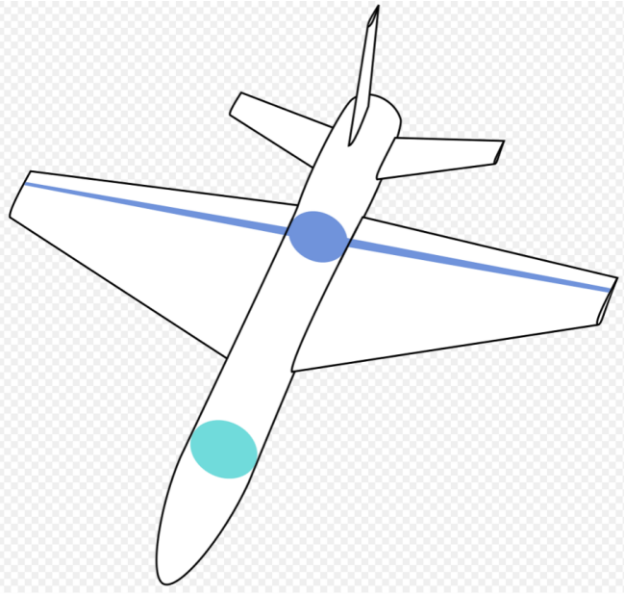

Figure 14. Transonic Area Rule[2]

The idea is then that the indented body creates a geometry with the required wing characteristics, but with a smoother transition cross-sectional area development. By doing this, Whitcomb then claims that the transonic drag rise of the geometry will now be reduced compared to the original body.

CHAPTER 3

TOOLS & METHODS FOR COMPUTATIONAL FLUID DYNAMICS

To obtain a more in-depth look into the shock wave patterns described by the area rule, 3-D versions of the original geometries included in NACA Report 1273 (Whitcomb's 1952 report introducing the Transonic Area Rule) were mocked up and CFD solutions were obtained for them. This section then begins with the descriptions of these geometries provided in the report.

a. Whitcomb's 1952 Geometries

To demonstrate the application of the Transonic Area Rule, Whitcomb created four base wing-body geometries which he named: 1) Unswept wing with cylindrical body; 2) Delta wing with cylindrical body; 3) Swept wing with cylindrical body; and 4) Swept wing with a curved body. Whitcomb described each loft with a dimensioned planform sketch, wing airfoil section descriptions and fuselage ordinates. The geometry planforms are as shown in Fig. (15) and Fig. (16) below, where all dimensions are in-in.

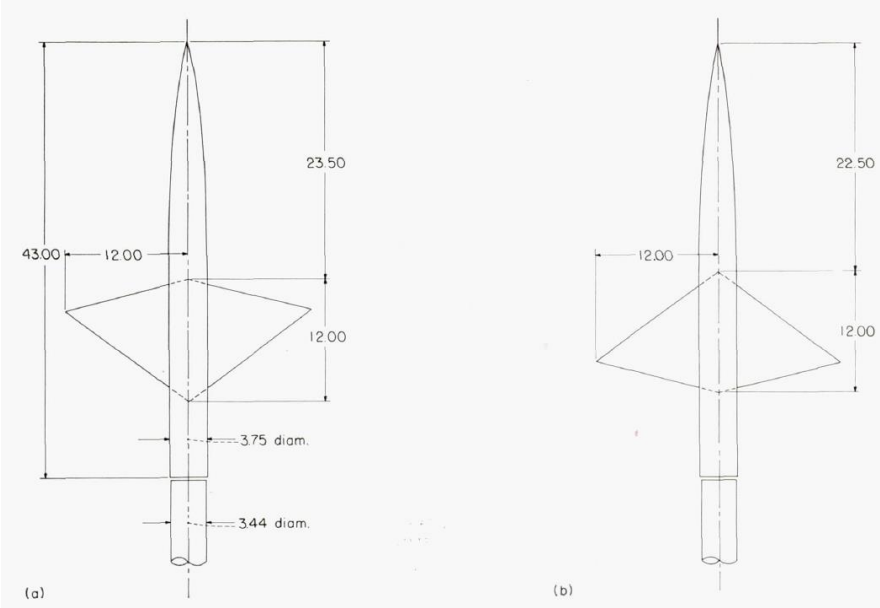

Figure 15. Planform Descriptions: Unswept Wing, Cylindrical Body (left) & Delta Wing, Cylindrical Body (right).[16]

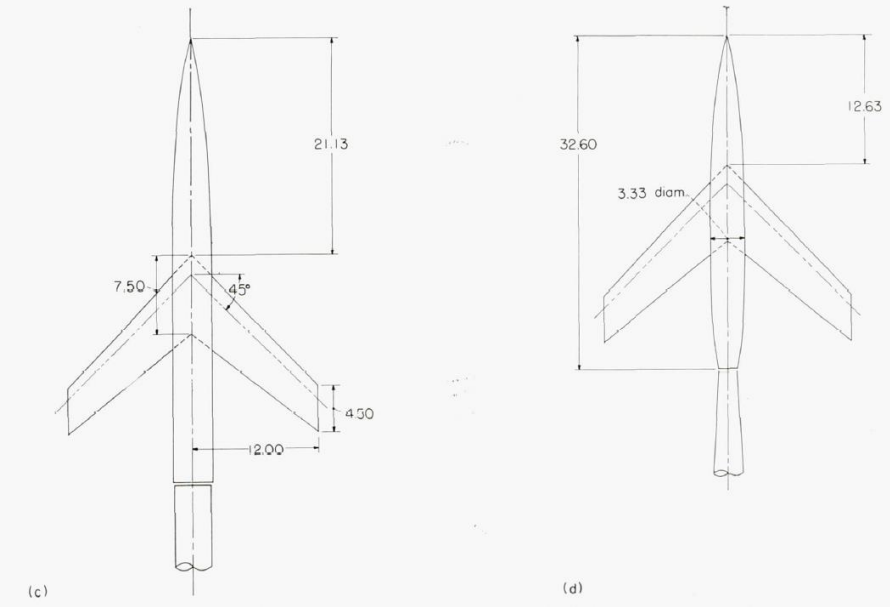

Figure 16. Planform Description: Swept Wing, Cylindrical Body (left) & Swept Wing, Curved Body (right).[16]

For the unswept wing, Whitcomb described it as having a "0-degree sweep of the quarter-chord line, an aspect ratio of 4.0, and a taper ratio of 0. The streamwise sections of the wing are symmetrical, are 4 percent thick, and consist of circular arcs with the maximum thickness at the 40-percent-chord stations[16]."

The delta wing is described simply as the reverse of the unswept wing "so that the 75-percent-chord line is unswept… The leading-edge sweep of this wing is 37 degrees[16]."

Finally, the swept wing was described as "a wing which has 45-degree sweep of the quarter-chord line, an aspect ratio of 4.0, a taper ratio of 0.6, and an NACA 65A006 airfoil section parallel to the airstream[16]."

Three types of bodies are then described by several tables of ordinates: the basic bodies (cylindrical and curved), comparable bodies of revolution (one for each of the four base geometries), and indented bodies (only bodies a-c in Fig. (15) and Fig. (16) above get these). These tables are included in Appendix A at the end of this report.

b. Modeling Geometries in SolidWorks

With this information, the modeling process began with a need to create 3-D models to represent the given geometries. To obtain the bodies for each of the geometries, the ordinate data was inserted into SolidWorks as a polyline and revolved. As for the wings, wing sections were created at the root and tip and material was extruded between the two sections. Once these were completed, they were combined in SolidWorks Assembly at the dimensions shown in Fig. (15) and Fig. (16) above. The results of this process are shown in the following figures:

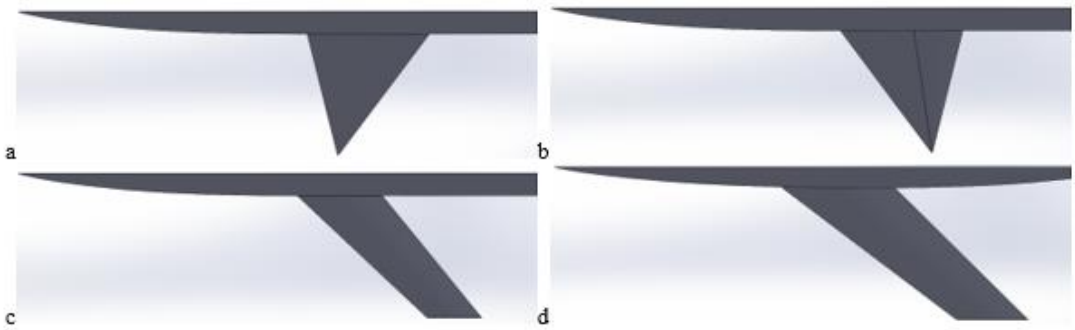

Figure 17. SolidWorks Base Body Geometries

In Fig. (18) are the comparable bodies of revolution designed using the Transonic Area Rule. Each of these bodies has an equivalent cross-sectional area development to their original wing-body combinations. For example, in the unswept and delta wing cases, the peak cross-sectional area points in the comparable bodies can be seen to coincide close to the location of the tip of the wing longitudinally. However, it should be noted that the location of maximum thickness on the wings will alter this location as greater thickness adds greater cross-sectional area.

Figure 18. SolidWorks Comparable Bodies of Revolution

Similarly, in Fig. (19) below, there are the indented bodies. As explained in Chapter 2 of this report, the indentation of the body is simply the opposite process of the

comparable bodies above. Rather than adding the cross-sectional area of the wings to the bodies, it is instead subtracted from the body. Thus, the bodies in Fig. (18) have the same cross-sectional area development as the respective bodies in Fig. (19).

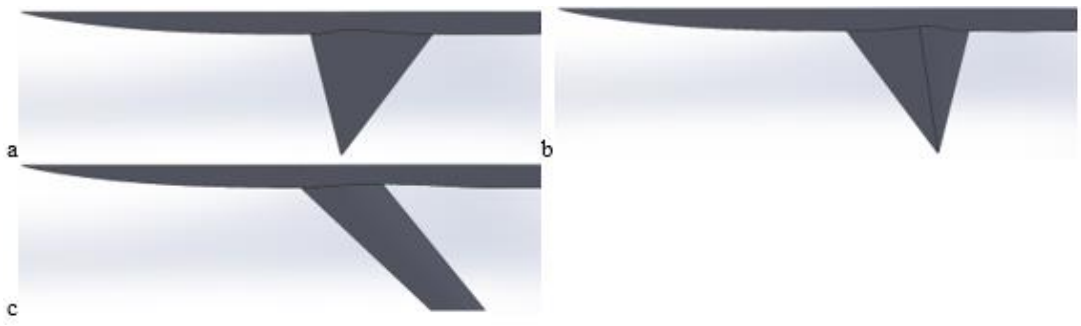

Figure 19. SolidWorks Indented Bodies

c. Pointwise Surface & Volume Meshes

Once the 3-D models were created, they could be transferred into a software called Pointwise which is used to create volume meshes. These volume meshes are then used in CFD codes to produce solutions based on the desired variables. The general process begins with creating a surface mesh on the body as is shown below. In Pointwise, a delta s value is chosen to create the surface mesh. This value refers to the average grid point spacing on selected connectors (shown as the blue lines outlining the model). The delta s value used for every model's body is 0.0025-m, which equates to approximately 0.01-in. The wings, however, use a value of 0.0015-m (~0.06-in) due to the complexity of the flow on this portion in comparison. Given the length of the cylindrical body, this equates to approximately 4,300 points along a connector of the body. Given that the curved body is shorter, this equates to approximately 3,260 points

along the body length. The unswept and delta wings then end up with approximately 30,000 points total over their whole surface. The swept wing has approximately 35,000 points total over its whole surface.

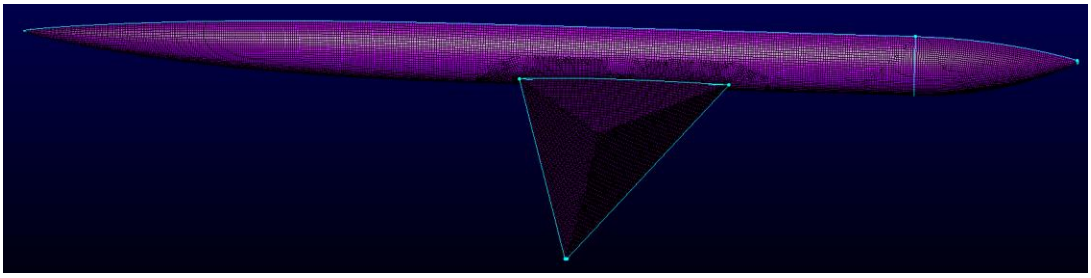

Figure 20. Example Unswept Wing, Cylindrical Body Surface Mesh

A point to note is that there is a boat-tail added to the back of the geometry as seen in Fig. (20). This feature was added to all models to improve code convergence when fed to the SU2 solver, which will be discussed in further detail in the next section. Continuing the meshing process, however, a volume grid could then be created stemming off the surface mesh. After properly initializing this grid, a mesh like the one shown in Fig. (21) is created. The total points in each of these volume grids is shown in Table 5 in Chapter 7 of this report. Each of the volume grids created is hybrid in terms of the types of elements used (i.e. tetrahedrals, pyramids, etc.) and can be seen in Fig. (21). Along with this, the far-field was extended out in every direction approximately 35 body lengths (~35m).

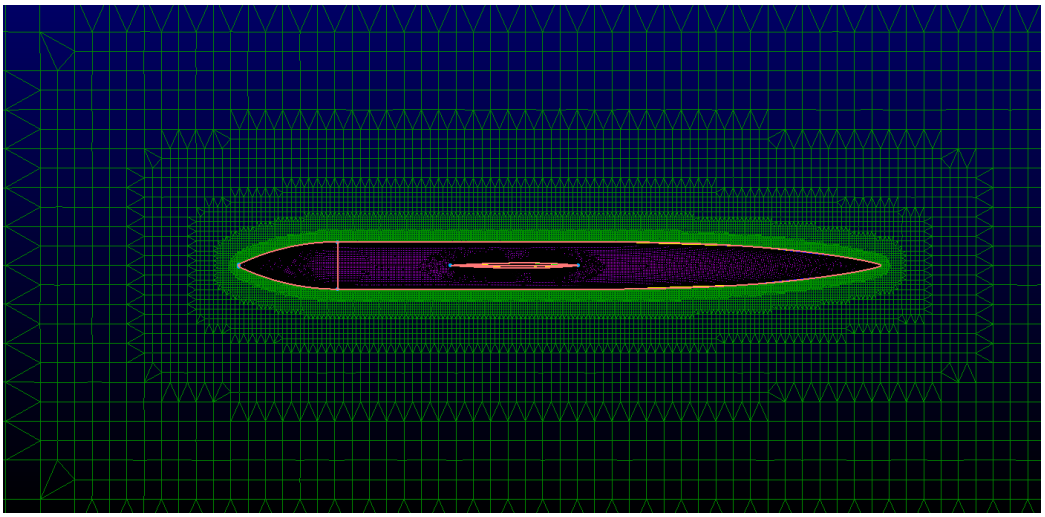

Figure 21. Symmetry Wall View of Volume Mesh

Once all these steps are completed, the boundary conditions could be set for recognition in SU2. The boat-tail added to the back of the geometry is referred to as "sting," the fuselage and wing as "body," the symmetry wall as "symm," and the far-field as "farfield." The mesh file is the converted to an SU2 file type to be run through the solver.

d. SU2 CFD Code

SU2 (v7.1.1 "Blackbird") is an open-source CFD code chosen to use for analysis of these geometries. Given the number of geometries, desired Mach number runs, and the computational intensity of these solutions, an inviscid "Euler" solution was used. This means that the surfaces defined as Euler boundaries in the SU2 input file have a slip condition (i.e. no skin friction is included in these solutions). The reduction in computation time, however, is mainly attributed to dropping all viscous terms anywhere else in the flow that would have had to be calculated otherwise. This shouldn't be an

issue for comparison purposes as Whitcomb normalized his drag rise results by subtracting the drag coefficient measurements at a Mach of approximately 0.85 from the other solutions. According to Whitcomb "this subtraction nearly eliminated the effects of differences in the skin friction of the comparable configurations on the comparisons of the drag characteristics for these configurations[16]." It will be noted later, however, that the results presented in this report are normalized to a lower Mach number of 0.5.

Returning to explanation of the boat-tail at the end of the geometries, it should have no impact on the drag measurements as it is excluded from evaluation of coefficients. Whitcomb also does something like this by correcting the data to "a condition at which the base pressure is equal to the stream static pressure[16]." Given that SU2 obtains its drag coefficient by integrating the pressures projected onto the surface of the geometry, the effect should be the same.

Finally, once the Euler boundaries (body and sting), far field (farfield), and symmetry wall (symm) are defined, the free-stream Mach number can be input. As the solution is computed, a history file is updated with the progressing drag coefficient and rms values. For convergence, the column on the far left (rms[Rho]) in Fig. (22) below must reach a value of -11. Convergence generally isn't an issue between columns as they generally follow the same trend. The exceptions to this are typically the RhoW and RhoE terms. For context, "Rho" refers to density, the "U, V, and W" terms refer to velocity components and the "E" terms refers to energy. To demonstrate this convergence, Fig. (23) and Fig. (24) below show the rms values, and lift and drag coefficient values versus iteration number, respectively. The lift values should be expected to remain around zero

given that the geometries are at zero-lift angle of attack (zero degrees given symmetry of upper and lower surfaces for all cases).

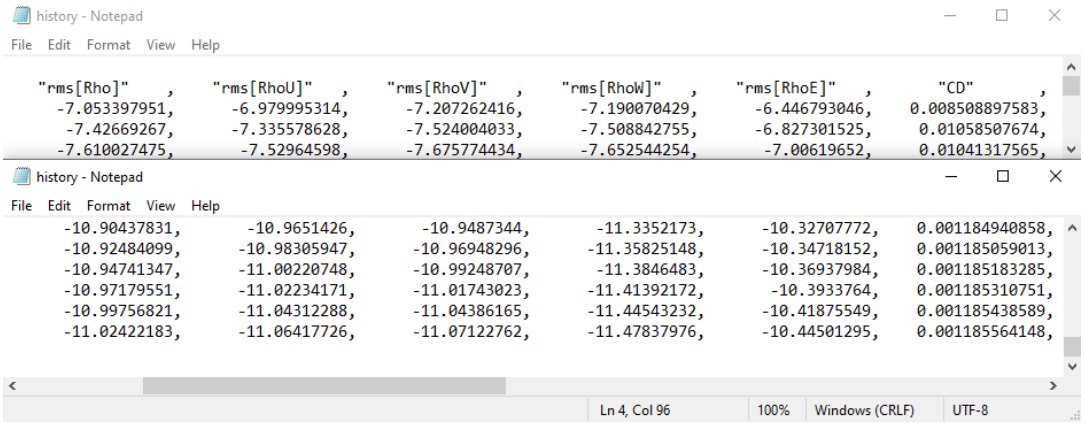

Figure 22. Convergence History of Unswept Wing, Cylindrical Body at M=0.88.

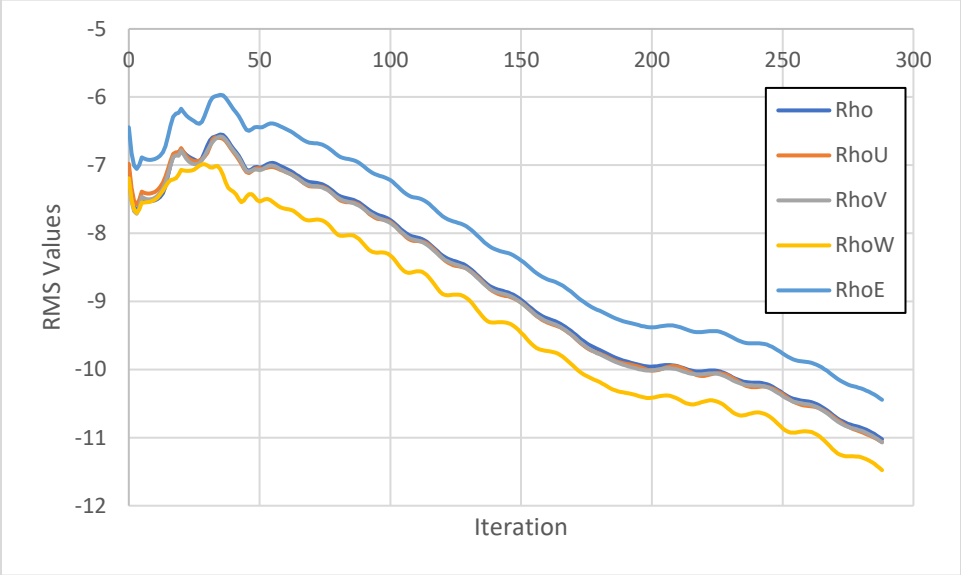

Figure 23. RMS Values vs. Iteration Number

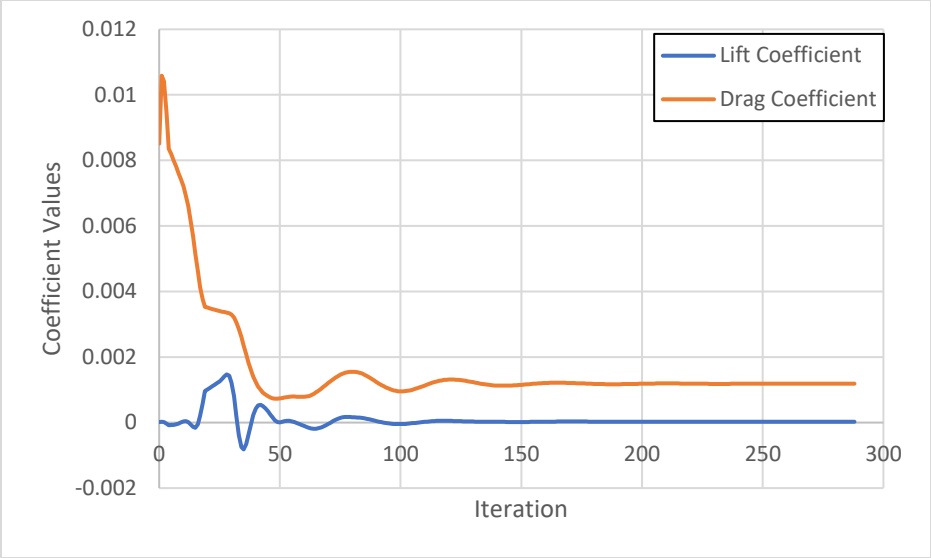

Figure 24. Lift and Drag Coefficients vs. Iteration Number

All solutions are made sure to converge before being included in any data within this report. Once the solutions are completed, the calculated data from SU2 is transferred to TecPlot output files for the surface flow and 3-D volume flow solutions. Each run of SU2 to output these files is for a geometry at a single Mach number. Thus, for 11 geometries and 8 Mach numbers each, this code had to be run 88 times.

e. TecPlot CFD Solution Modeling

TecPlot is a simple CFD solution visualizer that is used to present the flow characteristics modeled by the SU2 solutions discussed above. This includes some planform views of the models with either pressure coefficient or Mach number data shown on the surface of the bodies or 3-D flow solutions showing shock waves coming off the body. It should be noted that the flow and surface solutions will be in reversed directions, so it is important to pay attention to the coordinate system that will be

included in all these solution images. In these solutions, there will be some data probing for pressure coefficients at Mach numbers at locations determined to be shocks.

The determination of shocks in this thesis are subjective as they are determined by locations where the local flow goes from supersonic to subsonic over a distance where the probes are close together and the measured variables change drastically. An example of what is determined to be a shock is shown in Fig. (25) and Table 1 below. The probes here go from top to bottom in ascending order (i.e. probe 1 is closer to the root of the wing and probe 3 is near the wing-tip). In these solutions the flow is moving along the positive x-axis. Thus, the “a” probes are the upstream points and the “b” probes are downstream (after the shock). It should also be mentioned here that the black band regions will always show layers of Mach numbers between 0.9875 and 1. This is to keep consistency of determining shocks between solutions and gives a clear enough threshold to define a shock. In the example case below, it has been determined that probes 1 and 3 are located at shocks whereas probe 2 is not. In Fig. (25) it can be seen that the probes in 1 and 3 are kept quite close together before and after the black band, whereas the probes at 2 are separated a considerable distance. Then, in Table 1, it can be seen that even at the short distances at locations 1 and 3, they are still jumping from supersonic to subsonic a considerable amount (as demonstrated by the Mach number data). Location 2, however, has a short, smooth jump between supersonic to subsonic over a much greater distance. This becomes the basis of defining shocks in these solutions.

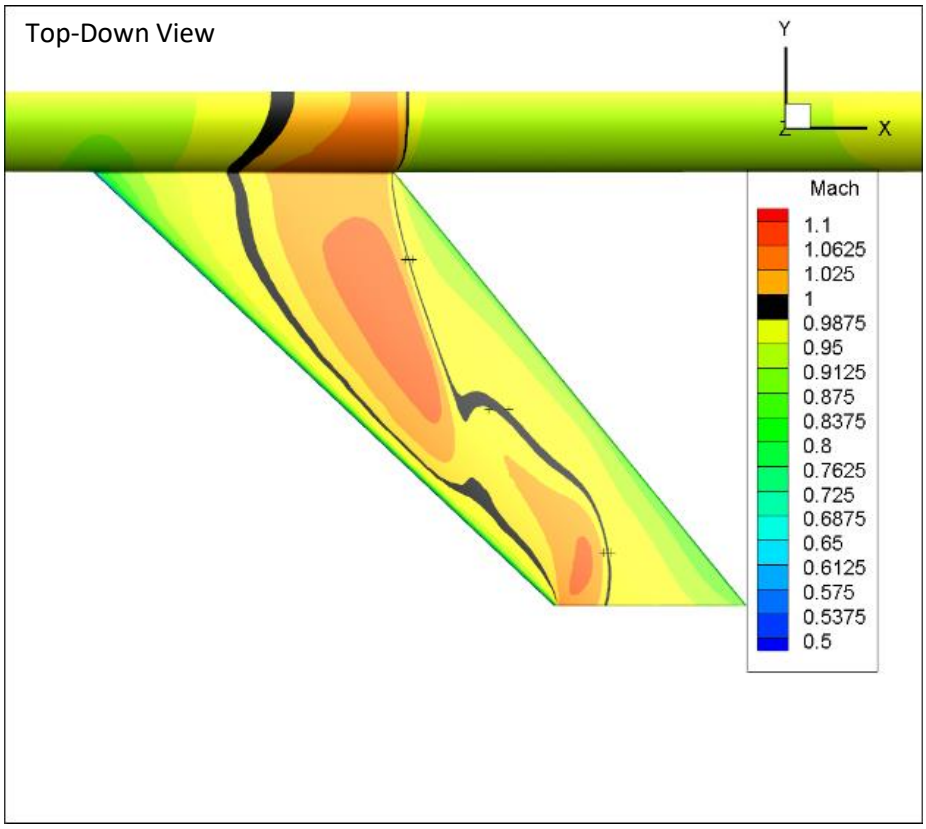

Figure 25. Swept Wing Cylindrical Body at M=0.95.

Table 1. Non-Shock & Shock Example Data Probes

Probes (Wing)	***CP***	**Mach**	**Shock/Non-Shock**
1a	-0.176	1.014	Shock
1b	-0.096	0.964	
2a	-0.157	1.002	Non-Shock
2b	-0.127	0.984	
3a	-0.181	1.014	Shock
3b	-0.116	0.975	

Finally, as shock patterns become more complex, keeping track of data probe locations also gets complicated, so a general template is defined for the order and location of probes. In Fig. (26) below, the general order is demonstrated. As discussed in the shock determination, regions of very thing black band regions will generally be determined to be a shock, but they will be differentiated by whether they are on the fuselage or the wing. Thus, probe locations 1 and 6 in Fig. (26) are body shocks, whereas all other probes refer to wing shocks. The other level of separation is then if these regions are connected along the same thin black band. Thus, probe locations 2 and 3 refer to the same shock, whereas probe locations 4 and 5 refer to a difference shock. Probe locations 1 and 2 would refer to the same shock if not differentiated by body vs wing. Then, the order of probing goes from left to right in all cases (even in flow solutions where the coordinate system is reversed). If the shock is vertical along a surface (i.e. no left-right separation), then the priority is from top to bottom. This is presented in Fig. (26) in ascending order from 1 to 6. These formats are then the general way that these solutions will be presented throughout the report.

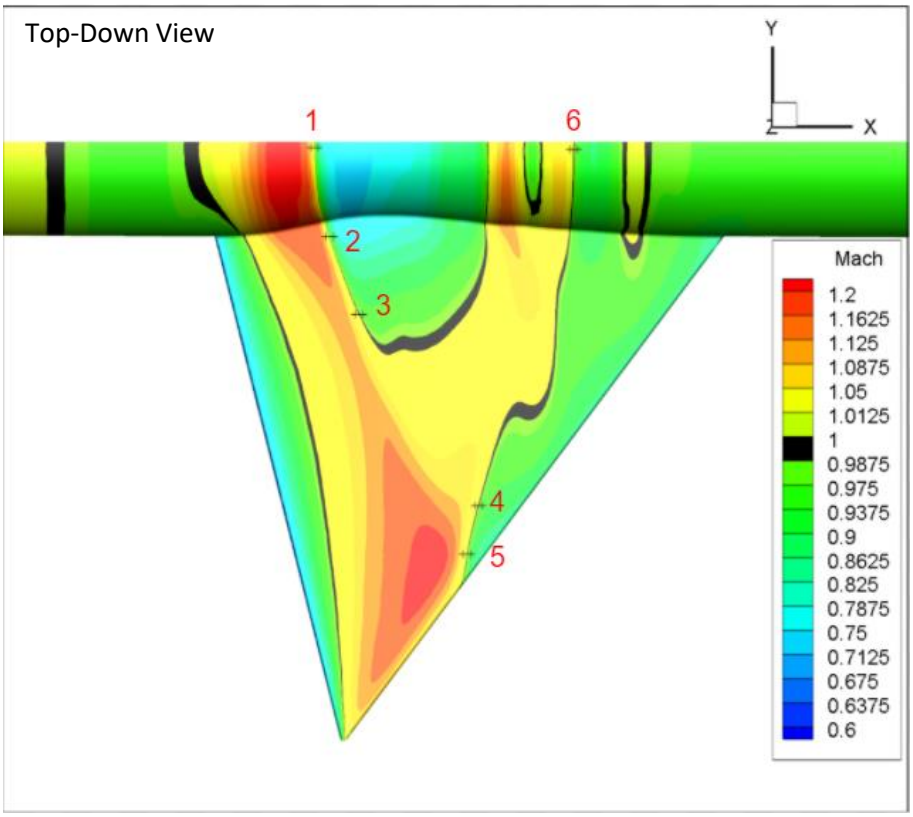

Figure 26. Example of Probe Placement

CHAPTER 4

COMMON WAVE DRAG ESTIMATION METHODS

Though CFD analysis is a relatively new tool growing in popularity, it is time consuming in its development process (as was demonstrated in the previous chapter) and is generally computationally intensive. It is for these reasons that there are still other wave drag estimation methods in use that require far less information to provide a relatively accurate approximation of the wave drag produced by a geometry. Thus, it becomes dependent on the steps of the design process one is in. The simpler wave drag estimation methods allow for a quick test of multiple geometries while CFD analysis allows for a more in depth look into the flow conditions of a chosen geometry.

Brenda Kulfan[9] discusses some of the differences between these two types of methods of drag approximation. A list of these differences is shown in Fig. (27) where Planar Linear Theory Analyses refer to analyses performed using methods derived from linear potential flow theory with planar boundary conditions. According to Kulfan[9], these planar linear theory analyses tend to underestimate compression pressures and overestimate expansion pressures, but they tend to be insignificant for drag measurements. Another behavior is that the disturbances modeled by linear theory propagate along freestream Mach lines which may cause issue in accurately prediction the development of shocks. Regarding the point on interference between lift and volume, Kulfan states that “these differences typically are not significant effects for long slender, thin configurations at low lift coefficients[9].” The last point is very important to take into consideration as viscous effects can cause major differences from realistic flows.

Methods developed using linear potential flow theory will neglect viscous interaction effects and thus the contribution of viscous effects to lift and drag values.

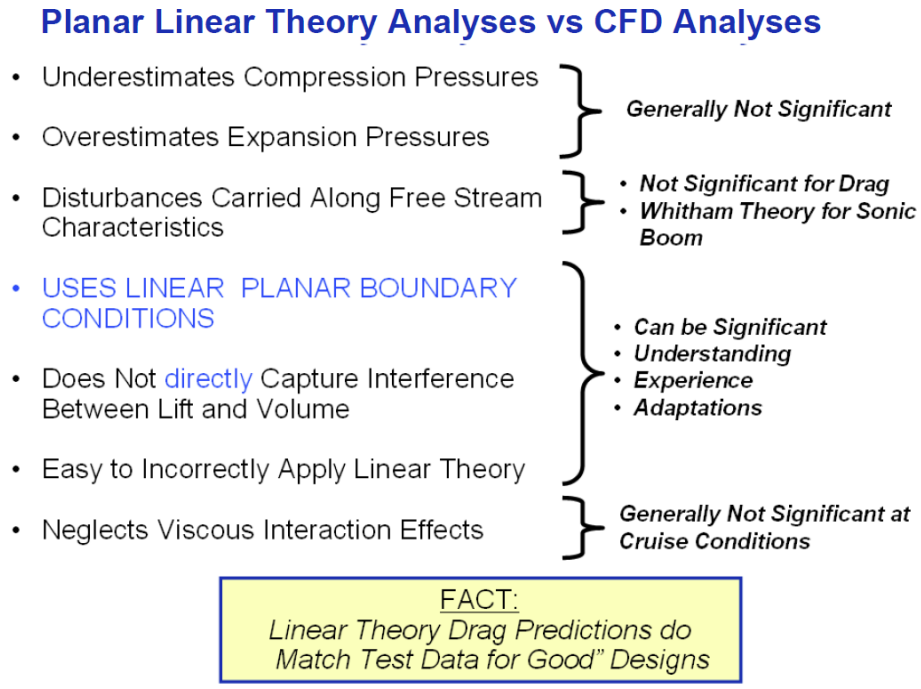

Figure 27. Planar Linear Theory Analyses vs CFD Analyses[9]

Another advantage to using these linear theory analyses is that total drag approximations can be broken into several different sources of drag through drag decomposition. Many of these methods function by approximating each component of drag through different applications of many of the same theories and then essentially combing the contributions into a single drag value. Thus, each component has its own separate development and can be singled out to observe values of particular interest.

With this in mind, two very common wave drag estimation methods were used to approximate the wave drag produced by Whitcomb's geometries in an attempt to match

the data provided in his report. Thus, in this work there are then three sources of approximation to allow for more in-depth comparison of results and further validation of accuracy if there is consistency.

a. EDET

EDET stands for "Empirical Drag Estimation Technique" and functions exactly as its name states. This code was designed to "use information already known about existing aircraft to predict the characteristics of future designs[4]." The general idea was not necessarily to completely accurately predict the total drag experienced by a geometry, but to instead provide a fairly accurate approximation early in the design process to guide decision making. This code provides drag coefficient approximations for many types of drag sources, including skin friction drag. However, given the Euler solution used for the CFD results (i.e. inviscid), the only term used from EDET results is the wave drag. According to the report by Feagin & Morrison, the wave drag is separated into drag due to volume (zero-lift drag) and drag due to lift. In Whitcomb's report, he is testing symmetrical wing sections with the models being at zero angle-of-attack, and thus at zero-lift. Thus, the only term of concern from EDET's wave drag is the zero-lift wave drag. This portion is itself split into components being the contribution from the fuselage, wing, and a wing-body interference effect[4]. Thus, there is only focus on the zero-lift wave drag term that could be found in the EDET table of values for the conditions of interest.

To determine the estimated value of zero-lift wave drag, one must first calculate the contribution from the fuselage. To do this the trends of Fig. (29) and Fig. (30) below

are used. It should be noted that these trends were extended as in Table 2 below to account for the values needed for Whitcomb's geometries. However, to determine the correct trends to be following, one must calculate the fuselage length to diameter ratio, body closure ratio (the base area of the fuselage), the reference area (typically wing area), and the maximum effective body cross-sectional area (referred to as Sπ). An example of the area values determined is shown in Fig. (28) below. Thus, the correlation of input geometry to the empirical data used in EDET is based on the "equivalent fineness ratio" of said geometry and is used to estimate the value of CD_{π}.

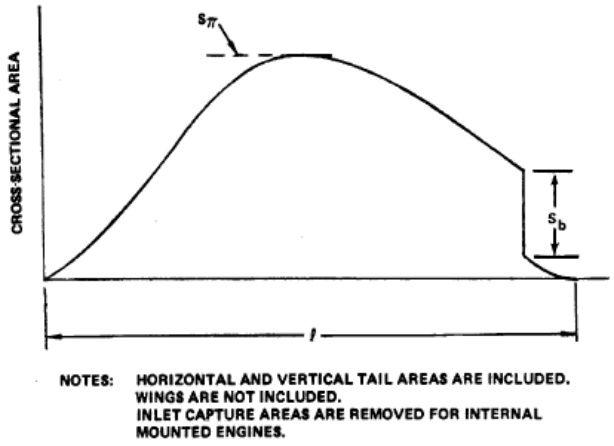

Figure 28. Cross-Sectional Area vs. Length of Geometry[4]

OF POOR QUALITY

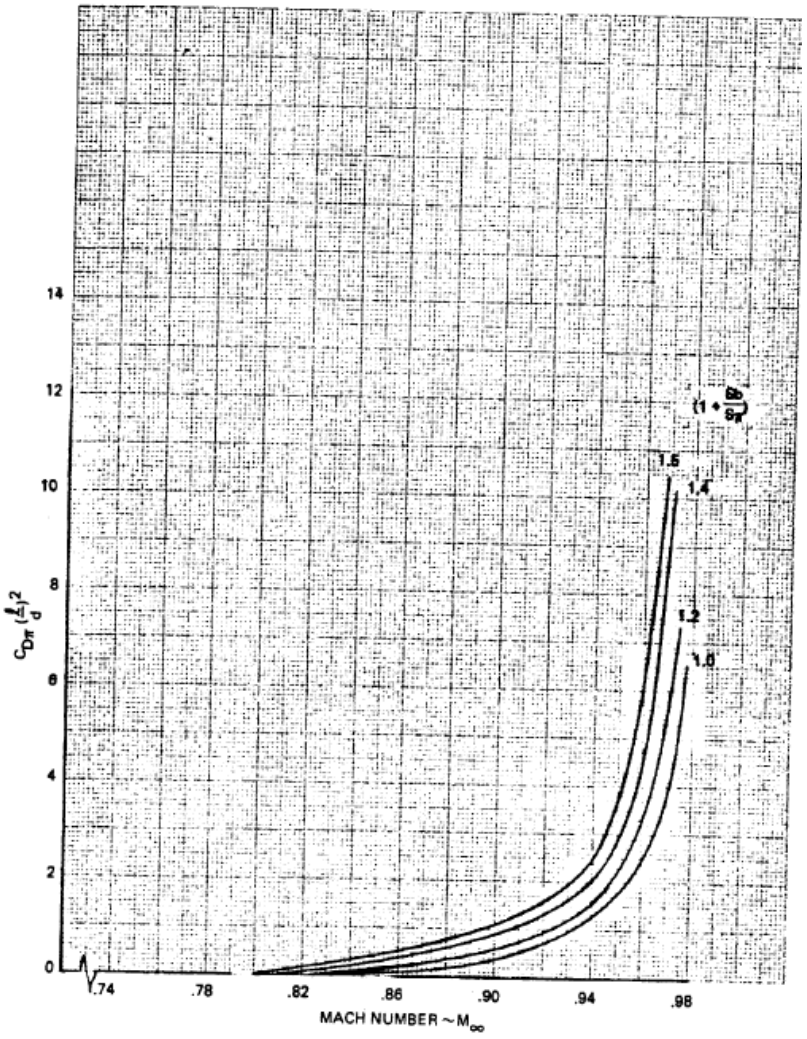

Figure 13. - Subsonic fuselage compressibility drag.

Figure 29. Subsonic Fuselage Compressibility Drag[4]

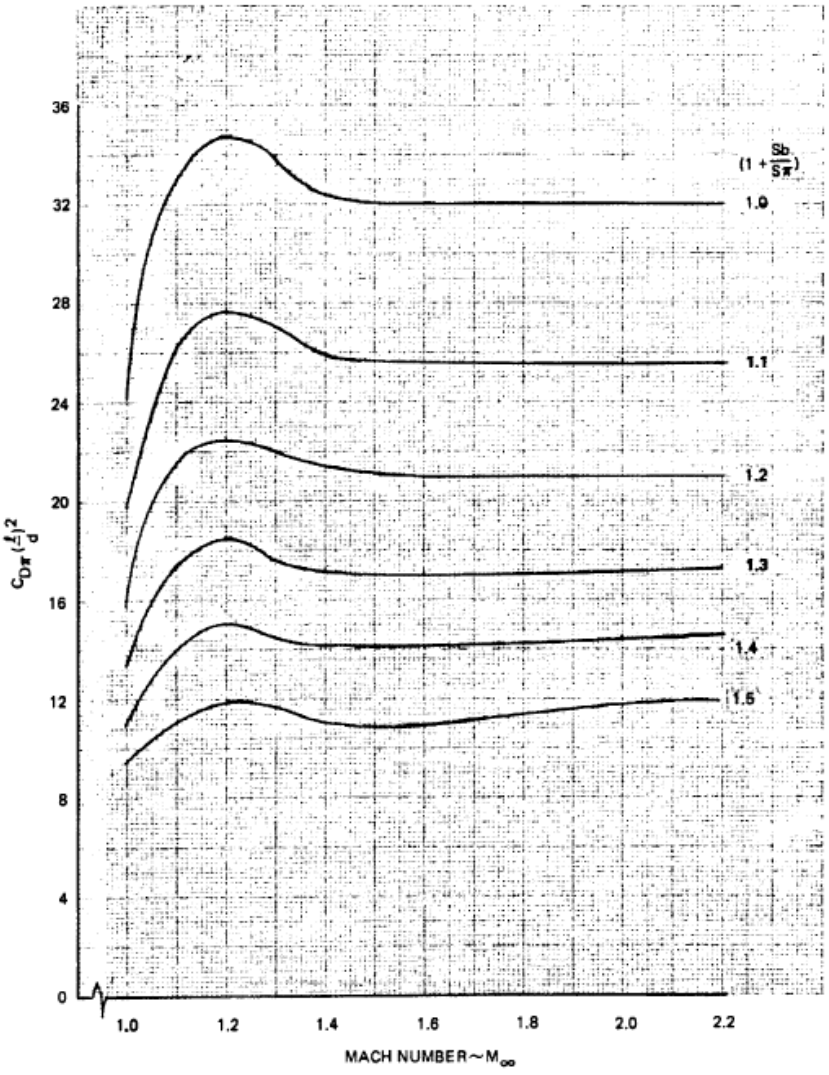

Figure 14. - Supersonic fuselage compressibility drag.

Figure 30. Supersonic Fuselage Compressibility Drag[4]

Table 2. Extended EDET Table

EDET WAVE DRAG TABLES

C BODY COMPRESSIBILITY DRAG TABLES
C MACH NUMBER ON THE VERTICAL..BASE AREA FUNCTION ON THE HORIZONTAL
C
C

1 + Sb/Spi	1	1.1	1.2	1.3	1.4	1.5	1.75	2
MACH= .200	0	0	0	0	0	0	0	0
MACH= .500	0	0	0	0	0	0	0	0
MACH= .700	0	0	0	0	0	0	0	0
MACH= .780	0	0	0	0	0	0	0.4	0.8
MACH = .820	0	0	0	0.1	0.32	0.64	1.04	1.44
MACH = .840	0	0	0.01	0.24	0.58	1.04	1.44	1.84
MACH = .860	0	0	0.11	0.41	0.86	1.47	1.87	2.27
MACH = .880	0.03	0.06	0.26	0.64	1.21	1.95	2.35	2.75
MACH = .900	0.16	0.21	0.47	0.93	1.6	2.48	2.88	3.28
MACH = .910	0.29	0.35	0.63	1.13	1.85	2.79	3.19	3.59
MACH = .920	0.46	0.53	0.82	1.35	2.11	3.11	3.51	3.91
MACH = .930	0.66	0.76	1.09	1.67	2.48	3.52	3.92	4.32
MACH = .940	0.97	1.11	1.48	2.09	2.95	4.04	4.44	4.84
MACH = .950	1.38	1.67	2.18	2.89	3.81	4.94	5.34	5.74
MACH = .960	1.94	2.65	3.47	4.41	5.47	6.64	7.04	7.44
MACH = .965	2.38	3.51	4.66	5.82	7	8.19	8.59	8.99
MACH = .970	3.15	4.96	6.62	8.11	9.45	10.64	11.04	11.44
MACH = 1.00	24.5	20	16.21	14.87	12.88	10.87	10.58	9.52
MACH = 1.05	30.68	23.73	19.65	17.22	14.02	11.06	10.06	8.56
MACH = 1.10	32.98	26.32	21.19	18.38	14.42	11.36	9.36	7.36
MACH = 1.15	34.28	27.41	22.01	19.17	14.84	11.87	9.87	7.5

RECALL THE EDET FORMULA

Sref	1	ft^2
Spi	0.077	ft^2
FINENESS RATIO (L/D)	11.47	
1 + SB/SPI	2	

MACH	Cdpi(L/D)^2	Cdpi	CDc
0.2	0	0	0
0.5	0	0	0
0.7	0	0	0
0.78	0.8	0.006081	0.000468
0.82	1.44	0.010946	0.000843
0.84	1.84	0.013986	0.001077
0.86	2.27	0.017254	0.001329
0.88	2.75	0.020903	0.00161
0.9	3.28	0.024931	0.00192
0.91	3.59	0.027288	0.002101
0.92	3.91	0.02972	0.002288
0.93	4.32	0.032837	0.002528
0.94	4.84	0.036789	0.002833
0.95	5.74	0.04363	0.00336
0.96	7.44	0.056552	0.004354
0.965	8.99	0.068333	0.005262
0.97	11.44	0.086956	0.006696
1	9.52	0.072362	0.005572
1.05	8.56	0.065065	0.00501
1.1	7.36	0.055944	0.004308
1.15	7.5	0.057008	0.00439

Finally, to determine the value of the fuselage contribution zero-lift drag due to slender body compressibility effects, the following equation is used:

$$CD_C = CD_\pi * \frac{S_{ref}}{S_\pi} \tag{3}$$

To determine the zero-lift wave drag from EDET for the Whitcomb geometries, the following values in Table 3 must then be used with Eq. (3) and Table 2 above.

Table 3. Necessary Fuselage Values for Use in EDET Corrections

CONFIG	**Sref (ft^2)**	**Sπ (ft^2)**	**(L/D)**	**1+Sb/Sπ**
All Cylindrical Body Cases	1	0.077	11.47	2

The next step of the process is then to apply the wing wave-drag contribution correction. This starts with a variable referred to as M_{DES} which is an empirical function of leading-edge sweep, camber, and aspect ratio of a wing. It is determined by finding the 2-D drag divergence Mach number (found using Fig. (32)) correlated with the geometry's design lift coefficient (determined using the curves in Fig. (31) below) and corrected to be 3-D by including corrections for the sweep and aspect ratio effects. Then, for an uncambered wing, the wave drag increment for the wing can be calculated using Eq. (4) below.

$$\Delta CD_{Cwing} = K2 * \left(\frac{t}{c}\right)^{\frac{5}{3}} \tag{4}$$

Thus, the wing wave drag contribution depends on the thickness ratio of the wing and this K2 value. As is shown in Fig. (33) below, K2 is related to the wing thickness as well along with the difference between the analysis Mach number and the design Mach number. Once the K2 value has been taken from that table, then it can be used in Eq. (4) to determine the wing's contribution. The values used for the wing wave drag contribution for Whitcomb's geometries are as shown in Fig. (34) below. Once both contributions are calculated, they can simply be summed to get the total approximated zero-lift wave drag for the geometry.

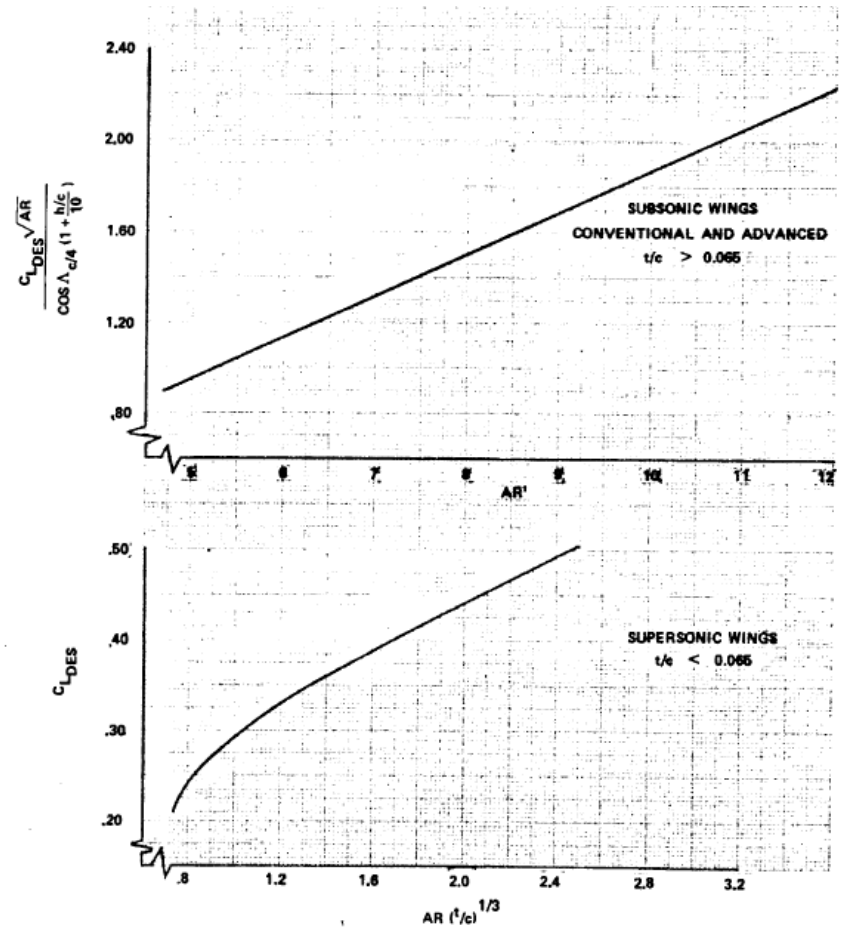

Figure 1. - Design lift coefficient.

Figure 31. Design Lift Coefficient Curves[4]

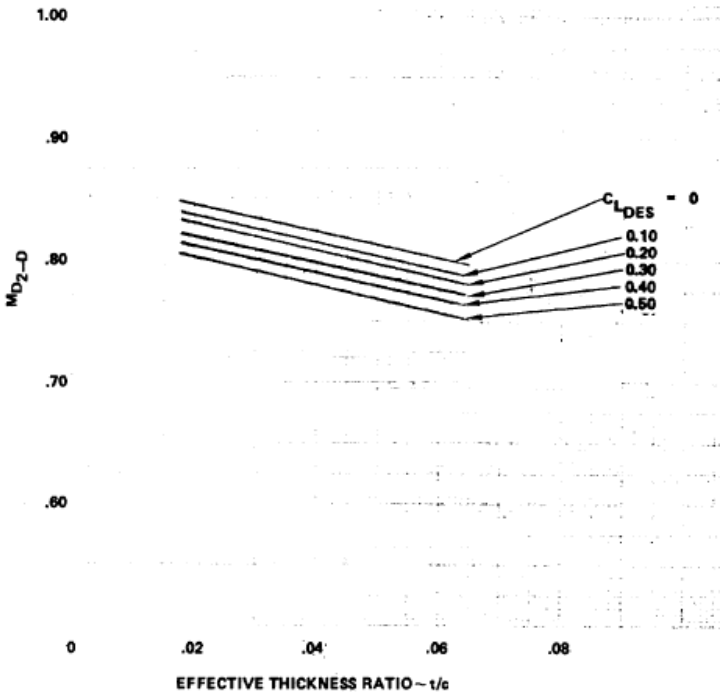

Figure 2. - Two-dimensional drag divergence Mach number, supersonic airfoil sections.

Figure 32. Two-Dimensional Drag Divergence Mach Number[4]

K2	Wing t/c						
	3.2%	4.2%	5.2%	6.4%	7.6%	10.3%	16.4%
-0.8	0.000	0.000	0.000	0.000	0.000	0.000	0.000
-0.2	0.060	0.040	0.020	0.020	0.010	0.008	0.002
-0.16	0.072	0.050	0.030	0.026	0.017	0.016	0.006
-0.12	0.100	0.060	0.040	0.038	0.025	0.024	0.012
DELTA -0.08	0.125	0.080	0.050	0.049	0.035	0.033	0.019
MACH -0.04	0.160	0.120	0.080	0.068	0.054	0.047	0.030
-0.02	0.200	0.160	0.120	0.110	0.070	0.059	0.039
(M-Mc 0	0.280	0.220	0.160	0.120	0.093	0.077	0.052
0.01	0.340	0.270	0.200	0.152	0.118	0.093	0.061
0.02	0.440	0.330	0.240	0.197	0.153	0.117	0.073
0.03	0.640	0.450	0.310	0.255	0.203	0.148	0.087
0.04	0.100	0.660	0.410	0.325	0.270	0.187	0.103
0.05	0.900	0.020	0.560	0.400	0.350	0.235	0.127

Figure 33. K2 Values Table[4,14]

Geometry	Sref	AR	SW25	t/c	SwetW	SwetB	Body(L/D)	1+Sbase/Spi	DesMach
DeltaWing Cylindrical Body,	1	4	25	4%	1.68	3.2	11.5	2	0.8843
SweptWing Cylindrical Body,	1	4	45	6%	1.68	3.2	11.5	2	0.9168
UnsweptWing Cylindrical Body.	1	4	0	4%	1.68	3.2	11.5	2	0.8543

Figure 34. Necessary Wing Values for Use in EDET Corrections

b. D2500

D2500, also known as the Harris Wave Drag Code, produces estimates of inviscid, supersonic pressure drag of shapes with fully attached flow. The whole basis of this code is making use of the Supersonic Area Rule (very similar to the Transonic Area Rule). The idea behind the Supersonic Area Rule is to take cutting planes parallel to each other through the configuration, all at the Mach angle for the freestream Mach number observed. The area distributions at each station from these cutting planes is then projected onto the plane normal to the freestream flow at their respective stations. The cross-sectional area development from combining the areas from the cutting planes is then made into the profile for equivalent bodies of revolution. However, the cutting planes can also be oriented at different angles as is shown by theta in Fig. (35) below. Several different angles for theta are then observed and equivalent bodies of revolution are created for each. Thus, for each Mach number observed, several different equivalent bodies are created corresponding to several values of theta. Then, "the wave drag of each equivalent body is determined by the von Kármán slender-body formula which gives the drag as a function of the free-stream conditions and the equivalent-body area distribution[6]." Finally, the results from the calculated wave drag values for each of the observed angles at a single Mach number is integrated to provide an average of these values. This is then the wave drag approximation by the Supersonic Area Rule[6,17].

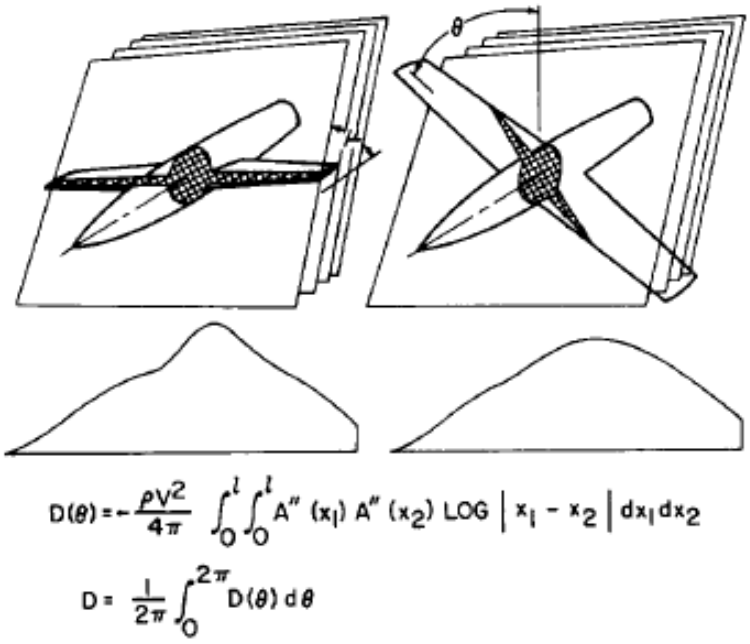

Figure 1.- Illustration of wave-drag computing procedure.

Figure 35. Wave-Drag Computing Procedure in Supersonic Area Rule[6]

However, it should be noted that the Supersonic Area Rule does not account for wave reflections due to interactions of flow between the fuselage and wing. Thus, more complicated geometries may prove to be more trouble for D2500, but it is not meant to be an exact method. Instead, the use of the Supersonic Area Rule is advised for early design processes to allow for quick trade studies before making permanent design choices. Thus, D2500 proves to be a quick, efficient method of making decisions early in the design process.

As might be expected, describing the geometry of a complex aircraft can be done many different ways, so the method D2500 uses has been documented extensively. The general idea is demonstrated in Fig. (36) below. Essentially, all components of the

aircraft are broken down into sections as shown in the mathematical model. The fuselage is described by the radii of equivalent circles at stations along the body, where the connection between stations (i.e. variation in radii) is assumed to be linear. The wings are then described by airfoil sections distributed along the span of the wing where the airfoil sections themselves are described by ordinate data. Once again, the connections between ordinate points are assumed to be linear. Horizontal and vertical tails to be included are described in a similar manner to the wings[6]. Given the simplicity of the Whitcomb geometries, no further complication is necessary.

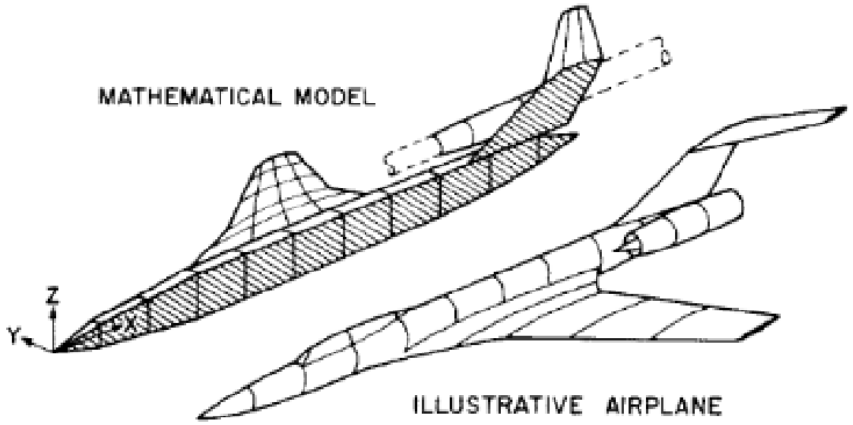

Figure 2.- Mathematical representation of illustrative airplane for machine-computing procedure.

Figure 36. D2500 Method of Mathematically Modeling an Illustrated Airplane[6]

The input file for the D2500 code requires the ordinates for the fuselage, the leading-edge location of the wing, wind chords, and wing airfoil sections. Thus, the input for D2500 fits the geometry of Whitcomb's models in a lot more detail than EDET and

functions by reducing the geometry to a comparable body of revolution. Once the program is given the necessary information in the input file like that shown in Fig. (37), it performs the process described by the Supersonic Area Rule above and yields an output file similar to that in Fig. (38) where the approximation of wave drag can be retrieved (the CDW terms).

```
*J0 J1 J2 J3 J4 J5 J6#AF#ORFUS#R1#F1#R2#F2#R3#F3#R4#F4POD#POFIN#FOCAN#CO
*2312312312312312312312312312312312312312312312312312312312312312123
  1 -1 -1  0  0  0 -1  2 10  1 12 15  0  0  0  0  0  0  0  0  0  0  0CONTROL
*234567
144.00                                                                 REFA
*2341234123412341234123412341234123412341234123412341234123412341234
  0.000 10.000 20.000 30.000 40.000 50.000 60.000 70.000 80.000100.000  XAF 1
*234567!234567!234567!234567!
 23.969 1.8779  0.00  10.118                                           WAFORG  1
 26.475 11.900  0.00  0.100                                           WAFORG  2
*234567!234567!234567!234567!234567!234567!234567!234567!234567!234567
 0.0000 0.8205 1.4398 1.8671 2.000  1.8968 1.7638 1.485  1.0475 0.0000  WAFORD  1-1
 0.0000 0.8205 1.4398 1.8671 2.000  1.8968 1.7638 1.485  1.0475 0.0000  WAFORD  2-1
*234567!234567!234567!234567!234567!234567!234567!234567!234567!234567
 0.00   1.125  2.250  4.50   9.00   11.25  13.50  15.75  20.25  22.50   XFUS 1-1
25.00   30.00  35.00  40.00  43.00                                      XFUS 1-2
*234567!234567!234567!234567!234567!234567!234567!234567!234567!234567
 0.00   0.3318 0.9229 2.4717 6.0786 7.6356 8.8985 9.8423 10.916 11.045  FUSARD 1-1
 11.045 11.045 11.045 11.045 11.045                                    FUSARD 1-2
*2341234123412341234123412341234123412341234123412341234123412341234
1.501200  60  16                  1                                   CASE 1
1.401200  60  16                  1                                   CASE 2
1.301200  60  16                  1                                   CASE 3
1.201200  60  16                  1                                   CASE 4
1.151150  60  16                  1                                   CASE 5
1.101100  60  16                  1                                   CASE 6
1.051050  60  16                  1                                   CASE 7
BOOM1000  60   1                  1                                   CASE 8
```

Figure 37. Unswept Wing, Cylindrical Body D2500 Input File

```
Entering OVL50 (ADIST)
Leaving OVL50 (ADIST)
Entering OVL60 (OUT)
Find max and min
Fill theta array from -90 to 90 deg          17  entries
Compute drag of entire aircraft
Volume of wing
Results
 MACH   =    1.150000
 CDW    =   1.0417249E-02
 D/Q    =    1.500084
 VOLUME =    17.74634
 * * * *
ICYC=  1
Leaving OVL60 (OUT)
End of this case.
Entering OVL50 (ADIST)
Leaving OVL50 (ADIST)
Entering OVL60 (OUT)
Find max and min
Fill theta array from -90 to 90 deg          17  entries
Compute drag of entire aircraft
Volume of wing
Results
 MACH   =    1.100000
 CDW    =   1.1995887E-02
 D/Q    =    1.727408
 VOLUME =    17.74634
 * * * *
ICYC=  1
```

Figure 38. Unswept Wing, Cylindrical Body Section of D2500 Output File

CHAPTER 5

WAVE DRAG RESULTS & COMPARISON

In this section there will be data presented on the normalized wave drag approximations produced by the SU2, EDET, and D2500 in comparison with the digitized results from Whitcomb's report. It should be noted that Whitcomb's results are normalized to the drag coefficient values produced at a freestream Mach number of 0.85, but the results in this report are normalized to those at a freestream Mach number of 0.5. This is done in an attempt to create a better comparison between the geometries observed because of their very different configurations. The idea behind this is that at a Mach number of 0.85, one may still expect compressibility effects to come into play (i.e. shocks and the like) here that may impact each of the geometries differently. At a Mach number of 0.5, flow can generally be treated as "incompressible" and thus establish a good point of comparison between each of the models. The drag coefficient and normalized drag coefficient data collected is included in Appendix B. The data taken from Whitcomb's report will also include error bars ranging +/- 0.0005 according to the report's claim of accuracy[16].

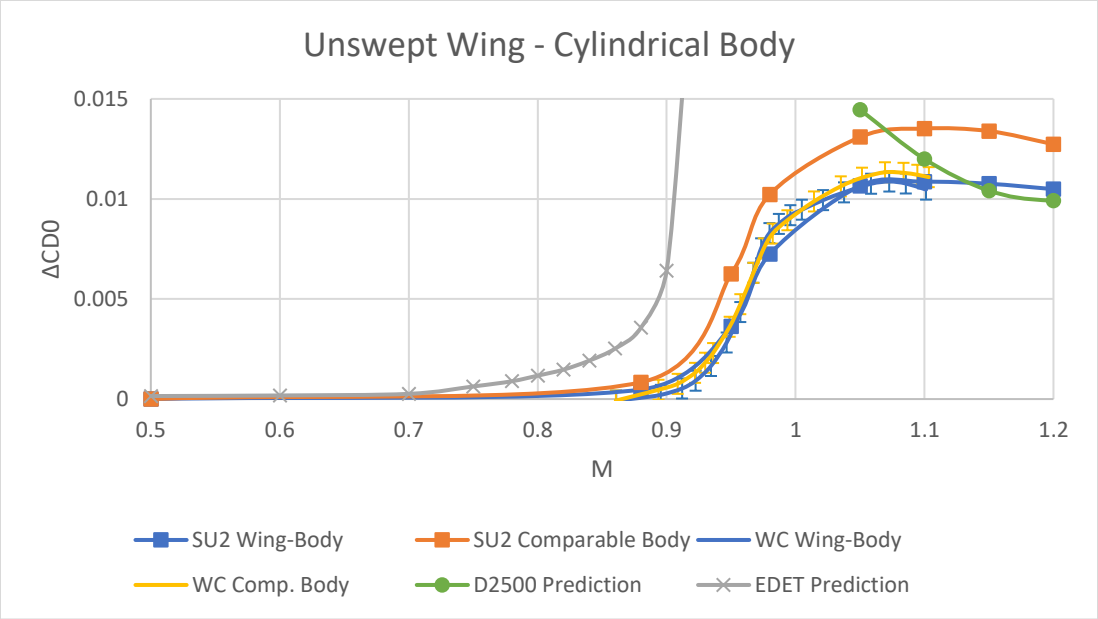

Figure 39. Unswept Wing Cylindrical Body Wave Drag Approximations

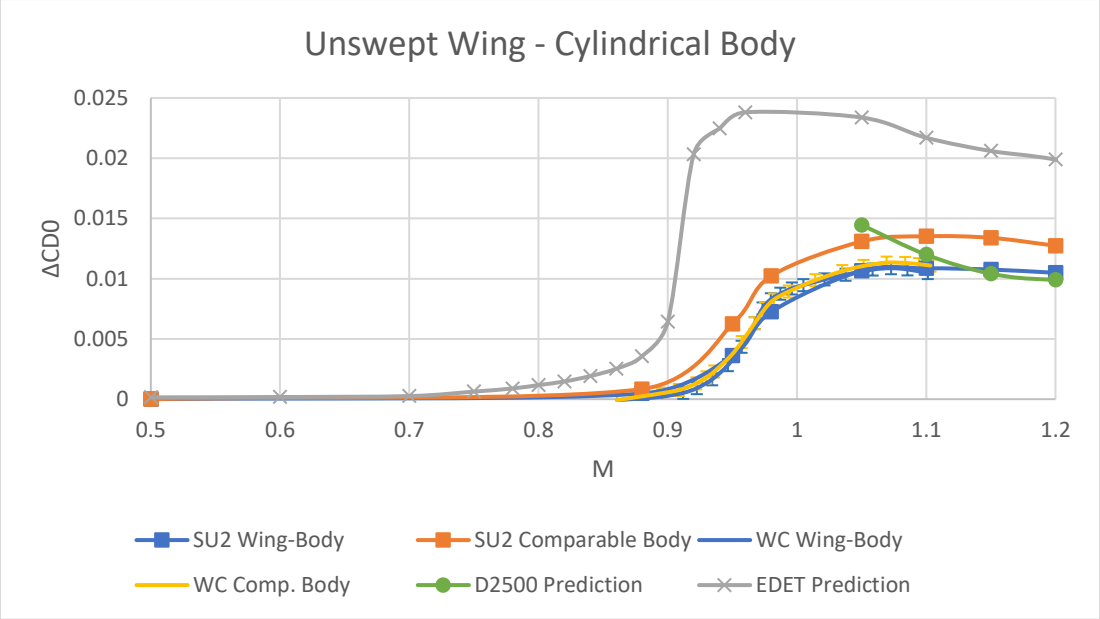

Figure 40. Full EDET Prediction for Unswept Wing Cylindrical Body

In the case of the unswept wing, cylindrical body geometry, Whitcomb's data shows that the base wing-body configuration has drag rise characteristics that nearly completely resemble that of the equivalent body of revolution, which fits the first claim of Whitcomb's Transonic Area Rule. The SU2 results, however, do not seem to fit the claim with the drag rise of the comparable body being greater than that of the base geometry. It should be noted, however that the SU2 wing-body solution appears to fit quite well with Whitcomb's wing-body measurements. Thus, SU2 appears to have done well at matching the wind tunnel data for the full configuration but does not agree with the comparable body configuration. The TecPlot visualizations of the flow may shed some light on this. As for the D2500 approximation, it seems to be pessimistic at the lower range of Mach numbers observed (M=1.05), but gradually aligns with the wing-body cases for both SU2 and Whitcomb's data (though the further trend of Whitcomb's data up to higher Mach numbers cannot be predicted). Finally, EDET appears to be greatly pessimistic at all Mach numbers observed for the drag rise of this geometry. There is no agreement whatsoever between this method and any others.

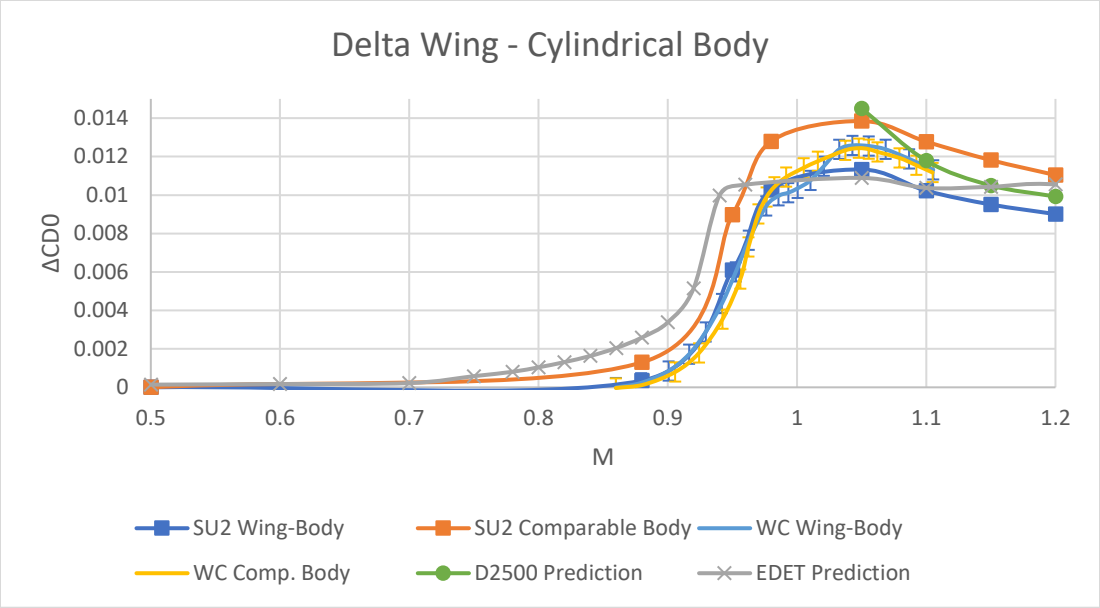

Figure 41. Delta Wing Cylindrical Body Wave Drag Approximations

In the case of the delta wing, cylindrical body geometry, Whitcomb's data again argues in favor of the first claim as both the wing-body and comparable body curves coincide for most of the Mach numbers observed. The only odd occurrence in this case is around a Mach number of 1 where the comparable body appears to yield greater values. In comparison to the SU2 data, the wing-body solution appears to agree quite well with the wind tunnel data up until a Mach number of approximately 1, after which the SU2 solution appears to underpredict. For the comparable body, however, the SU2 solution appears to predict higher values for all observed Mach numbers than the Whitcomb data or the SU2 wing-body solution. The D2500 prediction appears to start off higher than any other prediction until it gradually falls into place with the end of the Whitcomb data and fits in between the SU2 wing-body and comparable body cases. Finally, the EDET approximation seems to predict higher values up until a Mach number of approximately

0.95, where it is exceeded by the SU2 comparable body case. In a rather loose way, the EDET solution appears to agree with the SU2 wing-body case for a range of Mach numbers between 0.95 and 1.1.

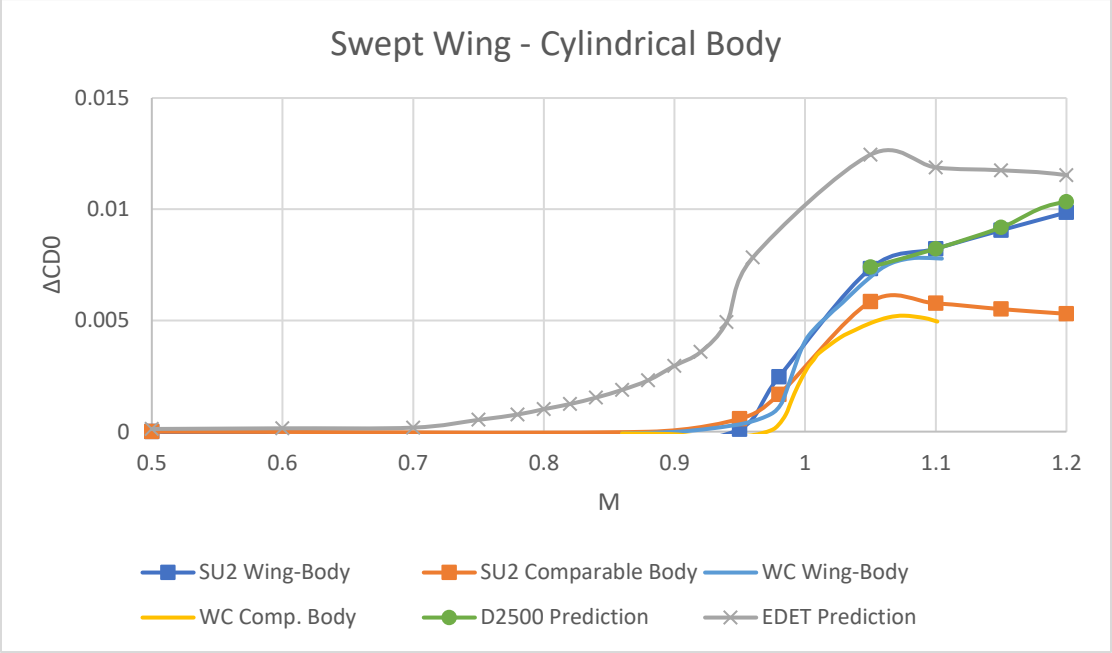

Figure 42. Swept Wing Cylindrical Body Wave Drag Approximations

The swept wing, cylindrical body geometry does not appear to argue the first claim like the unswept and delta cases did as even in Whitcomb's data, the wing-body and comparable body cases do not agree. Another interesting characteristic of this data is that the comparable body appears to produce lower values than that of the wing-body. This holds true for the SU2 cases as well, but the wing-body case appears to agree with Whitcomb's data more than the comparable body case. The SU2 comparable body produces greater values than that of Whitcomb's. The D2500 approximation in this case is interesting because it agrees almost perfectly with three of the values from the SU2

wing-body case and appears to approximate the Whitcomb data quite well at the end of it. Thus, the wing-body cases appear to agree quite well for the Whitcomb data, SU2 solution, and D2500 approximation. Finally, EDET, much like in the unswept case appears to predict much greater values than any other approximation used. There is once again no agreement between this method and any others.

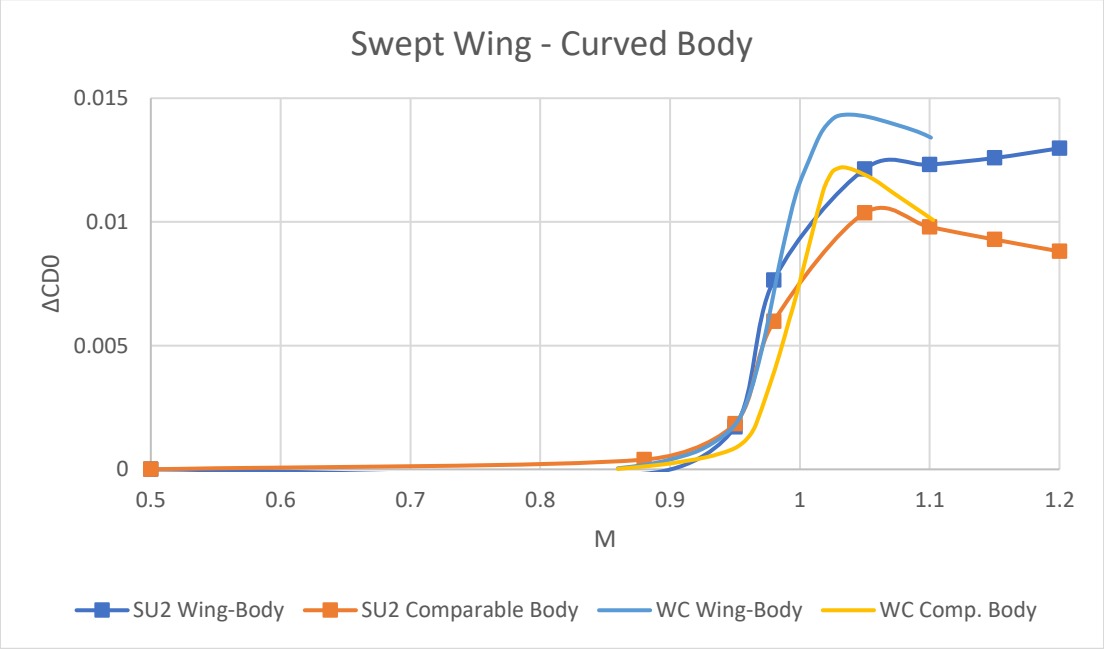

Figure 43. Swept Wing Curved Body Wave Drag Approximations

The final base geometry is that of the swept wing, curved body which, like the cylindrical body case, does not argue in favor of the first claim. Again, the comparable body of Whitcomb's data seems to produce values less than the wing-body. The only approximation method used for this geometry was SU2 and though they seem to agree that the comparable body produces less of a drag rise, the Whitcomb data and SU2 approximations do not appear to agree very well.

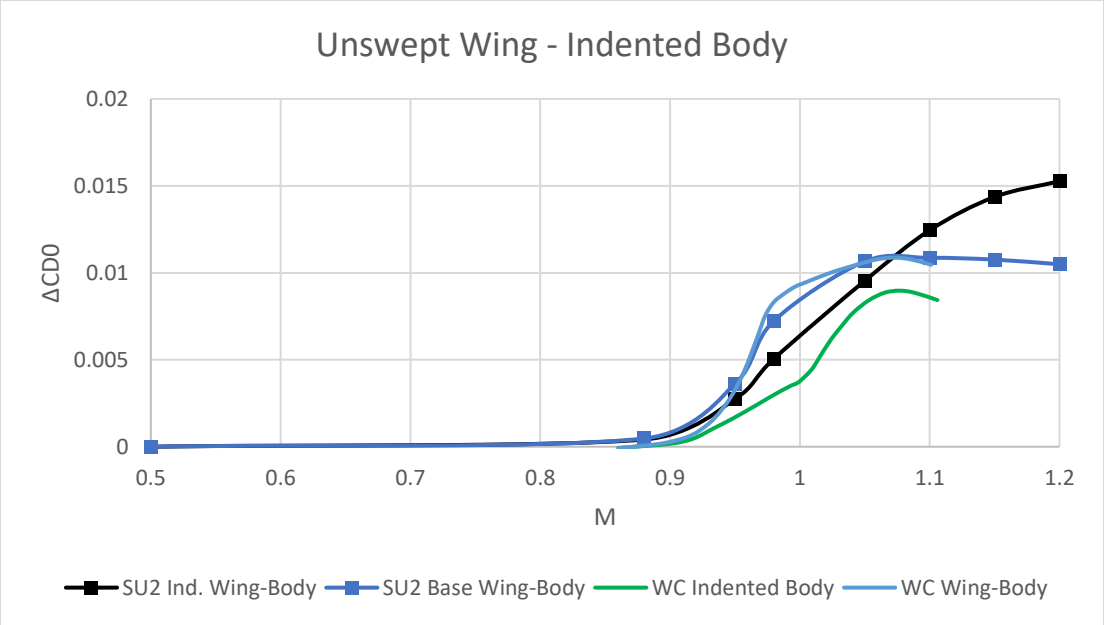

Figure 44. Unswept Wing Indented Body Wave Drag Approximations

In the second claim of the Transonic Area Rule, the indented body configuration should be expected to produce less of a transonic drag rise than the original wing-body configuration. However, as is seen in Fig. (16) for the unswept wing, this only appears to be true up to some Mach numbers. SU2 does indeed predict a lower transonic drag rise for the indented case up to a Mach number of approximately 1.05 and eventually exceeds the drag rise of the wing-body for greater Mach numbers. Along with this, the SU2 approximation appears to predict less of a reduction in the transonic drag rise than Whitcomb's data demonstrates.

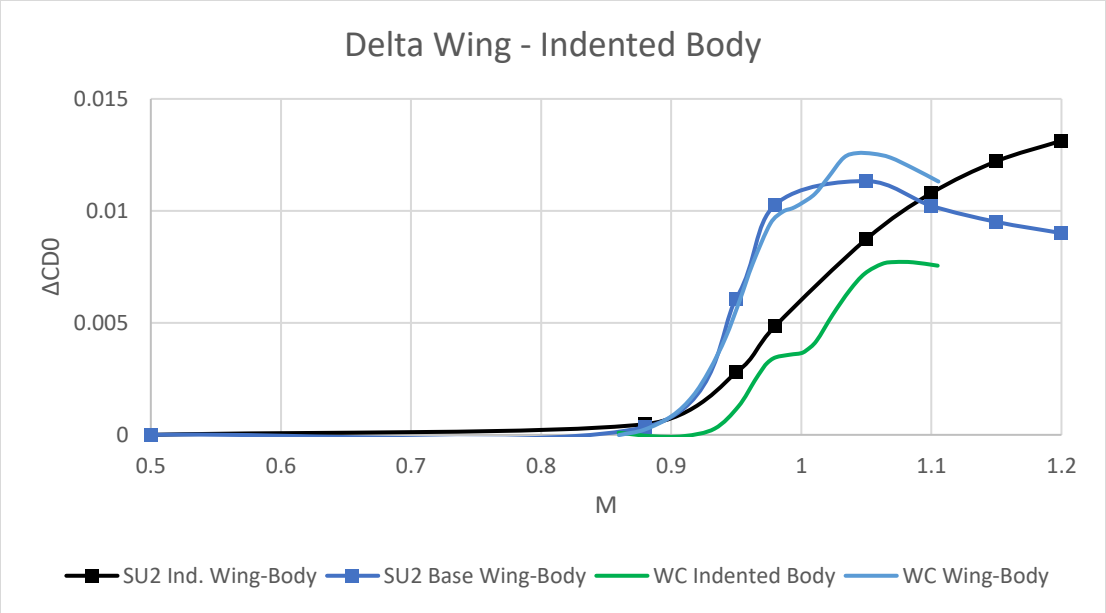

Figure 45. Delta Wing Indented Body Wave Drag Approximations

Similar to the unswept wing case, SU2 appears to predict a reduction in drag rise only up until certain Mach numbers, where again it exceeds the wing-body for Mach numbers higher than this. The SU2 prediction also seems to predict less reduction than Whitcomb's data demonstrates again. However, it does appear that the delta wing case does yield more of a reduction than the unswept case with a peak reduction of approximately 0.005 vs 0.002 both at a Mach number of 0.98.

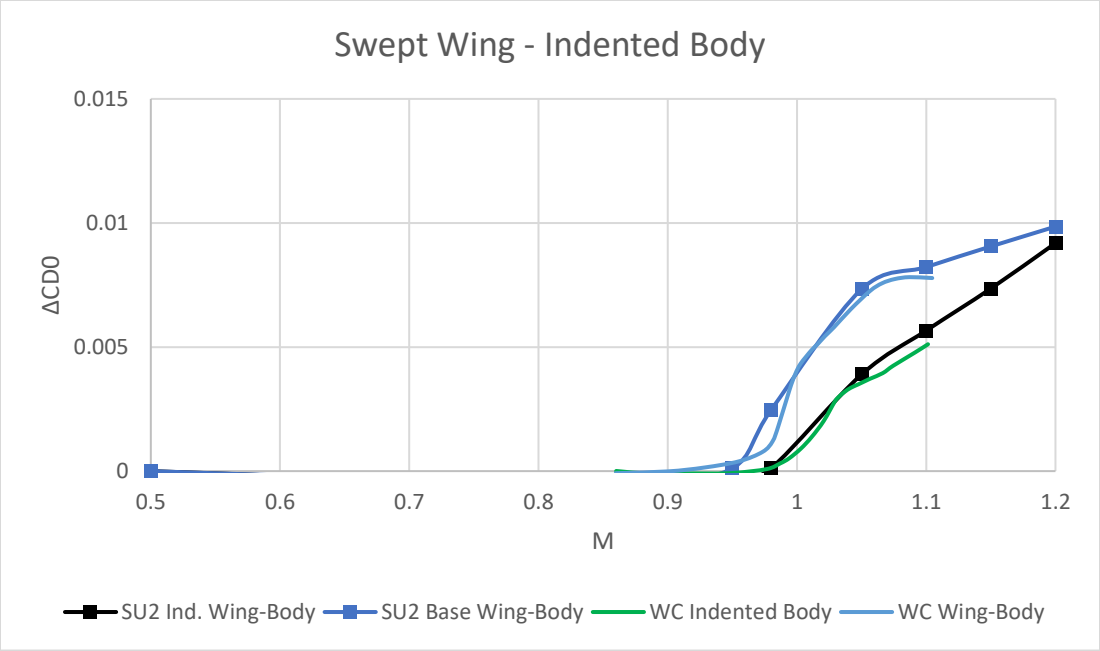

Figure 46. Swept Wing Indented Body Wave Drag Approximations

The case of the swept wing stands alone in its characteristics as it appears to argue Whitcomb's claim fairly well. In this case, the SU2 prediction appears to agree with Whitcomb's data for the indented body case fairly well. Along with this, the SU2 indented body appears to yield a lower drag rise than the SU2 wing-body all the way up to a Mach number of 1.2. The peak reduction in this case appears to happen at a Mach number of 1.05 and is approximately 0.003. It should also be noted that the swept wing case, whether or not it is indented at the body, produces a less extreme drag rise than the other cases.

Thus, concludes the results of the drag rise approximations, which have shown some major disagreement with both of Whitcomb's Transonic Area Rule claims. However, these values do not paint the whole picture of all the mechanisms taking place

in these solutions. This is where the questions arise, what is causing these differences, and how are shock patterns affecting what is seen here? It is for this reason that the surface pressure and local Mach number results of the SU2 solutions were produced.

CHAPTER 6

SURFACE PRESSURE & LOCAL MACH NUMBER RESULTS

In this section there will be many figures of TecPlot solutions with a black band used to demonstrate where the flow either goes from subsonic to supersonic or vice-versa. Data probes are placed a very short distance before and after the shock for each of these cases to collect data on the surface pressure coefficients and local Mach numbers. Along with this, the shock angles will be measured from the line perpendicular to the incoming flow (freestream flows in the positive-x direction). Shocks located directly on the body have their angles measured from the 3-D flow solution vs the surface flow solutions. These shock angles are then used as "sweep" in the table of Küchemann *CP** values discussed in Chapter 2 to determine what Küchemann's *CP** equation would predict to be the pressure coefficients that would cause a shock. It should be noted, however, that there are some *CP* measurements that appear to exceed the range of prediction from the *CP** table. When this occurs, the *CP** column of a table will be filled in with a "N/A." For the measure pressure coefficient values to agree with Küchemann's predictions, one should expect the *CP** value to be at about the halfway point between the *CP* measurements upstream and downstream of the shock.

a. Unswept Wing, Cylindrical Body

In this section are the CFD solutions (mostly surface and some flow) for the Unswept Wing, Cylindrical Body geometry. This section consists of Fig. (47)-Fig. (53) which include figures and the tabulated values of the probe data collected. Refer to Chapter 3, Part e. for instructions on how to read these.

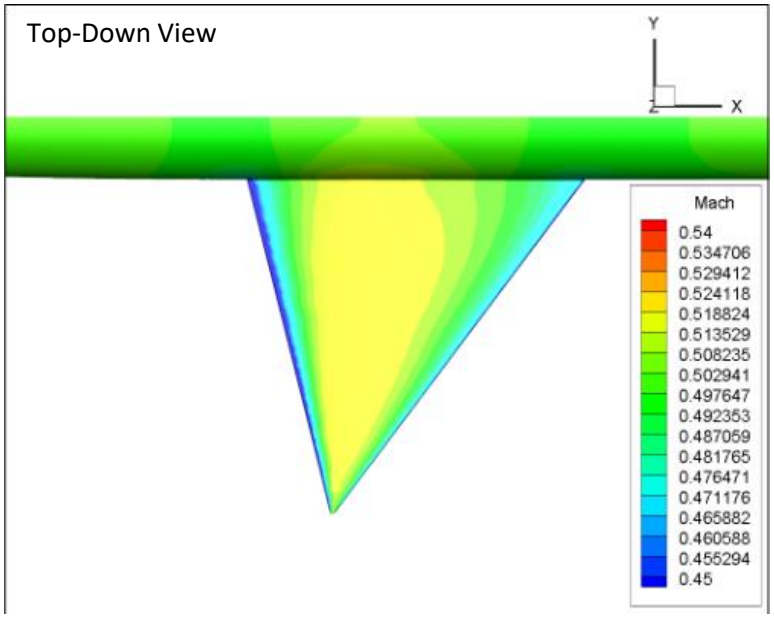

Figure 47. Unswept Wing, Cylindrical Body M=0.5 Solution

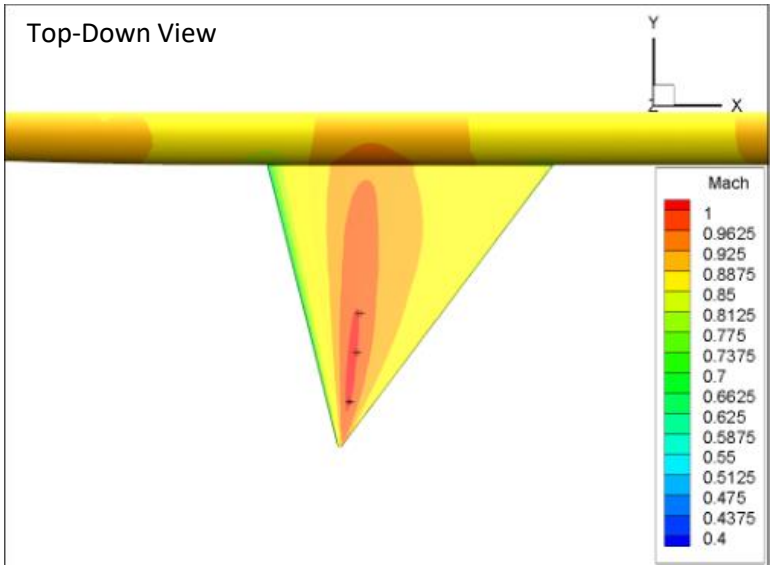

Figure 48. Unswept Wing, Cylindrical Body M=0.88 Solution

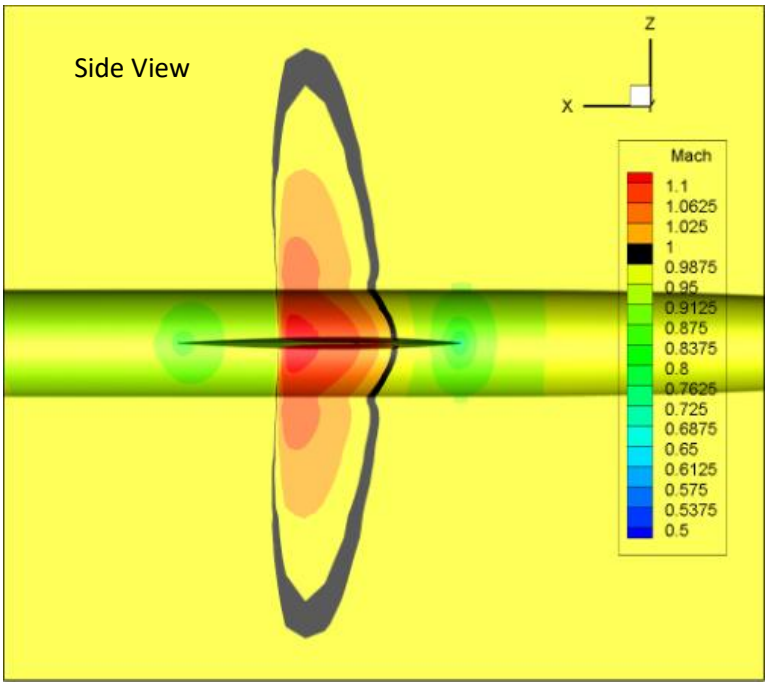

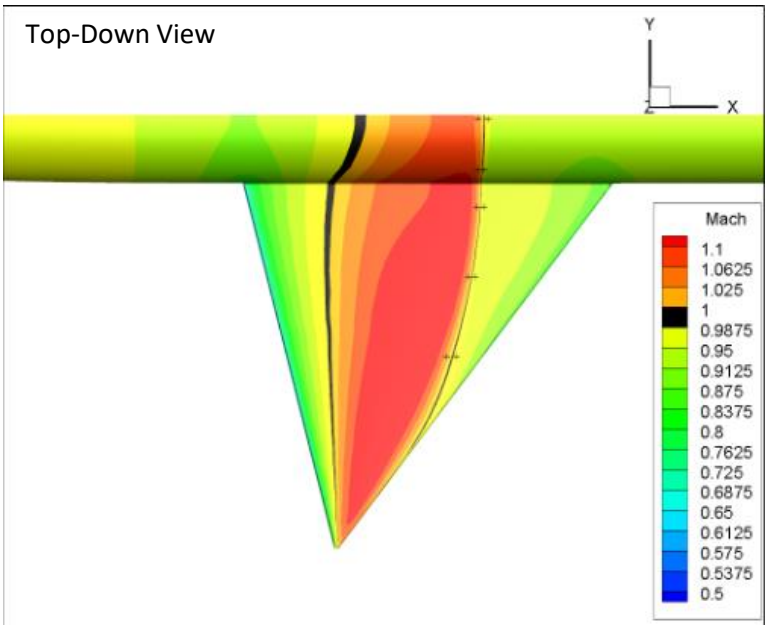

Probes	***CP***	**Mach #**	**Shock Angle (º)**	***CP****
1a	-0.178	1.042	2.3	-0.09
1b	-0.035	0.957		
2a	-0.176	1.038		
2b	-0.050	0.963		

3a	-0.185	1.036	5.9	-0.09
3b	-0.022	0.940		
4a	-0.167	1.027		
4b	-0.038	0.952		
5a	-0.186	1.036	15.8	~-0.14
5b	-0.067	0.967		

Figure 49. Unswept Wing, Cylindrical Body M=0.95 Solution

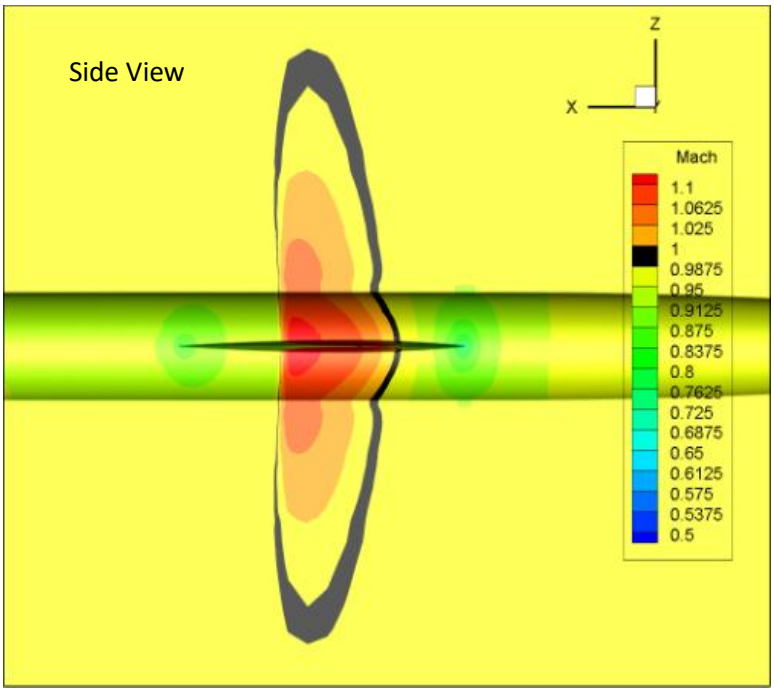

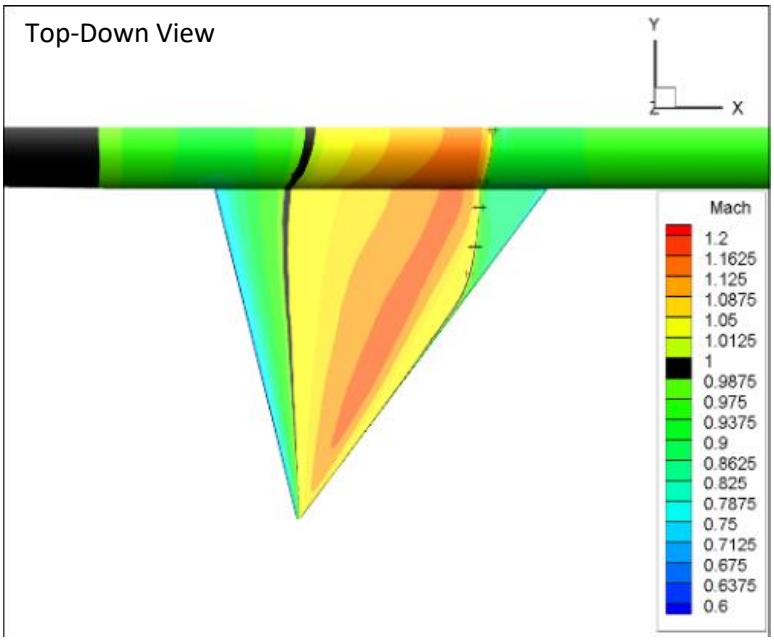

Probes	*CP*	Mach #	Shock Angle (º)	*CP**
1a	-0.106	1.027	8.4	(-0.04)-(-0.06)
1b	0.055	0.930		
2a	-0.107	1.029		
2b	0.068	0.924		
3a	-0.134	1.037	7.6	(-0.04)-(-0.06)
3b	0.050	0.925		
4a	-0.107	1.024		
4b	0.051	0.930		
5a	-0.096	1.020		
5b	0.036	0.938		

Figure 50. Unswept Wing, Cylindrical Body M=0.98 Solution

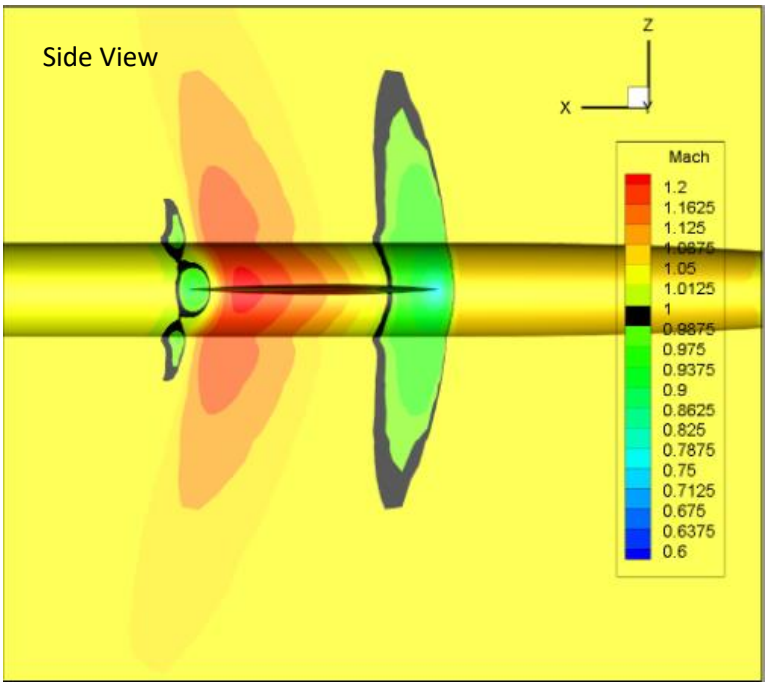

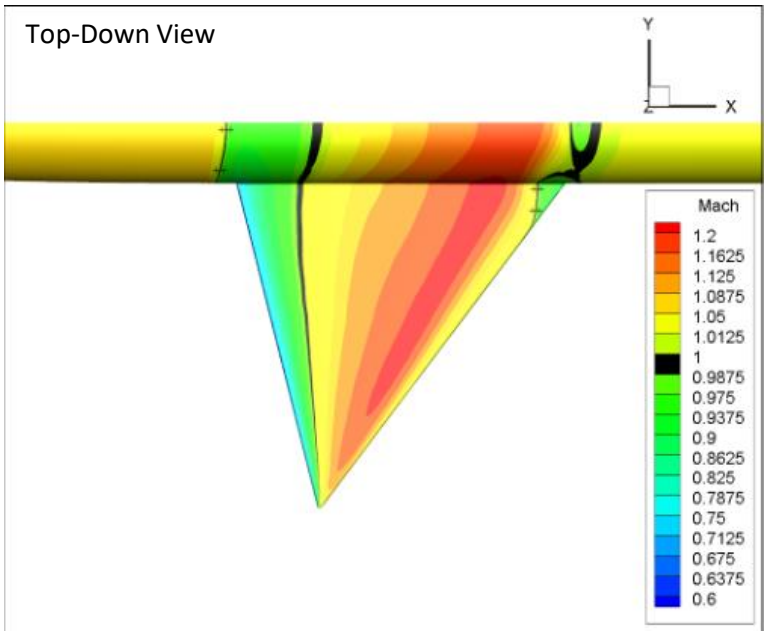

Probes	***CP***	**Mach #**	**Shock Angle (º)**	***CP****
1a	0.024	1.023	9.5	N/A
1b	0.125	0.959		
2a	0.038	1.014		

2b	0.132	0.953		
3a	0.029	1.010	6.1	N/A
3b	0.097	0.967		
4a	0.025	1.013		
4b	0.108	0.960		

Figure 51. Unswept Wing, Cylindrical Body M=1.05 Solution

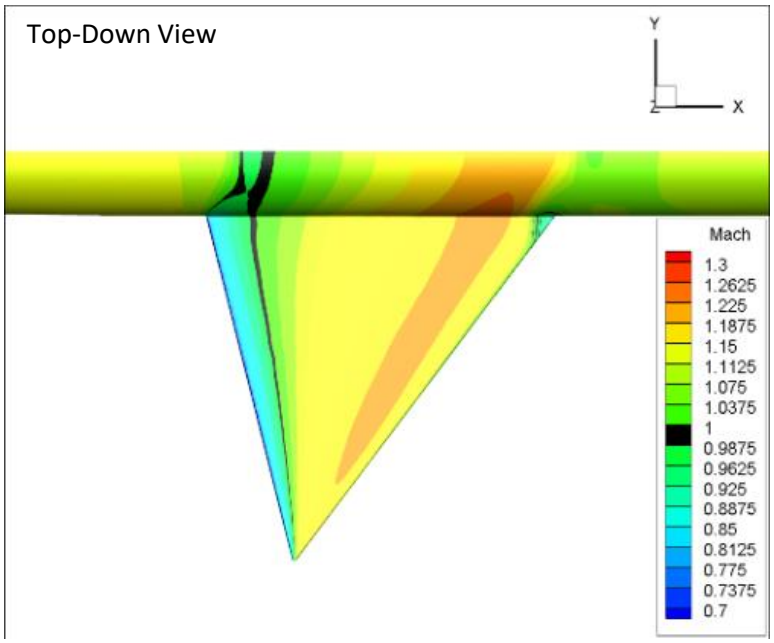

Probes	***CP***	**Mach #**	**Shock Angle (º)**	***CP****
1a	0.086	1.018	4.6	N/A
1b	0.160	0.968		
2a	0.098	1.010		
2b	0.173	0.959		

Figure 52. Unswept Wing, Cylindrical Body M=1.1 Solution

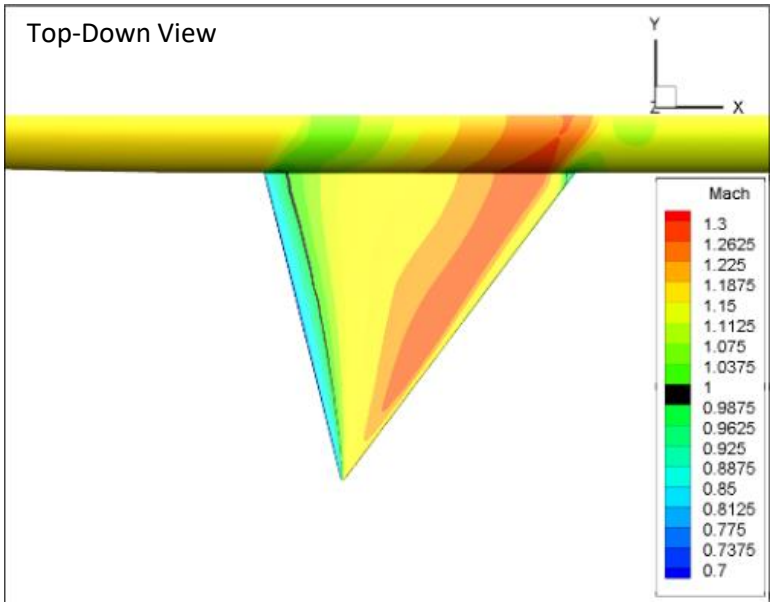

Figure 53. Unswept Wing, Cylindrical Body M=1.15 Solution

Looking at the solutions above, it can be seen that a shock does develop across the wing and on the body starting at the Mach 0.95 solution and appearing to disappear at the Mach 1.15 solution. The shock appears to develop across most of the wing and as the freestream Mach number increases, it moves further toward the trailing edge of the wing. The shock seems to disappear at the trailing edge junction of the wing and body. Along with this, the body does not appear to yield a body shock at the same location for the Mach 1.05 solution. Instead, another body shock appears to form forward of the wing, which again dissipates at higher Mach numbers. Though not shown here, the Mach 1.05 solution also appears to demonstrate the starts of a small bow shock at the nose. As the Mach number is increased however, this bow shock shrinks in size to a point where it is hard to see. Eventually, it appears as though there are no shocks on the body at all. This behavior at the nose is shown in the comparable body section of this geometry.

Looking at the tables of data probe values, it can be seen that there is some odd behavior. When looking at the shock angles for the given freestream Mach numbers, it can be seen that expected Mach cone angles are not recovered. Another interesting behavior is that Küchemann's *CP** equation does appear to predict pressure coefficient values before development of a shock quite well for subsonic freestream solutions. At the supersonic solutions, the equation is no longer able to predict pressure coefficient values as it only covers negative pressure coefficient values. This is relatively odd because a negative pressure coefficient value would go in hand with a local Mach number greater than freestream. Given the way super-velocities function, it would be expected that the flow over the wing before the shock would be greater than freestream. Instead, in every supersonic case, right before the shock, the flow appears to slow down to slightly below freestream.

b. Unswept Wing, Comparable Body

In this section are the CFD solutions (all flow) for the Unswept Wing, Comparable Body geometry. This section consists of Fig. (54)-Fig. (61) which include figures and the tabulated values of the probe data collected. Refer to Chapter 3, Part e. for instructions on how to read these.

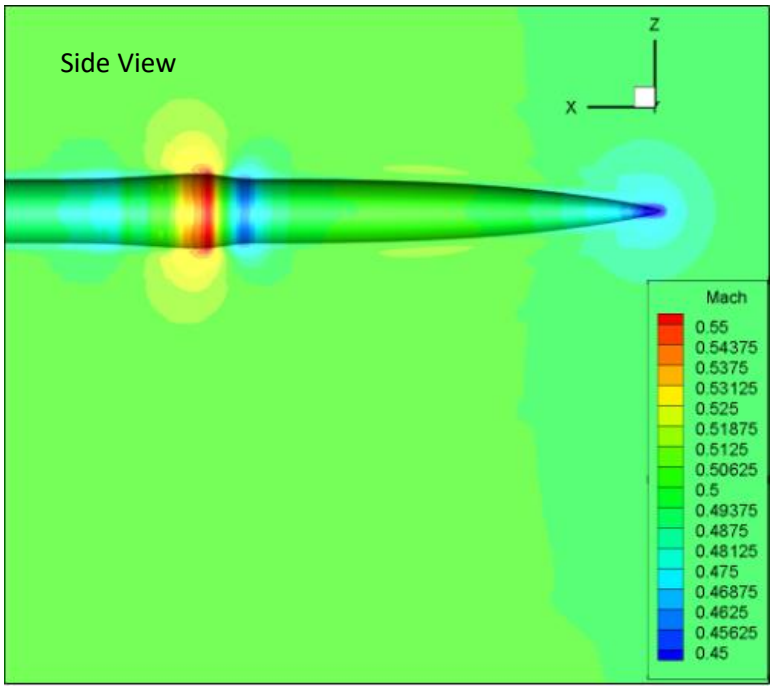

Figure 54. Unswept Wing, Comparable Body M=0.5 Solution

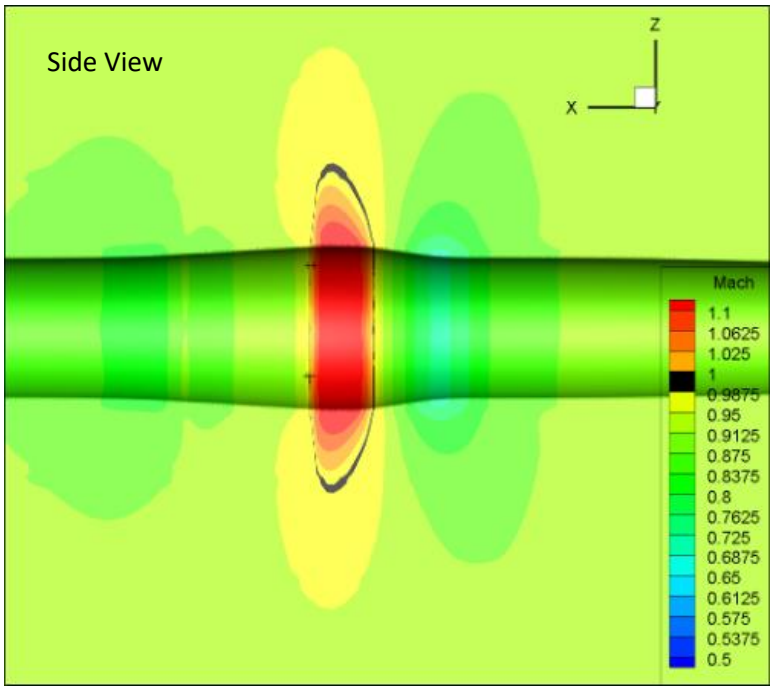

Probes	***CP***	**Mach #**	**Shock Angle (º)**	***CP****
1a	-0.378	1.055	4.3	~-0.19

1b	-0.234	0.976		
2a	-0.361	1.046		
2b	-0.212	0.962		

Figure 55. Unswept Wing, Comparable Body M=0.88 Solution

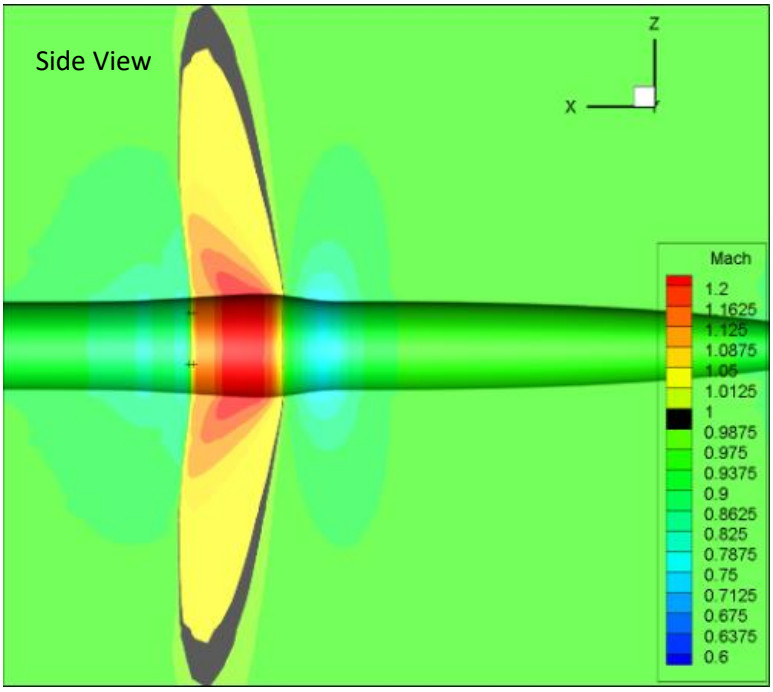

Probes	***CP***	**Mach #**	**Shock Angle (º)**	***CP****
1a	-0.278	1.093	6.9	(-0.09)-(-0.11)
1b	-0.018	0.931		
2a	-0.256	1.077		
2b	-0.010	0.928		

Figure 56. Unswept Wing, Comparable Body M=0.95 Solution

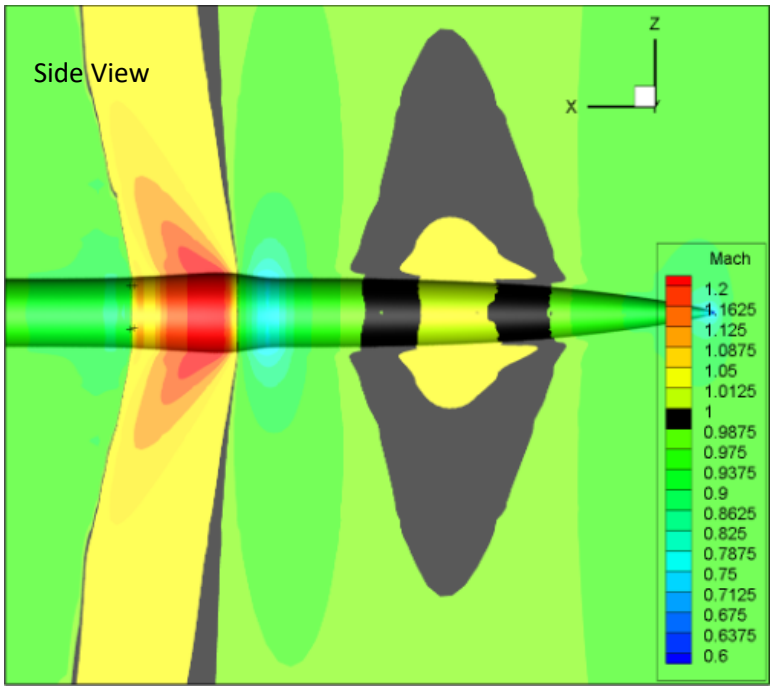

Probes	*CP*	Mach #	Shock Angle (º)	*CP**
1a	-0.141	1.048	11.4	(-0.06)-(-0.07)
1b	0.033	0.944		
2a	-0.138	1.046		
2b	0.033	0.943		

Figure 57. Unswept Wing, Comparable Body M=0.98 Solution

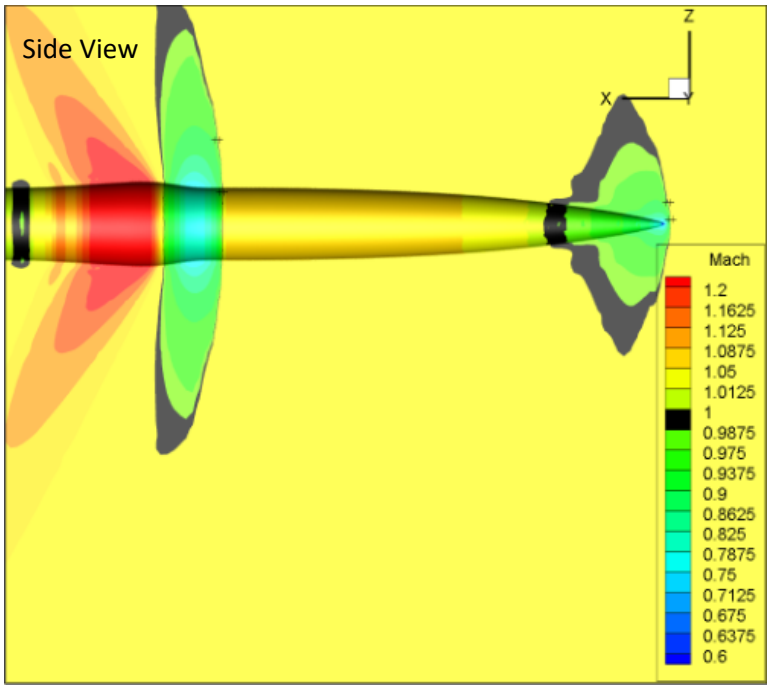

Probes	*CP*	Mach #	Shock Angle (º)	*CP**
1a	0.028	1.031	7.5	N/A
1b	0.162	0.947		
2a	0.003	1.036		
2b	0.128	0.953		
3a	0.021	1.035	9.5	N/A
3b	0.114	0.977		
4a	0.003	1.047		
4b	0.167	0.943		

Figure 58. Unswept Wing, Comparable Body M=1.05 Solution

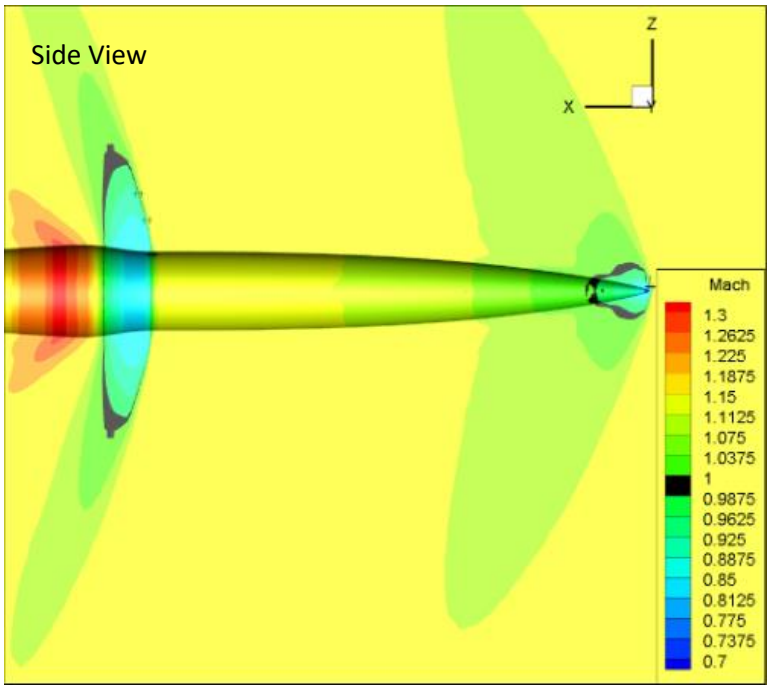

Probes	*CP*	Mach #	Shock Angle (º)	*CP**
1a	0.083	1.043	13.8	N/A
1b	0.209	0.961		
2a	-0.014	1.109		
2b	0.243	0.938		
3a	0.027	1.068		
3b	0.225	0.933		
4a	0.016	1.088	20.4	N/A
4b	0.203	0.965		
5a	0.005	1.096		
5b	0.228	0.934		

Figure 59. Unswept Wing, Comparable Body M=1.1 Solution

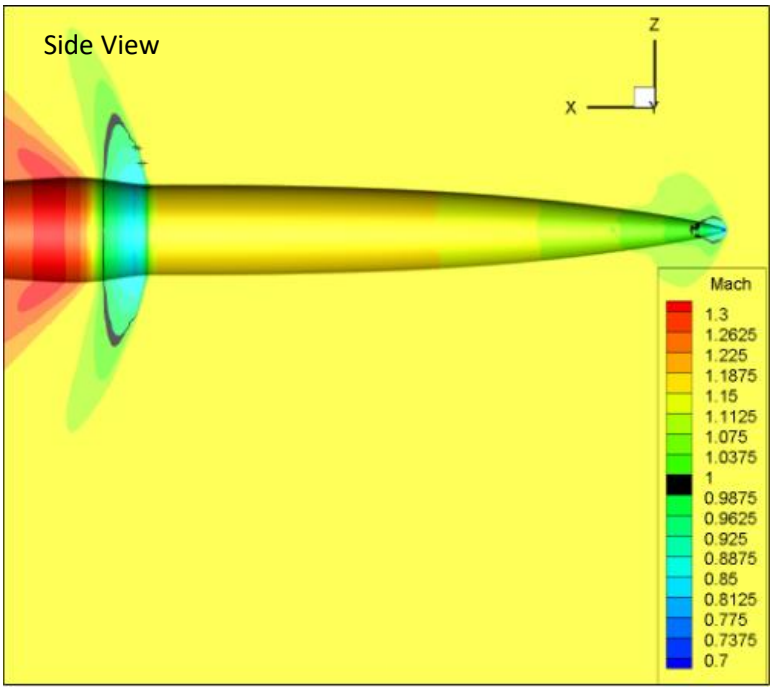

Probes	***CP***	**Mach #**	**Shock Angle (º)**	***CP****
1a	0.108	1.071	16.9	N/A
1b	0.257	0.970		
2a	0.061	1.105		
2b	0.288	0.949		
3a	0.129	1.047		
3b	0.292	0.935		

Figure 60. Unswept Wing, Comparable Body M=1.15 Solution

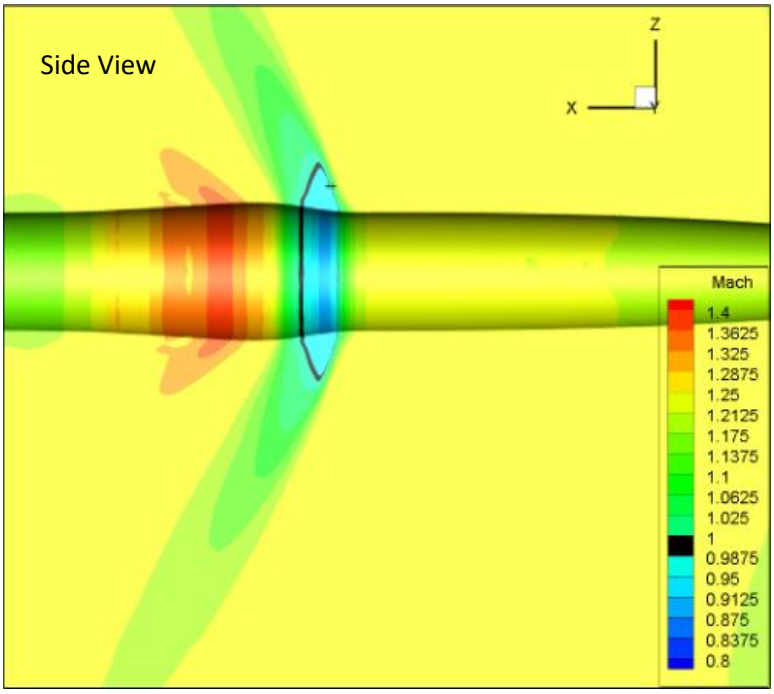

Probes	*CP*	Mach #	Shock Angle (º)	*CP**
1a	0.202	1.049	22.6	N/A
1b	0.315	0.972		
2a	0.213	1.036		
2b	0.307	0.972		

Figure 61. Unswept Wing, Comparable Body M=1.2 Solution

For the comparable body case the shock appears to occur aft of the point of maximum cross-sectional area and progresses aft as the freestream Mach number is increased. However, transitioning from the Mach 0.95 solution to the 1.05 solution, it can be seen that the shock moves forward of the area ruling cross-sectional area development and gradually moves closer to it as the freestream Mach number is increased even more. However, at the Mach 1.05 solution, a bow shock can be seen to develop at the nose of

the body which progressively shrinks. This nose behavior is also present in the base and indented bodies.

Just as in the base body case, this geometry does not return the expected values of Mach cone angles when comparing the measured shock angles. And again, Küchemann's equation appears to predict the pressure coefficients before a shock fairly well with the exception of the Mach 0.88 solution where the predicted *CP** does not fall within the measured range. The most accurate case appears to be the Mach 0.98 case where the predicted value falls almost perfectly at the halfway point of the probe data. At the supersonic solutions, there is an issue of not being able to predict *CP** values again.

c. Unswept Wing, Indented Body

In this section are the CFD solutions (mostly surface and some flow) for the Unswept Wing, Indented Body geometry. This section consists of Fig. (62)-Fig. (69) which include figures and the tabulated values of the probe data collected. Refer to Chapter 3, Part e. for instructions on how to read these.

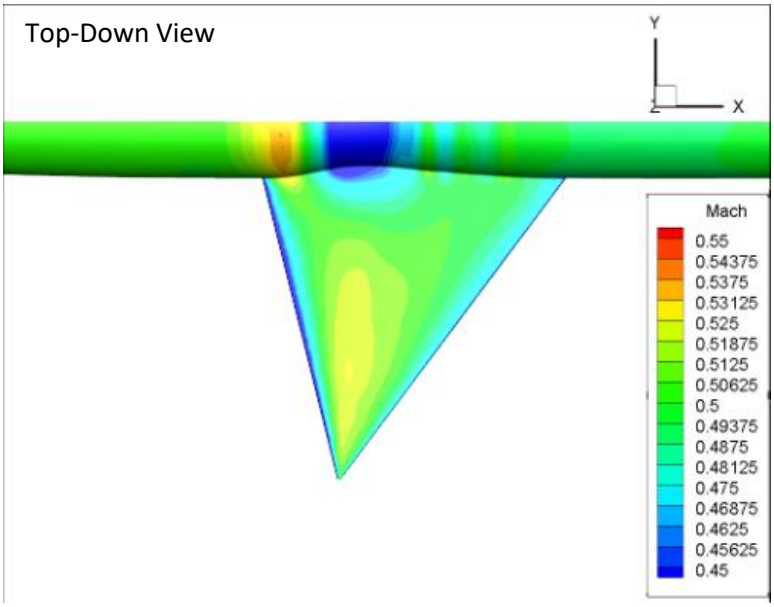

Figure 62. Unswept Wing, Indented Body M=0.5 Solution

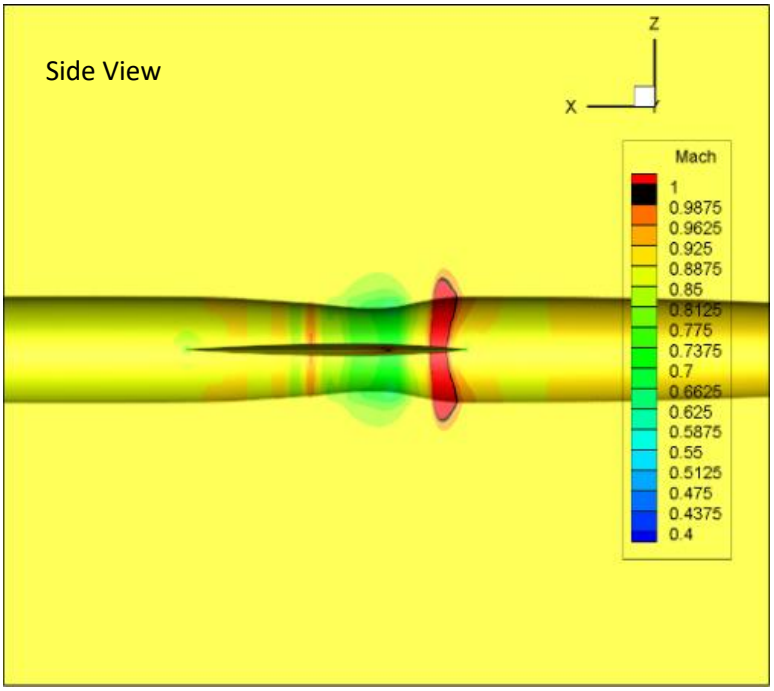

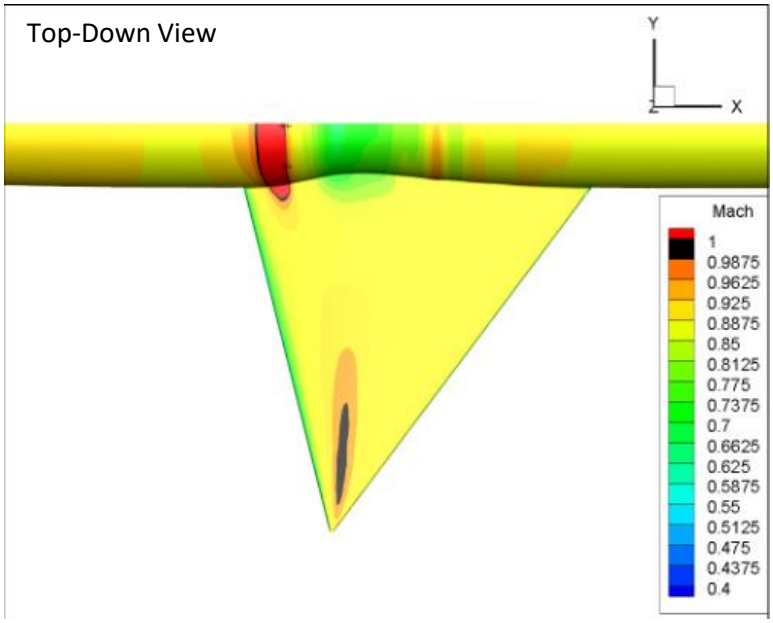

Probes	***CP***	**Mach #**	**Shock Angle (º)**	***CP****
1a	-0.326	1.019	12.8	~(-0.22)-(-0.24)
1b	-0.201	0.947		
2a	-0.320	1.017		
2b	-0.216	0.956		

Figure 63. Unswept Wing, Indented Body M=0.88 Solution

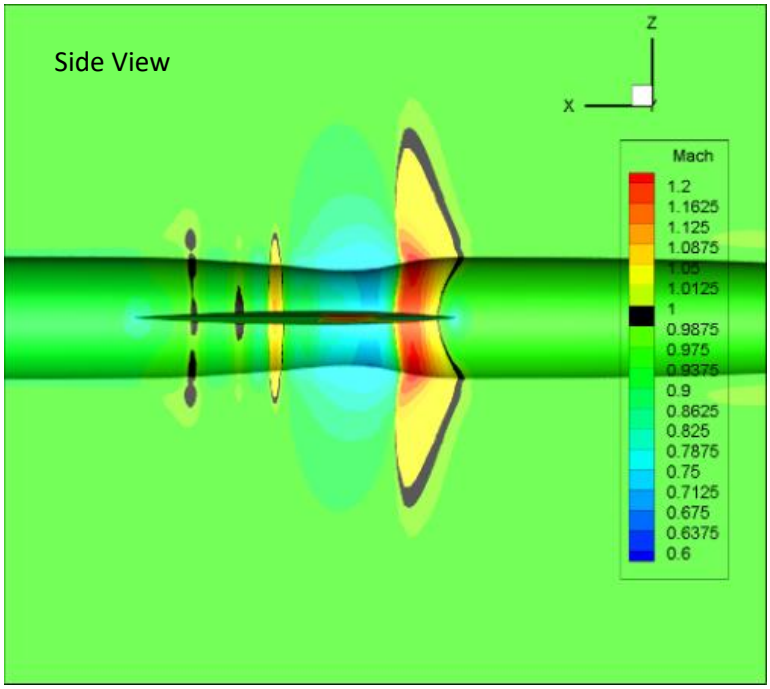

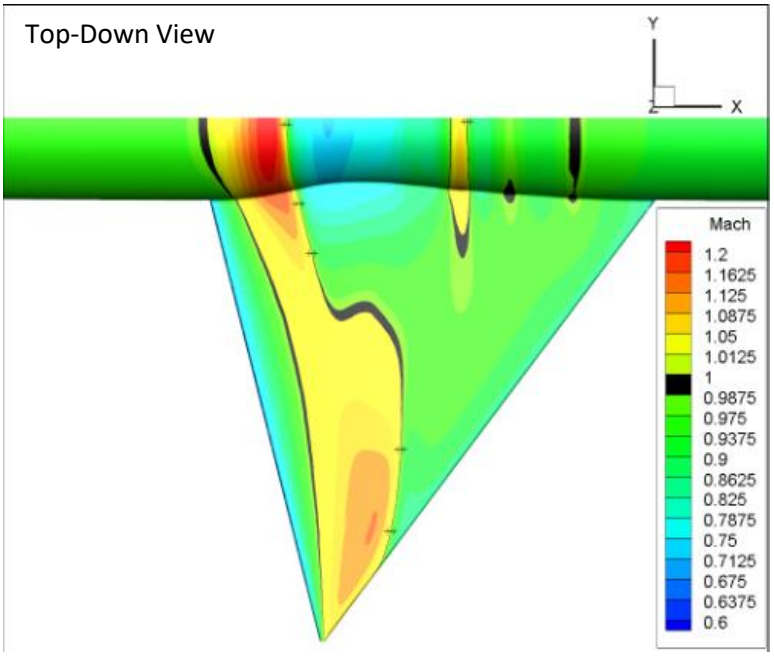

Probes	***CP***	**Mach #**	**Shock Angle (º)**	***CP****
1a	-0.253	1.059	8.2	(-0.09)-(-0.11)
1b	-0.026	0.917		
2a	-0.255	1.066	13.8	

2b	-0.013	0.916		(-0.13)-(-0.14)
3a	-0.173	1.027		
3b	-0.061	0.959		
4a	-0.184	1.032	7.2	(-0.09)-(-0.11)
4b	-0.047	0.951		
5a	-0.212	1.042		
5b	-0.037	0.938		
6a	-0.207	1.023	4.4	-0.09
6b	-0.063	0.939		

Figure 64. Unswept Wing, Indented Body M=0.95 Solution

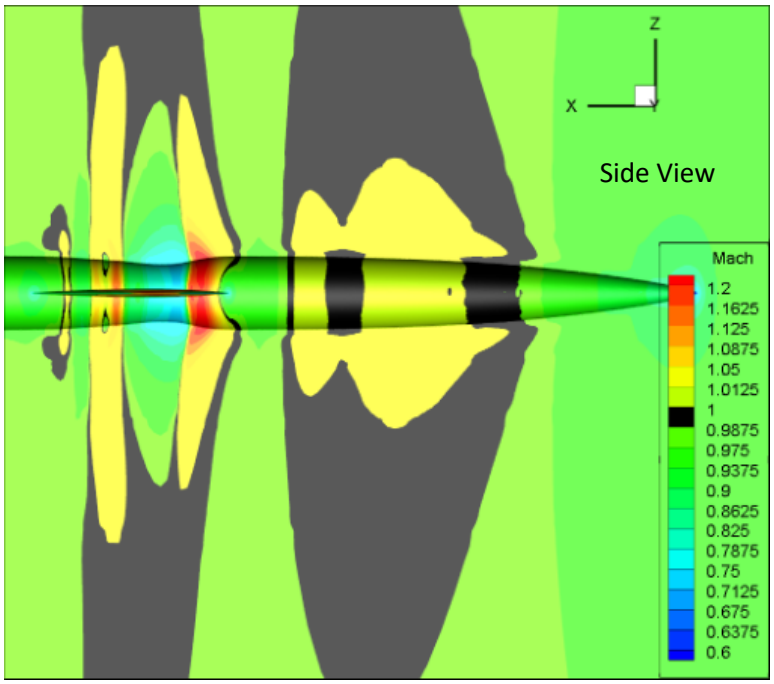

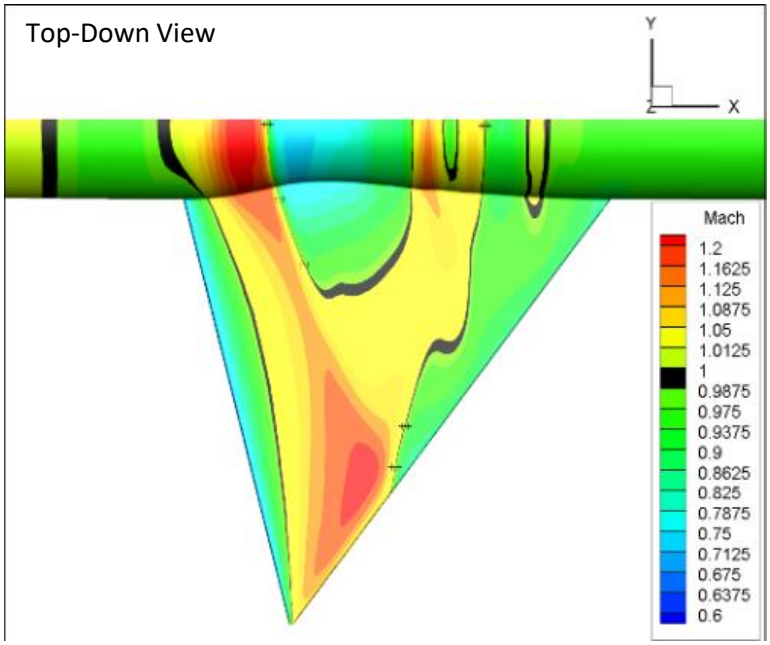

Probes	***CP***	**Mach #**	**Shock Angle (º)**	***CP****
1a	-0.240	1.088	15.9	(-0.09)-(-0.11)
1b	0.051	0.895		
2a	-0.233	1.087	22.4	-0.15
2b	0.085	0.886		
3a	-0.128	1.033		
3b	-0.022	0.969		
4a	-0.106	1.019	15.7	(-0.09)-(-0.11)
4b	-0.005	0.958		
5a	-0.161	1.051		
5b	0.029	0.935		
6a	-0.131	1.018	~0	-0.03
6b	-0.031	0.957		

Figure 65. Unswept Wing, Indented Body M=0.98 Solution

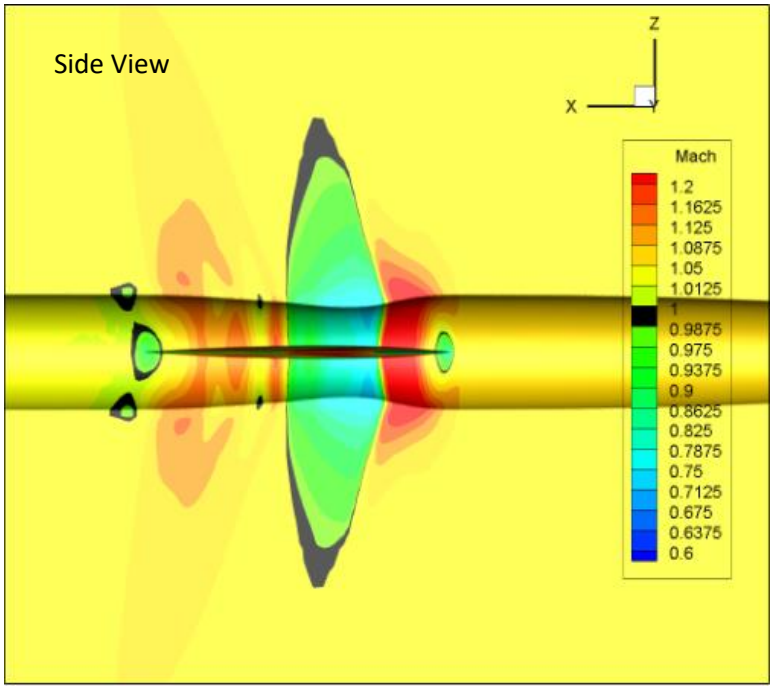

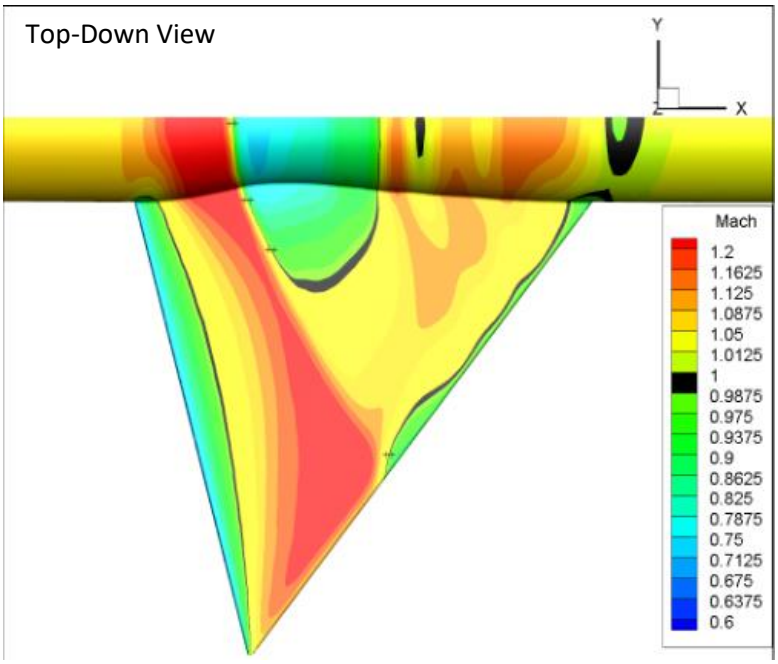

Probes	***CP***	**Mach #**	**Shock Angle (º)**	***CP****
1a	-0.108	1.079	15.6	N/A
1b	0.143	0.903		
2a	-0.112	1.081	27.7	-0.1

2b	0.168	0.890		
3a	-0.008	1.027		
3b	0.091	0.964		
4a	0.004	1.020	27.4	-0.1
4b	0.096	0.961		

Figure 66. Unswept Wing, Indented Body M=1.05 Solution

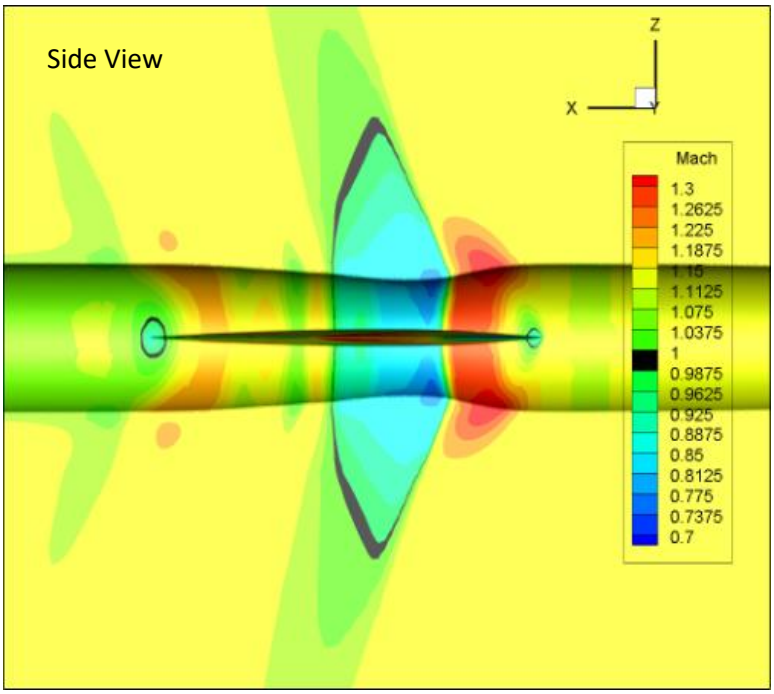

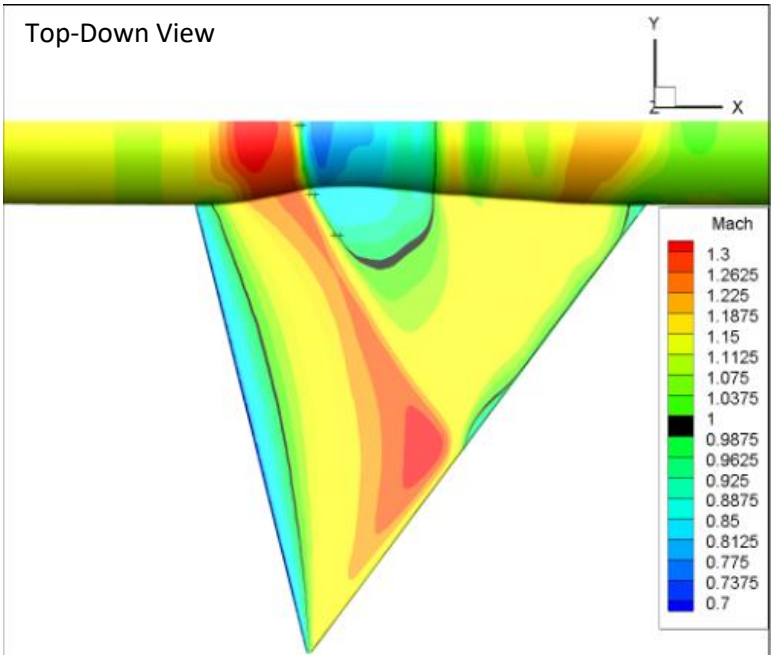

Probes	***CP***	**Mach #**	**Shock Angle (º)**	***CP****
1a	-0.043	1.086	23.8	~0
1b	0.209	0.906		
2a	-0.060	1.093	33.1	(-0.09)-(-0.11)
2b	0.197	0.910		
3a	0.051	1.033		
3b	0.157	0.962		

Figure 67. Unswept Wing, Indented Body M=1.1 Solution

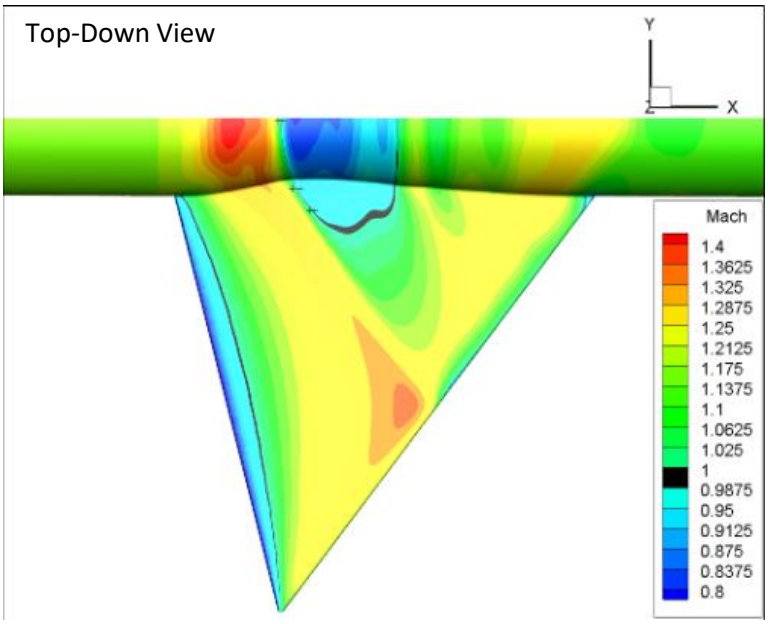

Probes	*CP*	Mach #	Shock Angle (º)	*CP**
1a	0.068	1.062	Unknown	N/A
1b	0.301	0.901		
2a	0.024	1.084	33.7	N/A
2b	0.233	0.934		
3a	0.122	1.020		
3b	0.195	0.971		

Figure 68. Unswept Wing, Indented Body M=1.15 Solution

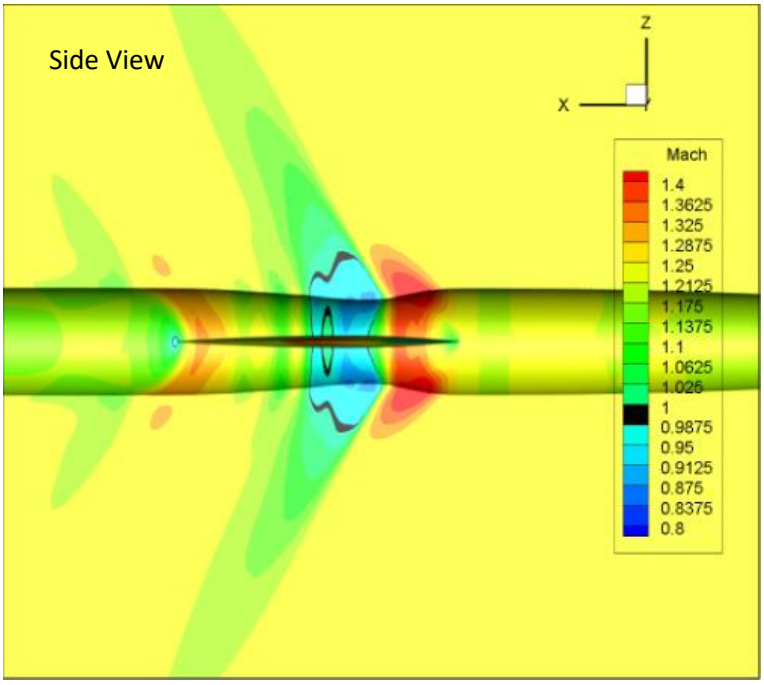

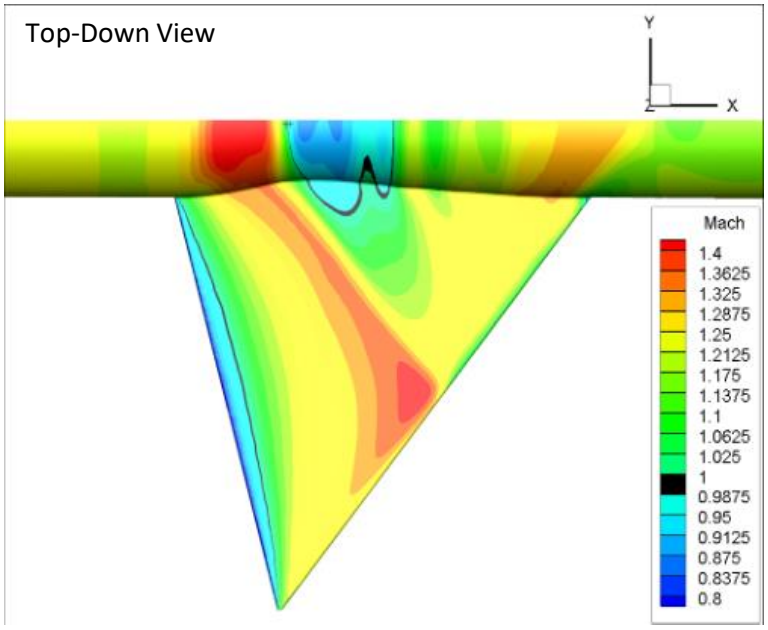

Probes	*CP*	Mach #	Shock Angle (º)	*CP**
1a	0.182	1.035	31.8	N/A
1b	0.326	0.938		

Figure 69. Unswept Wing, Indented Body M=1.2 Solution

In the case of the indented body, the flow conditions are more complex than the base body. A shock first appears on the body forward of the indentation and at a lower Mach number than the base body (0.88 vs 0.95). This shock then appears to “spill” onto the wing along with another shock near the wing-tip. This is seen in the Mach 0.95 solution along with a small body shock aft of the indentation. As the freestream Mach number is increased, the shocks appear to propagate farther and a range of supersonic flow spills over an odd portion of the wing, connecting all regions of shock locations. Eventually the wing shock disappears toward the trailing edge of the wing just as in the base body version, but the shock located forward of the indentation remains even to the Mach number of 1.2. The intensity of the shock appears to be increasing in magnitude as shown by the large drops in Mach number over the shocks at the higher freestream Mach solutions.

In this case there is only one point in which the shock angle does appear to at least coincide with the Mach angle fitted to the local Mach number before the shock. This can be seen in probe 2 of the Mach 0.98 solution. However, given that no other data points seem to agree with this, this point may be just coincidentally fitted. As for the critical pressure coefficient estimates, again the supersonic solutions do not have their shocks predicted. The subsonic solutions do seem to have the predictions fall within the range of measured values, but they are not very centered between said points like they were in the base and comparable body cases.

d. Delta Wing, Cylindrical Body

In this section are the CFD solutions (mostly surface and some flow) for the Delta Wing, Cylindrical Body geometry. This section consists of Fig. (70)-Fig. (75) which include figures and the tabulated values of the probe data collected. Refer to Chapter 3, Part e. for instructions on how to read these.

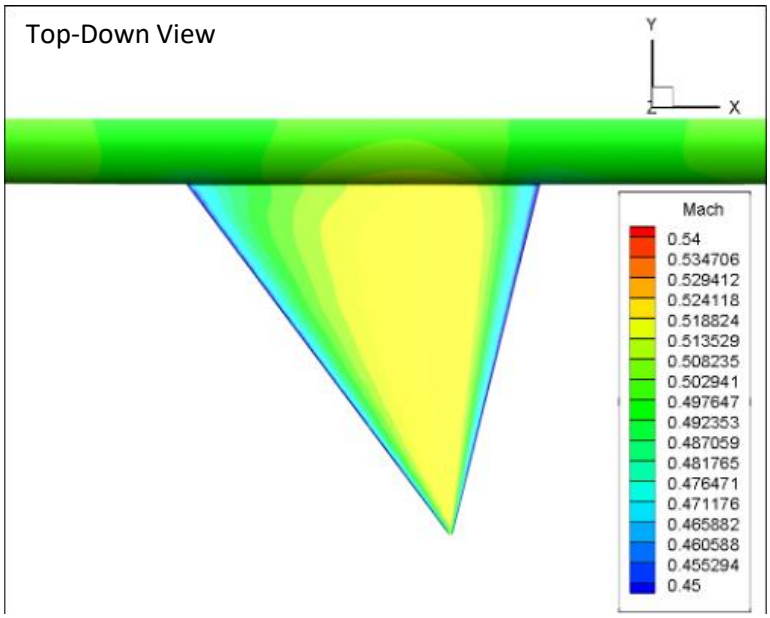

Figure 70. Delta Wing, Cylindrical Body M=0.5 Solution

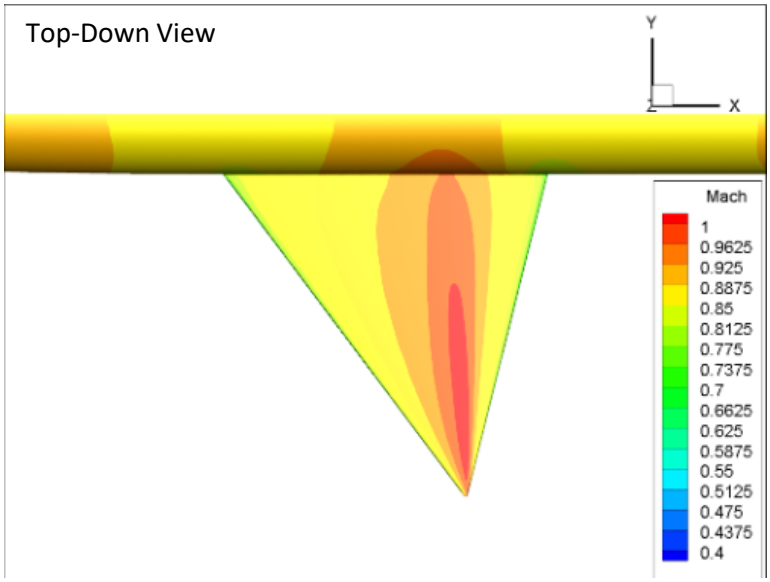

Figure 71. Delta Wing, Cylindrical Body M=0.88 Solution

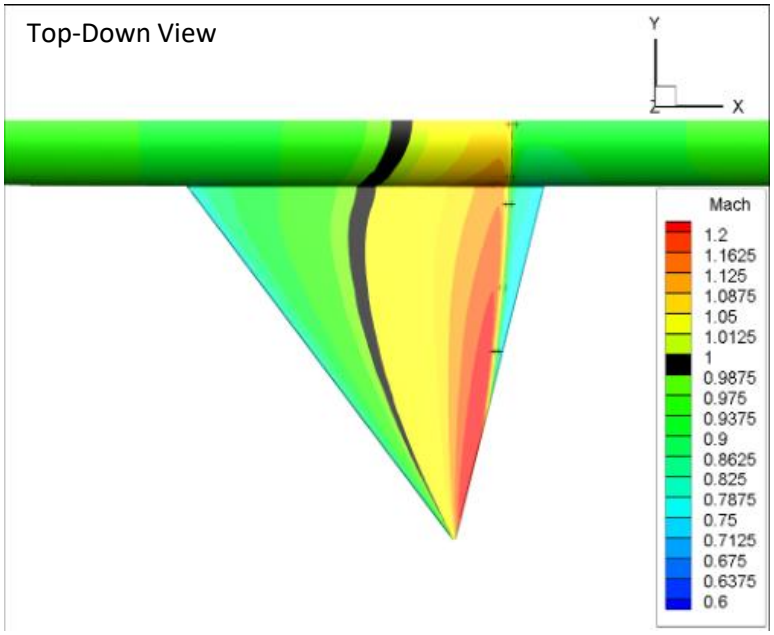

Probes	***CP***	**Mach #**	**Shock Angle (º)**	***CP****
1a	-0.150	1.024	~0	-0.09
1b	-0.029	0.952		
2a	-0.163	1.027		
2b	0.021	0.917		

3a	-0.226	1.058	5.5	-0.09
3b	0.057	0.889		
4a	-0.313	1.114		
4b	0.083	0.866		
5a	-0.374	1.151		
5b	0.091	0.852		

Figure 72. Delta Wing, Cylindrical Body M=0.95 Solution

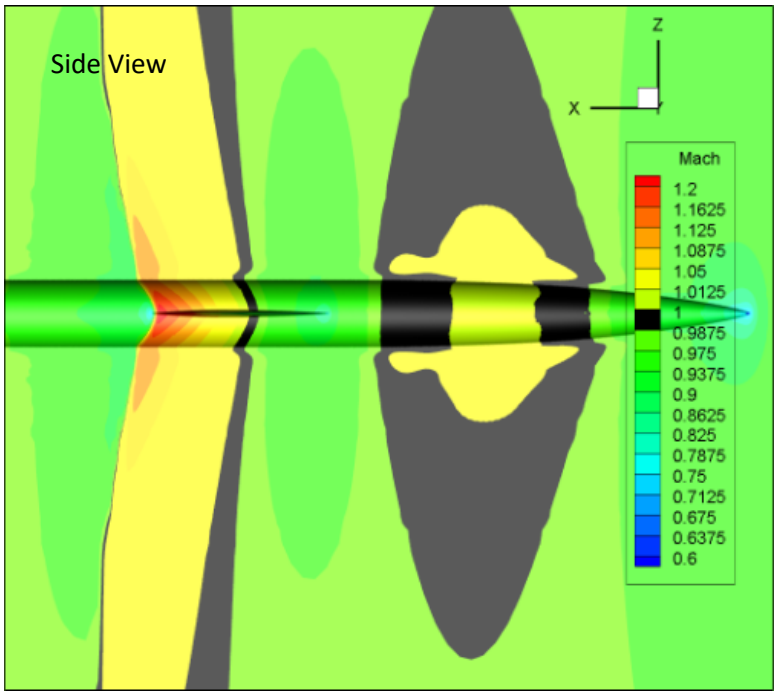

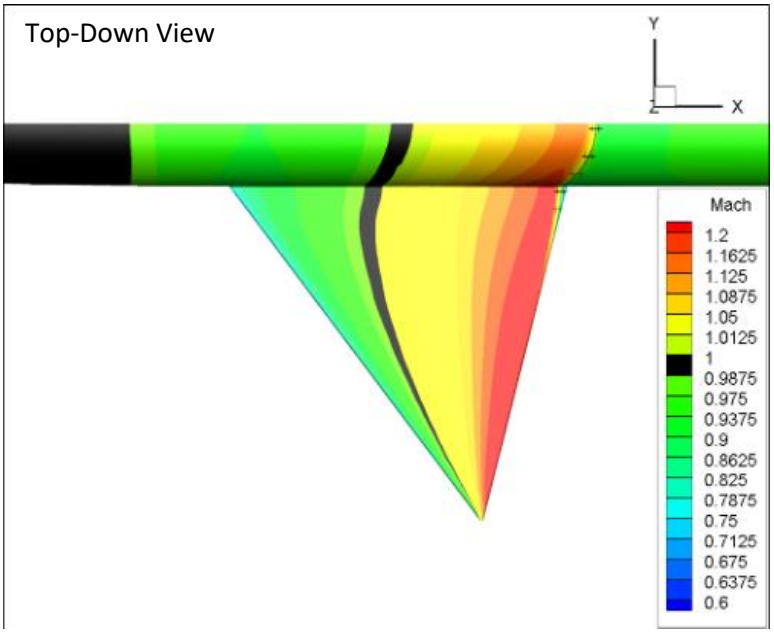

Probes	*CP*	Mach #	Shock Angle (º)	*CP**
1a	-0.119	1.034	9.7	-0.06
1b	0.040	0.936		
2a	-0.110	1.032		
2b	0.018	0.953		
3a	-0.146	1.048		
3b	0.054	0.930		
4a	-0.234	1.094	9.9	-0.06
4b	0.139	0.851		
5a	-0.289	1.134		
5b	0.155	0.817		

Figure 73. Delta Wing, Cylindrical Body M=0.98 Solution

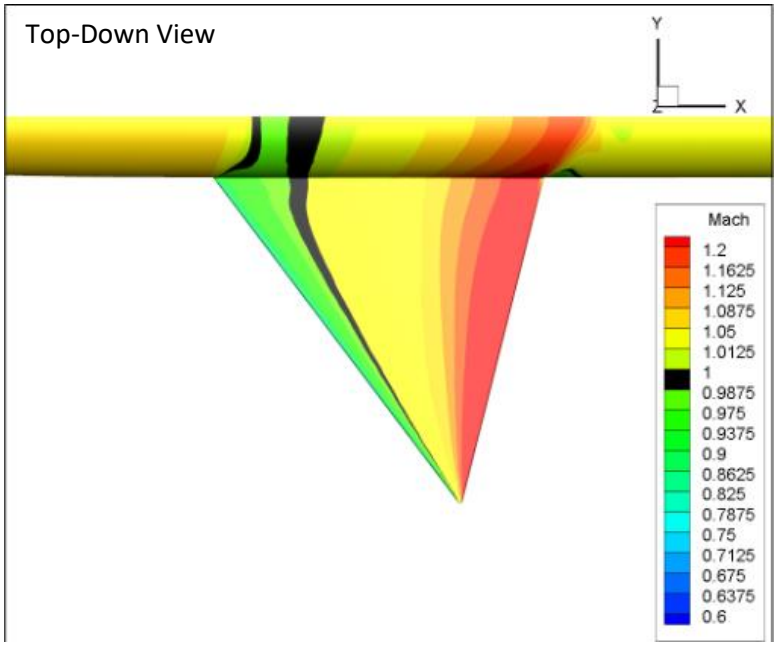

Figure 74. Delta Wing, Cylindrical Body M=1.05 Solution

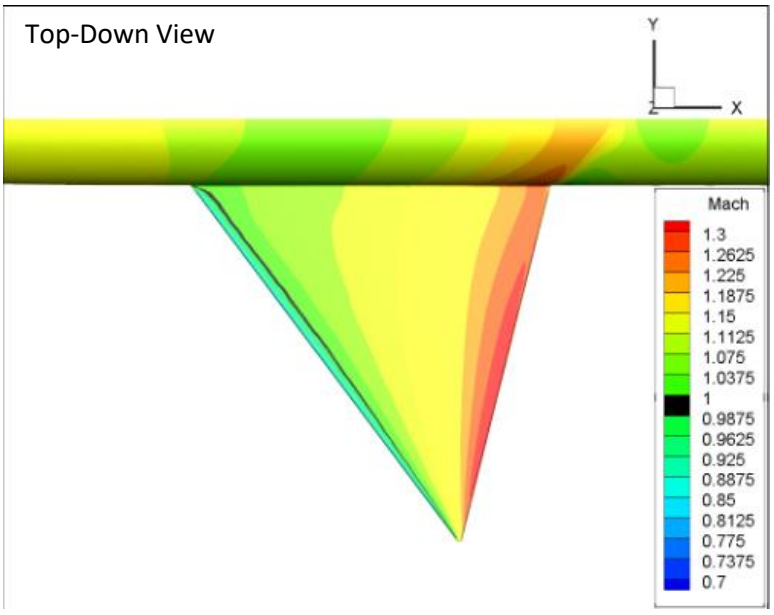

Figure 75. Delta Wing, Cylindrical Body M=1.1 Solution

The base body delta wing solutions show a shock appear across the body and the wing at the Mach 0.95 solution. As the Mach number is increased, the shock appears to

move further down the body and wing seem to be attached until the shock just about disappears at the Mach 1.05 solution. Past this point, there are no shocks on the aft body or the wing. A bow shock is demonstrated in the comparable body solution later, however.

The story is the same here as for the other bodies in that the Mach cone angles and the shock angles do not coincide for freestream or local Mach numbers. The critical pressure coefficient prediction is somewhat the same in that the *CP** prediction values do appear to fall within the ranges of measured data points and are fairly close to being within the middle. However, there are no shocks in the supersonic solutions to predict any critical pressure coefficients here, so a comparison cannot be made.

e. Delta Wing, Comparable Body

In this section are the CFD solutions (all flow) for the Delta Wing, Comparable Body geometry. This section consists of Fig. (76)-Fig. (83) which include figures and the tabulated values of the probe data collected. Refer to Chapter 3, Part e. for instructions on how to read these.

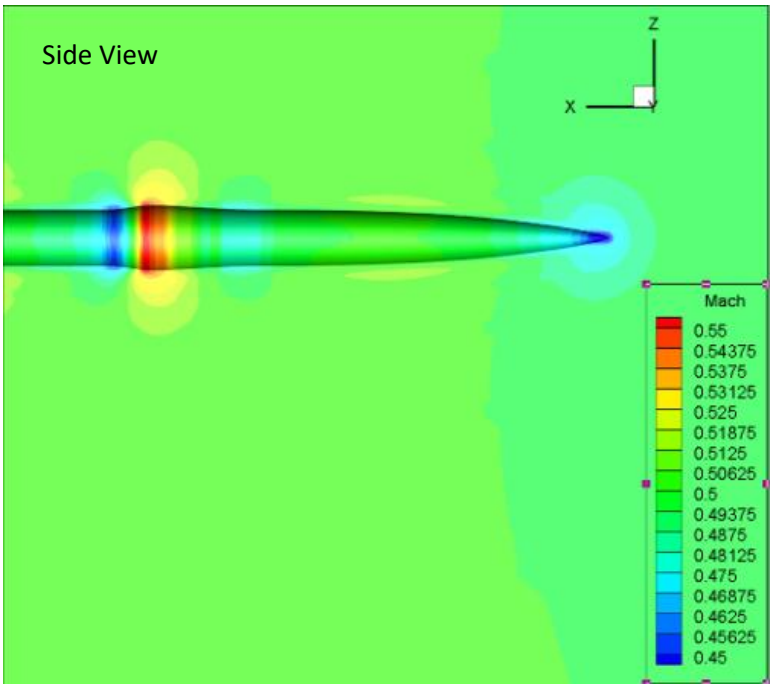

Figure 76. Delta Wing, Comparable Body M=0.5 Solution

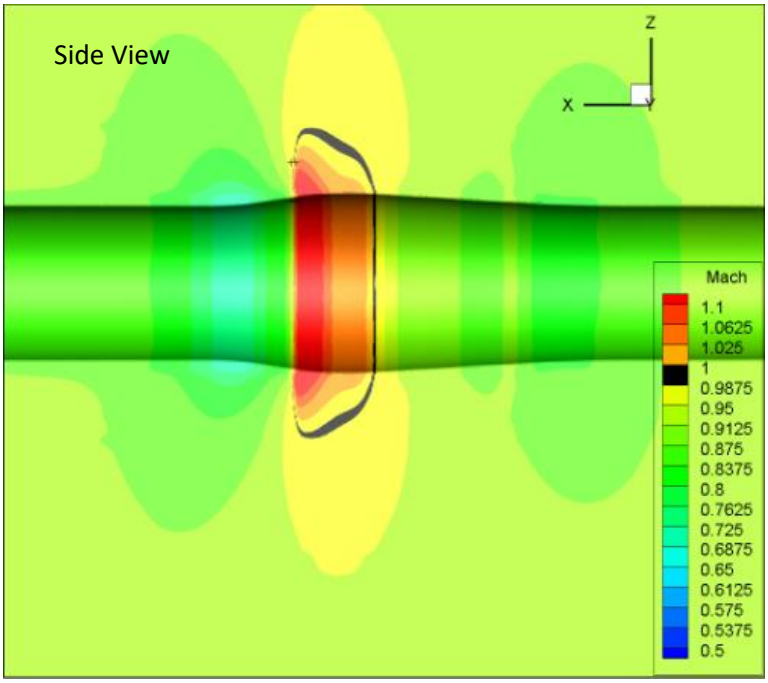

Probes	***CP***	**Mach #**	**Shock Angle (º)**	***CP****
1a	-0.316	1.043	~0	-0.19

1b	-0.142	0.950		
2a	-0.462	1.087		
2b	-0.196	0.930		

Figure 77. Delta Wing, Comparable Body M=0.88 Solution

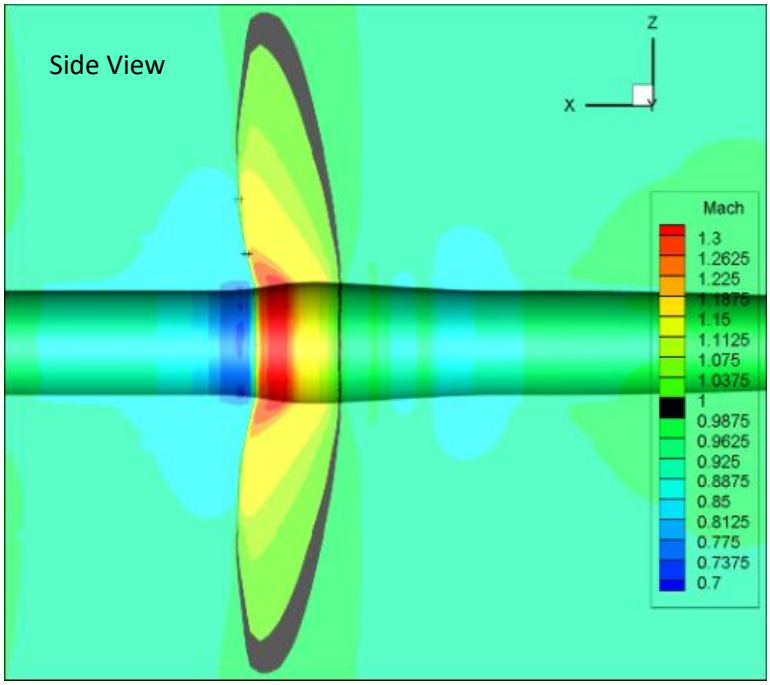

Probes	***CP***	**Mach #**	**Shock Angle (º)**	***CP****
1a	-0.223	1.076	4.4	-0.09
1b	0.047	0.921		
2a	-0.392	1.180	18.3	(-0.16)-(-0.18)
2b	0.129	0.863		
3a	-0.423	1.175		
3b	0.035	0.871		

Figure 78. Delta Wing, Comparable Body M=0.95 Solution

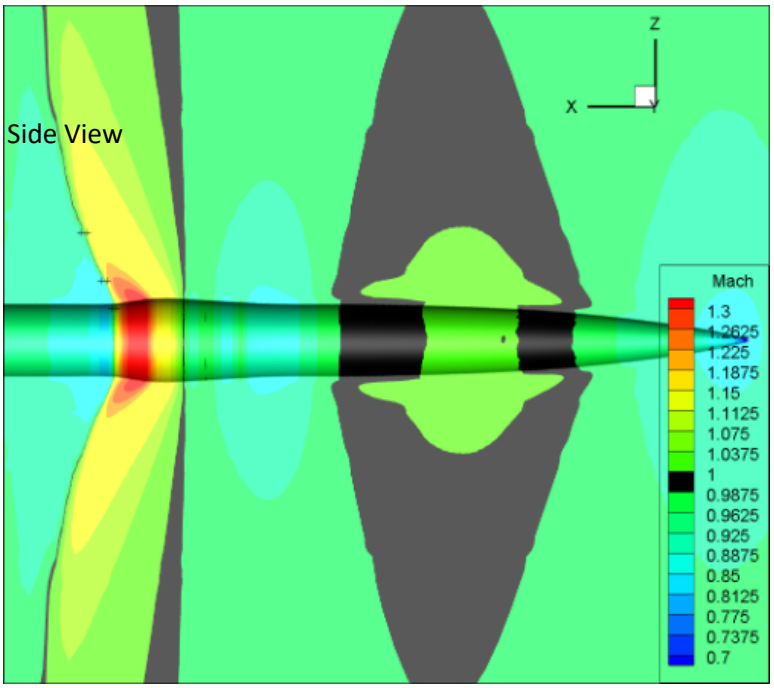

Probes	*CP*	Mach #	Shock Angle (º)	*CP**
1a	-0.162	1.075	23.1	(-0.15)-(-0.18)
1b	0.042	0.952		
2a	-0.285	1.151		
2b	0.099	0.913		
3a	-0.272	1.133		
3b	0.096	0.903		

Figure 79. Delta Wing, Comparable Body M=0.98 Solution

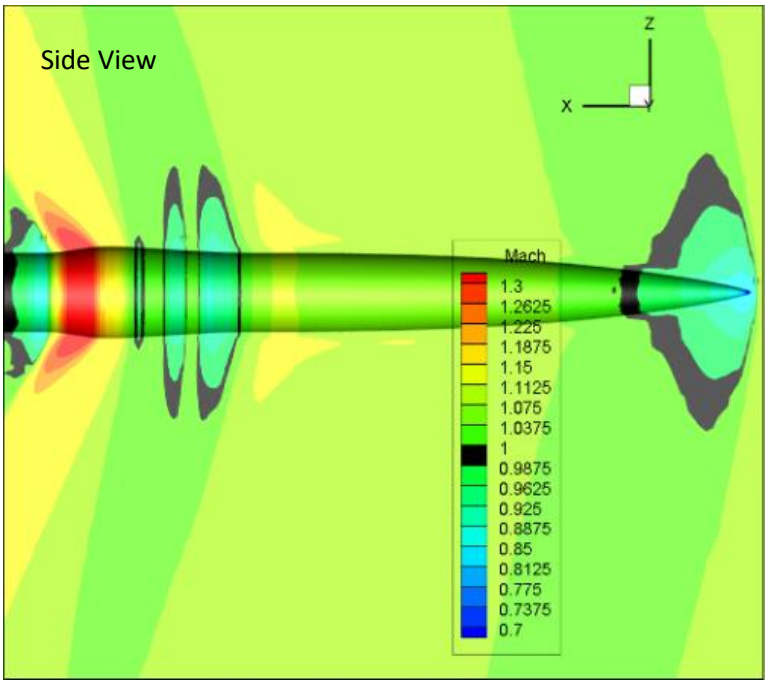

Probes	*CP*	Mach #	Shock Angle (º)	*CP**
1a	-0.045	1.071	30	-0.13
1b	0.136	0.955		
2a	-0.053	1.073		
2b	0.137	0.950		
3a	0.038	1.025	8.2	N/A
3b	0.119	0.974		
4a	0.028	1.019		
4b	0.102	0.973		
5a	0.001	1.049	10.2	N/A
5b	0.150	0.954		

Figure 80. Delta Wing, Comparable Body M=1.05 Solution

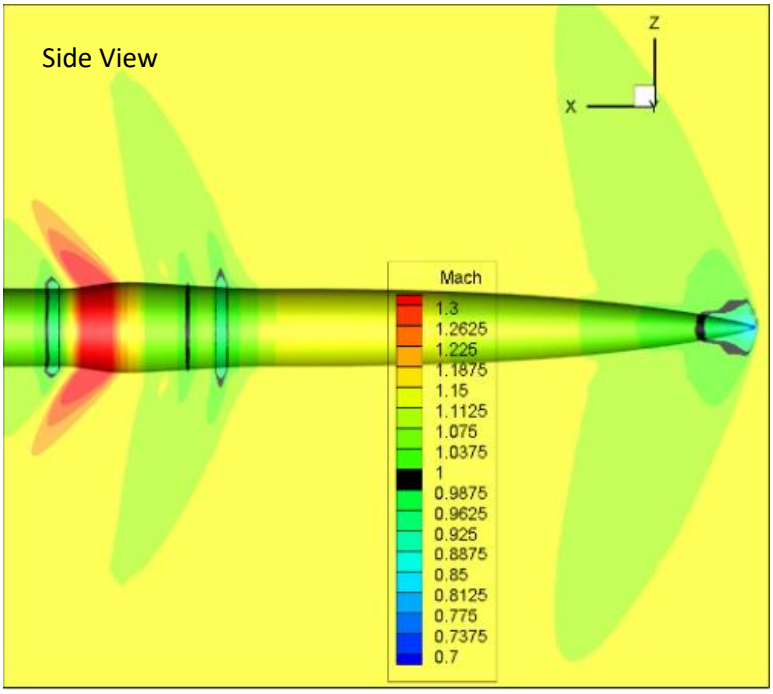

Probes	*CP*	Mach #	Shock Angle (º)	*CP**
1a	0.043	1.070	20.7	N/A
1b	0.185	0.976		
2a	0.027	1.081		
2b	0.161	0.987		

Figure 81. Delta Wing, Comparable Body M=1.1 Solution

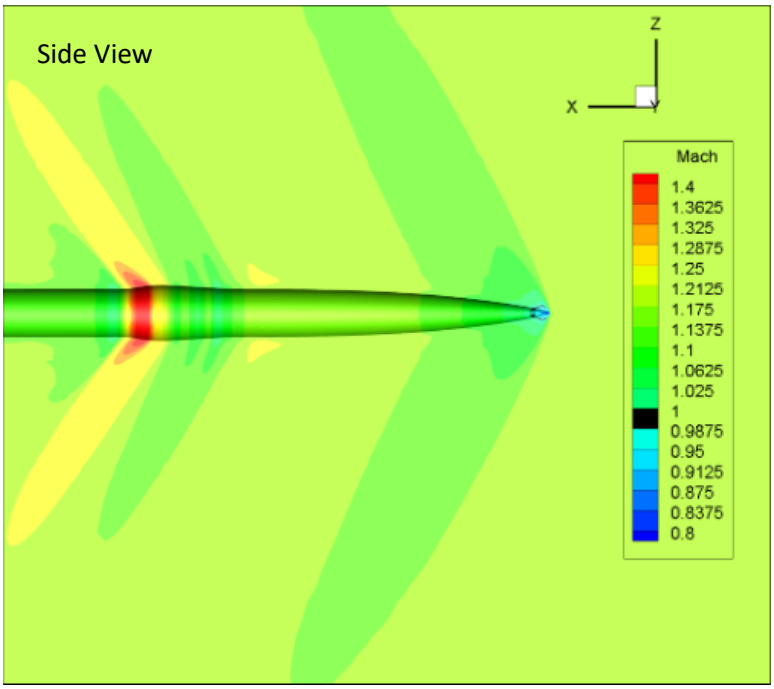

Figure 82. Delta Wing, Comparable Body M=1.15 Solution

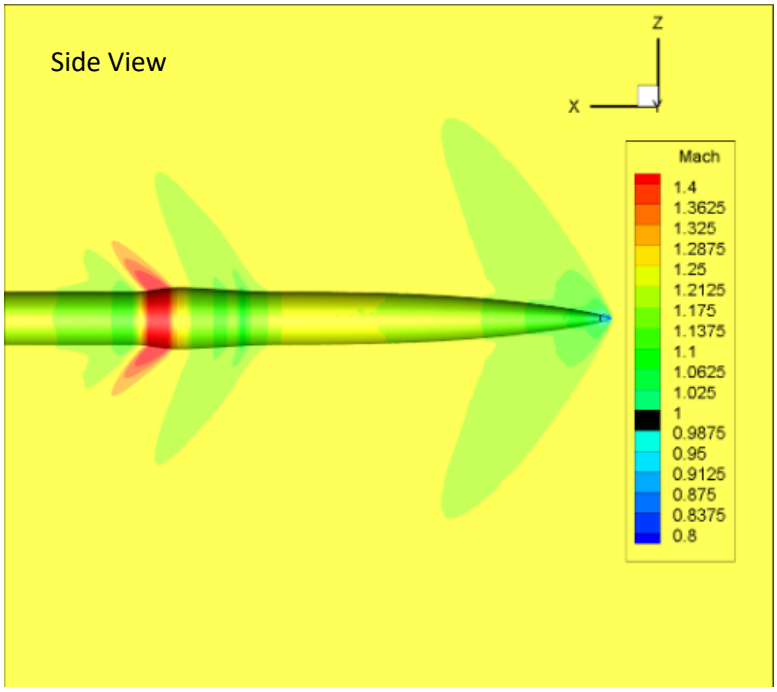

Figure 83. Delta Wing, Comparable Body M=1.2 Solution

The delta wing comparable body appears to behave similarly to the unswept case in that the shock begins aft of the point of maximum cross-sectional area at the Mach 0.88 solution and moves further aft as the Mach number is increased. However, when the freestream Mach number becomes supersonic, the shock moves forward of that point but with multiple regions that could nearly be shock waves. Along with this, in the Mach 1.05 solution, there appears to still be a shock aft of that point. Thus, there are two shocks on the aft body, one in front of the point of maximum cross-sectional area and one aft. It is in this solution that the bow shock at the nose first appears as well. The behavior of the bow shock appears in the base body and indented body cases as well. As the Mach number is increased further, the bow shock shrinks and there are no longer any shocks on the aft body.

There is another outlier in the data where the Mach cone angle and shock angle for the local Mach number before the shock agree with some accuracy. This is shown in probe 1 of the Mach 1.1 solution where the Mach cone angle for a Mach number of 1.07 would be 20.84 degrees and the measured shock angle was 20.7 degrees. Again, however, no other data points within this collection appear to argue this case. As for the critical pressure coefficient prediction, the subsonic solutions are predicted fairly accurately. As points are collected further off the body, however, the accuracy appears to drop off as they steer away from the center of the range of collected data. The supersonic solutions are not able to be predicted once more as in all of the previous cases.

f. Delta Wing, Indented Body

In this section are the CFD solutions (some surface and some flow) for the Delta Wing, Indented Body geometry. This section consists of Fig. (84)-Fig. (91) which include figures and the tabulated values of the probe data collected. Refer to Chapter 3, Part e. for instructions on how to read these.

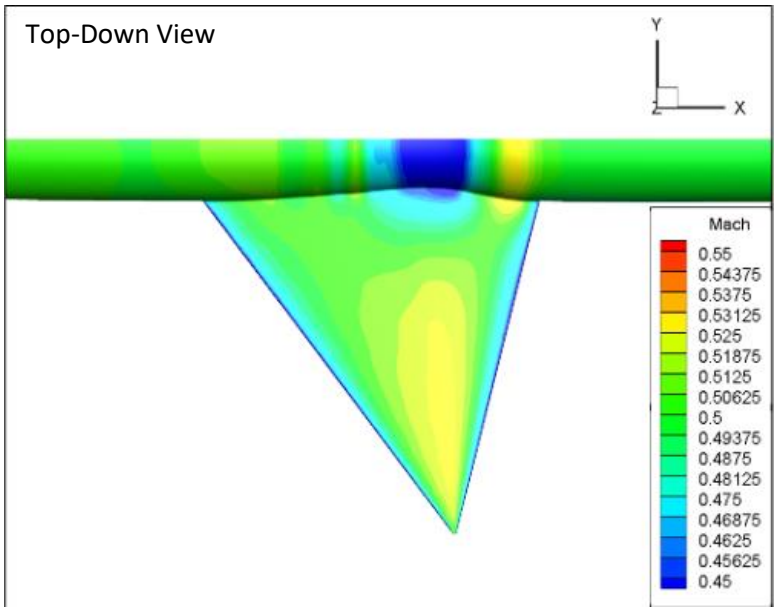

Figure 84. Delta Wing, Indented Body M=0.5 Solution

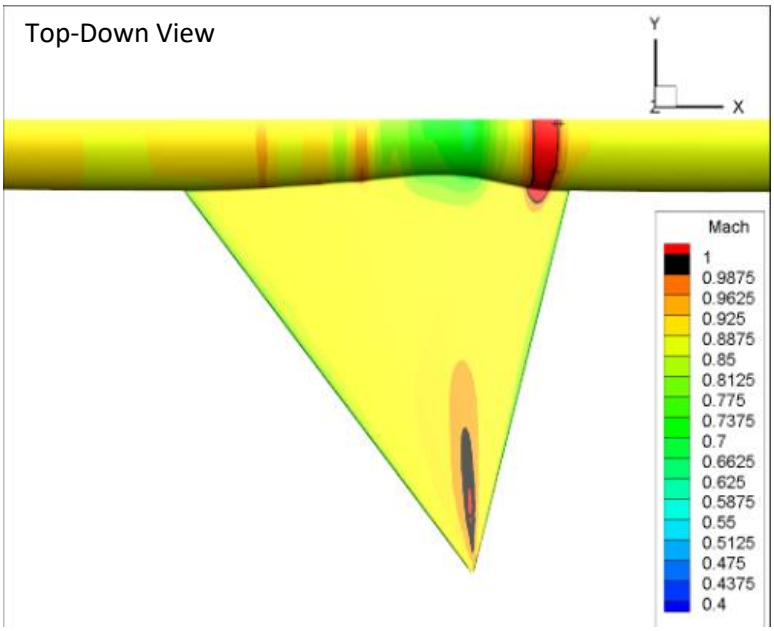

Probes	*CP*	Mach #	Shock Angle (º)	*CP**
1a	-0.318	1.012	Unknown	N/A
1b	-0.239	0.968		
2a	-0.307	1.005		
2b	-0.237	0.966		

Figure 85. Delta Wing, Indented Body M=0.88 Solution

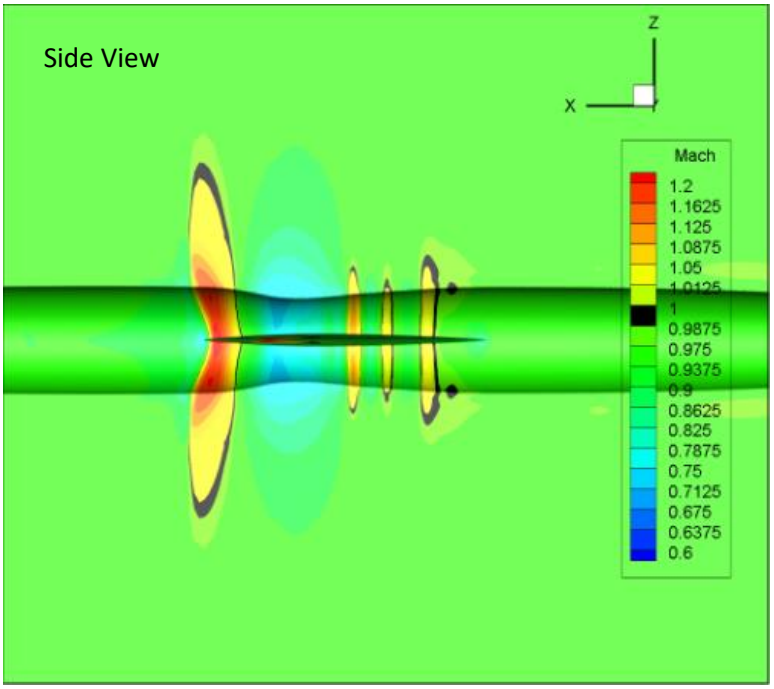

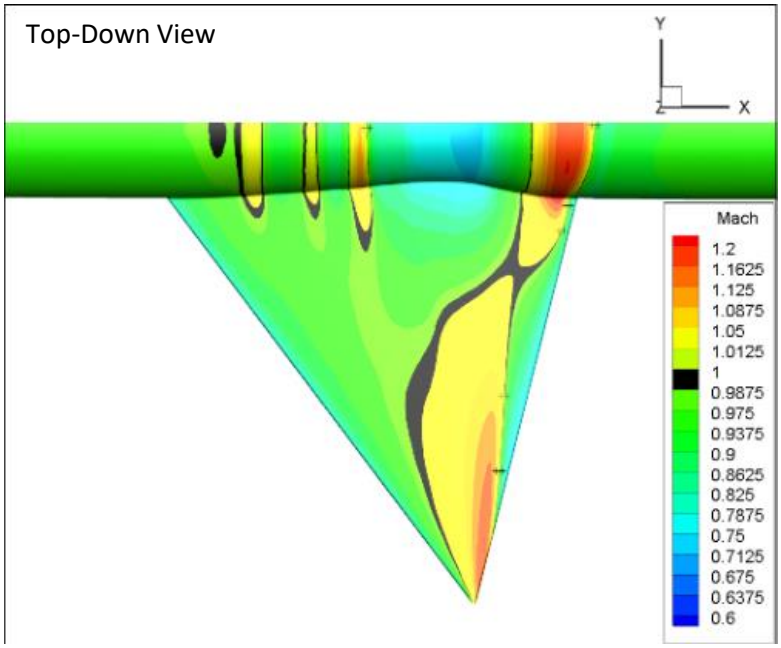

Probes	***CP***	**Mach #**	**Shock Angle (º)**	***CP****
1a	-0.220	1.044	~0	-0.09
1b	-0.036	0.935		
2a	-0.193	1.041	4.1	-0.09

2b	-0.024	0.939		
3a	-0.269	1.079		
3b	0.026	0.891		
4a	-0.214	1.036	14.8	-0.14
4b	-0.015	0.917		
5a	-0.225	1.037		
5b	0.006	0.894		
6a	-0.163	1.021	5.4	-0.09
6b	-0.026	0.934		

Figure 86. Delta Wing, Indented Body M=0.95 Solution

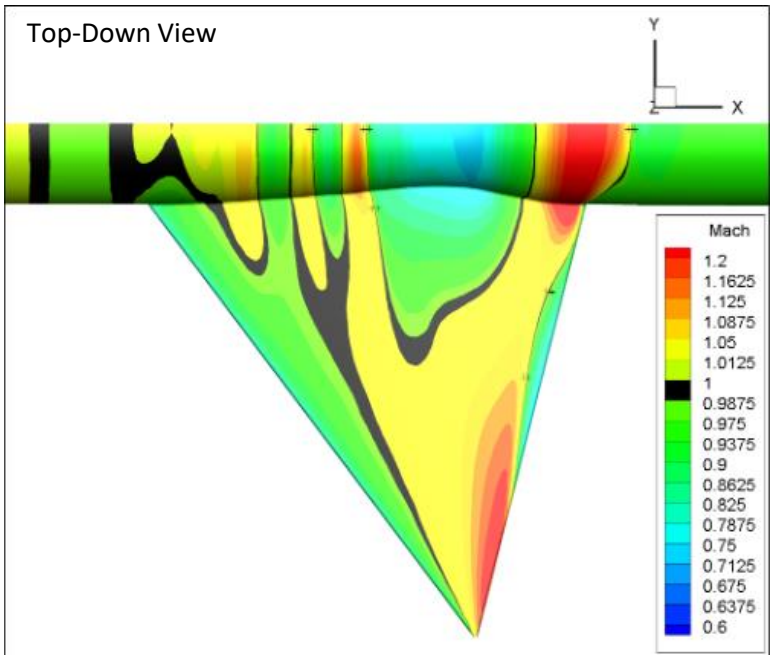

Probes	***CP***	**Mach #**	**Shock Angle (º)**	***CP****
1a	-0.116	1.028	Unknown	N/A
1b	-0.004	0.959		
2a	-0.172	1.049	Unknown	N/A
2b	0.019	0.933		

3a	-0.126	1.034	10.8	(-0.06)-(-0.07)
3b	0.035	0.935		
4a	-0.084	1.011	27.4	-0.2
4b	0.000	0.959		
5a	-0.155	1.052	6.3	(-0.04)-(-0.06)
5b	0.028	0.937		
6a	-0.154	1.033	Unknown	N/A
6b	0.001	0.937		

Figure 87. Delta Wing, Indented Body M=0.98 Solution

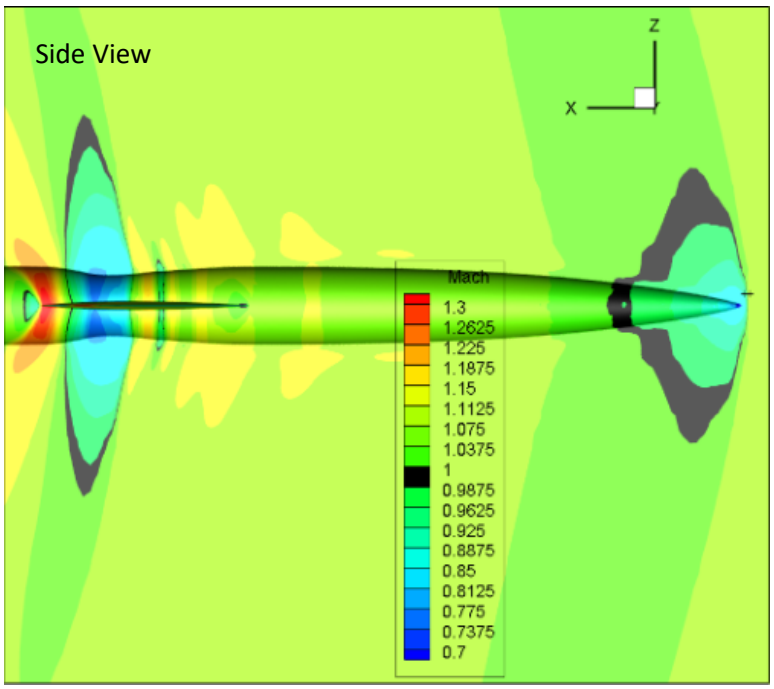

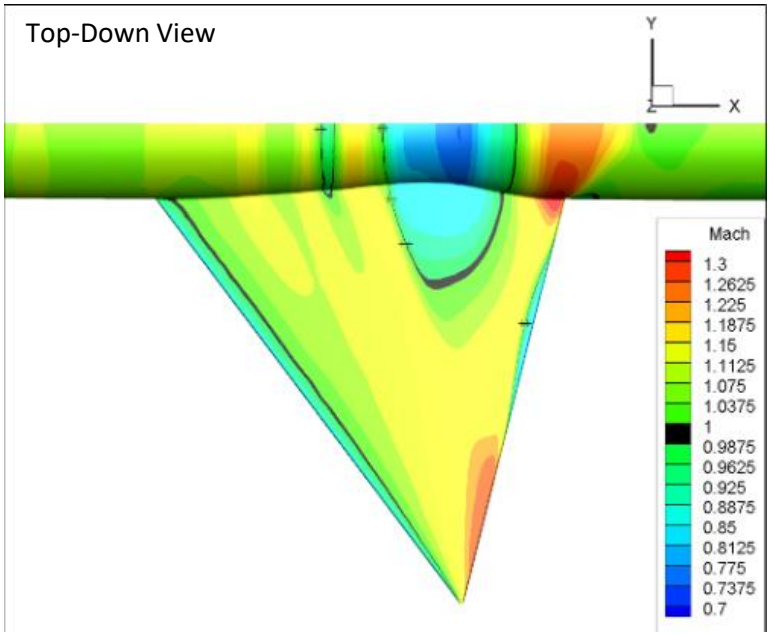

Probes	***CP***	**Mach #**	**Shock Angle (º)**	***CP****
1a (Flow)	0.001	1.049	6.7	N/A
1b (Flow)	0.146	0.957		
2a	0.008	1.030	30	-0.13
2b	0.119	0.967		
3a	0.013	1.021	12.8	N/A
3b	0.115	0.951		
4a	-0.011	1.034	19	N/A
4b	0.135	0.939		
5a	-0.005	1.037		
5b	0.109	0.964		
6a	-0.029	1.048	12.9	N/A
6b	0.153	0.923		

Figure 88. Delta Wing, Indented M=1.05 Solution

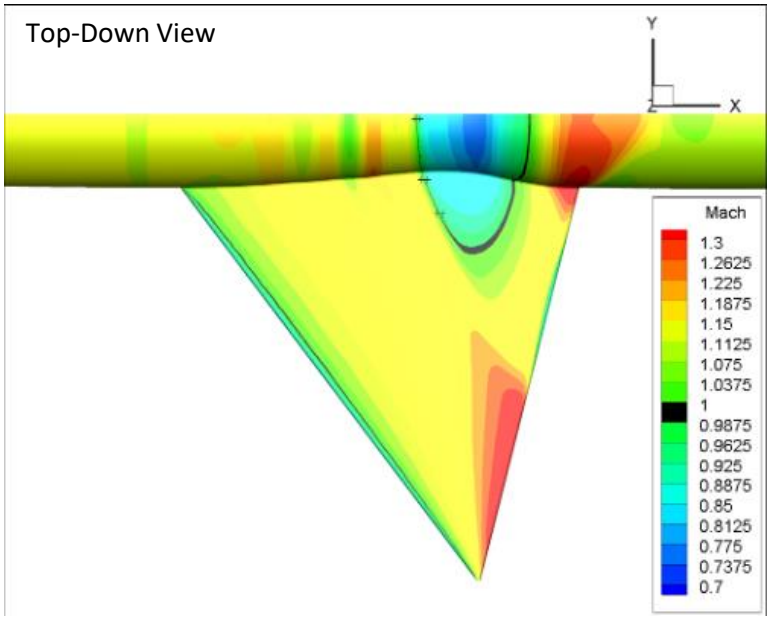

Probes	*CP*	Mach #	Shock Angle (º)	*CP**
1a	0.068	1.029	Unknown	N/A
1b	0.220	0.929		
2a	0.055	1.033	25.3	0
2b	0.188	0.942		
3a	0.086	1.021		
3b	0.175	0.962		

Figure 89. Delta Wing, Indented M=1.1 Solution

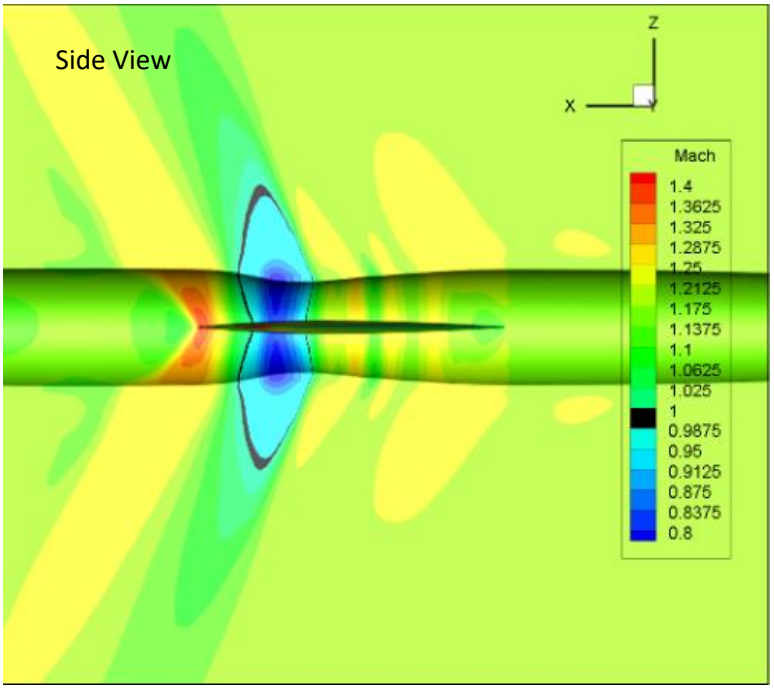

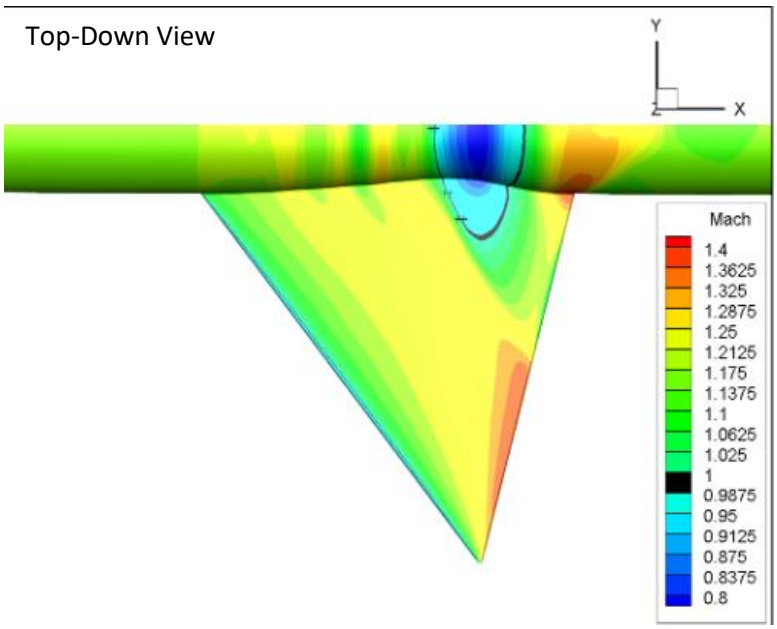

Probes	*CP*	Mach #	Shock Angle (º)	*CP**
1a	0.150	1.030	21.6	N/A
1b	0.246	0.966		
2a	0.136	1.024	28.2	N/A
2b	0.224	0.962		

3a	0.156	1.016		
3b	0.228	0.968		

Figure 90. Delta Wing, Indented M=1.15 Solution

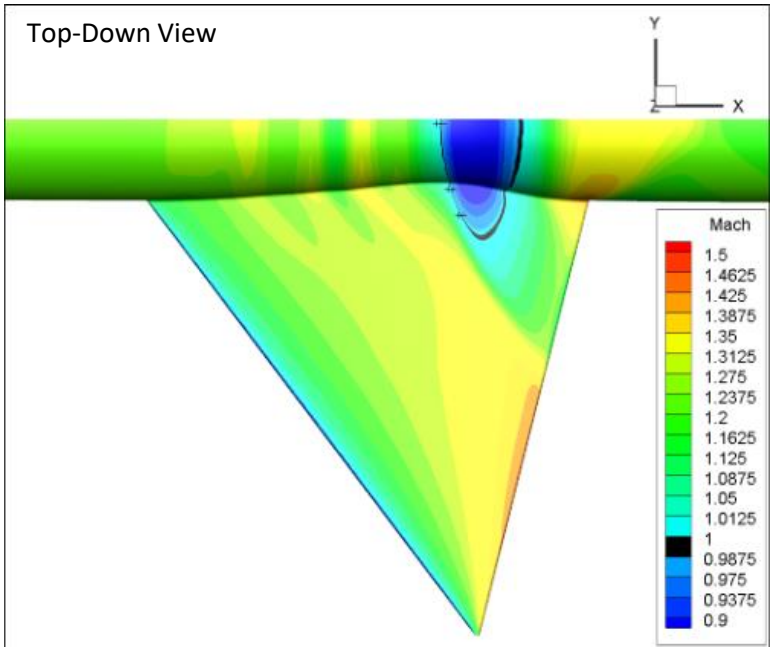

Probes	***CP***	**Mach #**	**Shock Angle (º)**	***CP****
1a	0.227	1.019	Unknown	N/A
1b	0.306	0.963		
2a	0.196	1.022	24.9	N/A
2b	0.281	0.961		
3a	0.197	1.026		
3b	0.281	0.968		

Figure 91. Delta Wing, Indented M=1.2 Solution

In the delta wing indented solutions, the situation is very similar to the indented body unswept case in that a shock first occurs in the Mach 0.88 solution and has a very

similar shape. However, instead of forward of the indentation, the shock now begins aft of it. In the Mach 0.95 solution, another similarity is seen with the three bands of supersonic flow forward of the indentation. Something similar is seen developing in the unswept case behind the indentation. As the Mach number is increased multiple shocks appear on this body. In the Mach 0.98 solution, three different shocks are seen on the body and two on the wing with several different regions of supersonic flow all over the wing. Like the unswept case again, as the Mach number is increased, all other shocks seem to disappear with the only shock remaining being one forward of the indentation. However, given the drops in Mach number over the shocks at the Mach 1.2 solutions for both the delta indented and unswept indented cases, it appears that the delta indented geometry produces a weaker shock forward of the indentation. The Mach number drop over the shock for the delta case is approximately 0.061 whereas the unswept case is approximately 0.097. This would be an interesting point of conversation in comparison to the drag reduction due to body indentations as shown in Chapter 5.

Probe 4 and 5 of the Mach 0.95 solution do seem to have a shock angle measurement that fits the Mach cone angle for the local Mach numbers measured. The Mach cone angle equation says that between a Mach number of 1.03 and 1.04 would yield an angle of 13.86 or 15.94 degrees, respectively. Probes 4 and 5 correspond to an angle of approximately 14.8 degrees. Once again, this is a single occurrence within this collection. For the critical pressure coefficient predictions the subsonic solutions are predicted fairly well, but they are not quite at the midpoint between the range of measured values. The supersonic solutions are again not able to be predicted.

g. Swept Wing, Cylindrical Body

In this section are the CFD solutions (some surface and some flow) for the Swept Wing, Cylindrical Body geometry. This section consists of Fig. (92)-Fig. (97) which include figures and the tabulated values of the probe data collected. Refer to Chapter 3, Part e. for instructions on how to read these.

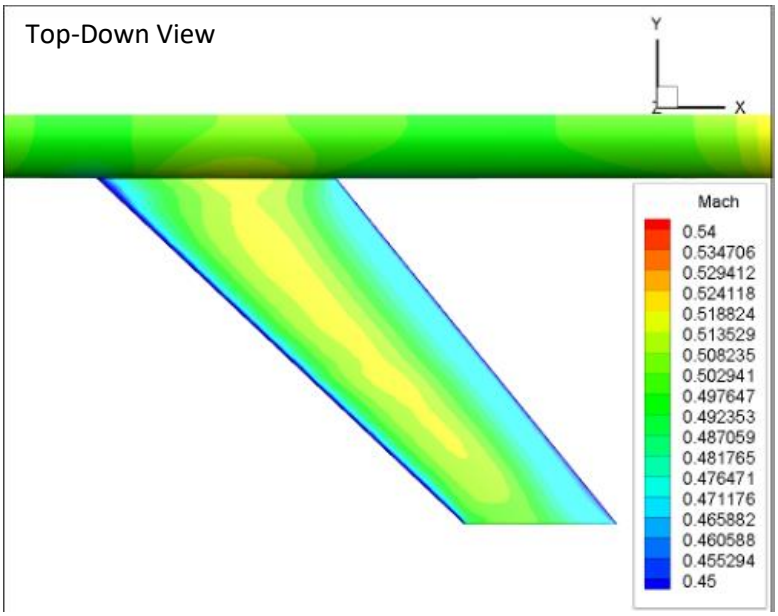

Figure 92. Swept Wing, Cylindrical Body M=0.5 Solution

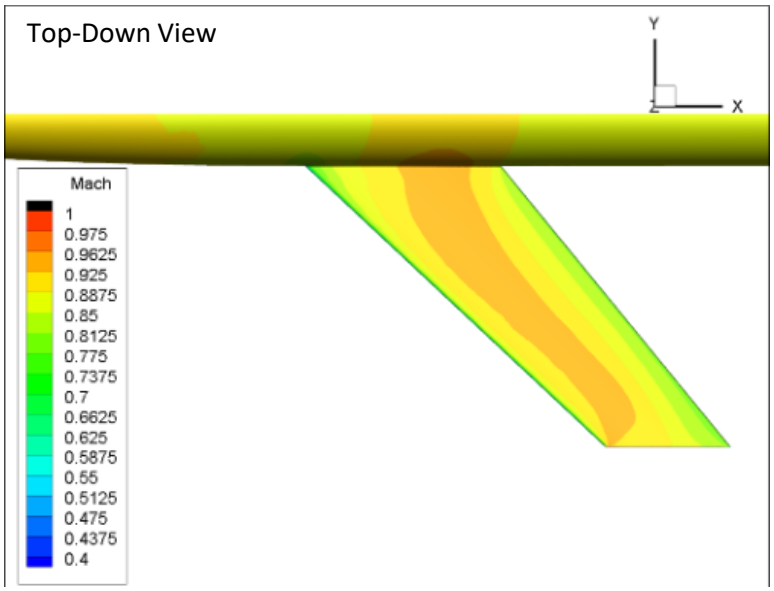

Figure 93. Swept Wing, Cylindrical Body M=0.88 Solution

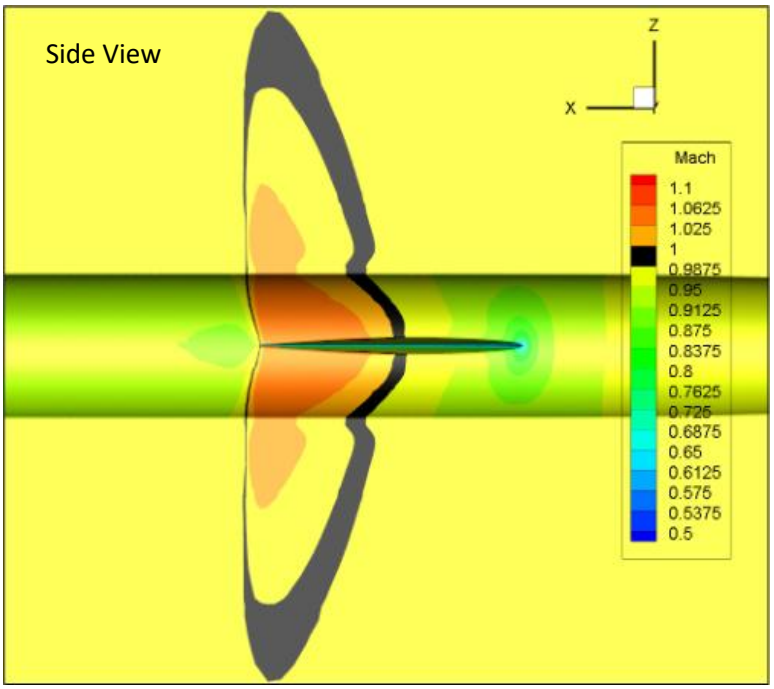

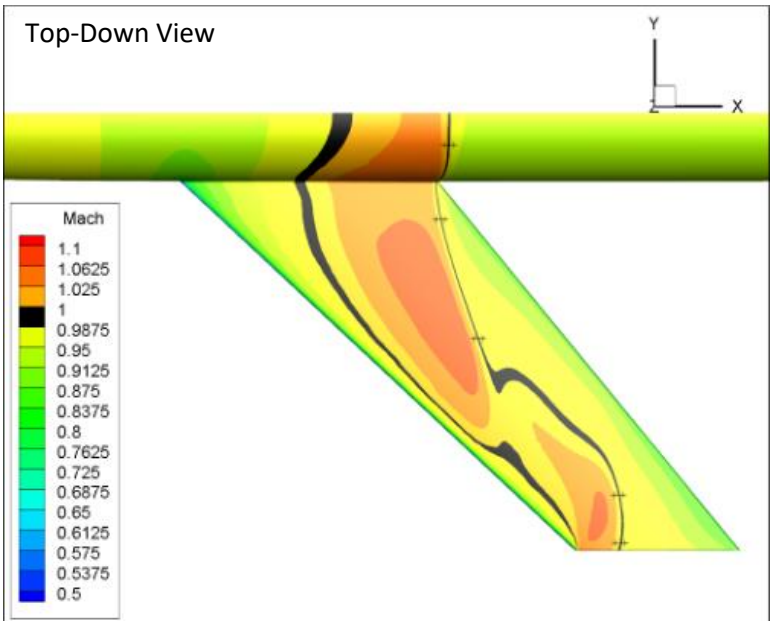

Probes	*CP*	Mach #	Shock Angle (º)	*CP**
1a	-0.127	1.013	1.9	-0.09
1b	-0.051	0.968		
2a	-0.183	1.022	16.8	(-0.14)-(-0.16)
2b	-0.081	0.960		
3a	-0.185	1.016		
3b	-0.111	0.972		
4a	-0.187	1.018	11.7	(-0.11)-(-0.13)
4b	-0.110	0.971		
5a	-0.181	1.016	6.8	(-0.09)-(-0.11)
5b	-0.109	0.976		

Figure 94. Swept Wing, Cylindrical Body M=0.95 Solution

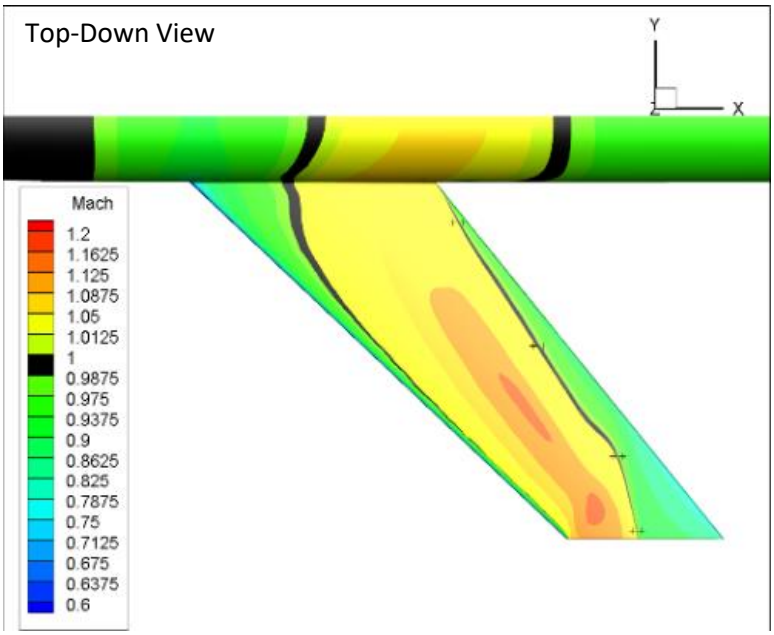

Probes	*CP*	Mach #	Shock Angle (º)	*CP**
1a	-0.135	1.027	32.8	-0.26
1b	-0.039	0.968		
2a	-0.107	1.006		
2b	-0.061	0.979		
3a	-0.122	1.011	15.2	-0.09
3b	-0.035	0.958		
4a	-0.167	1.040		
4b	0.004	0.933		

Figure 95. Swept Wing, Cylindrical Body M=0.98 Solution

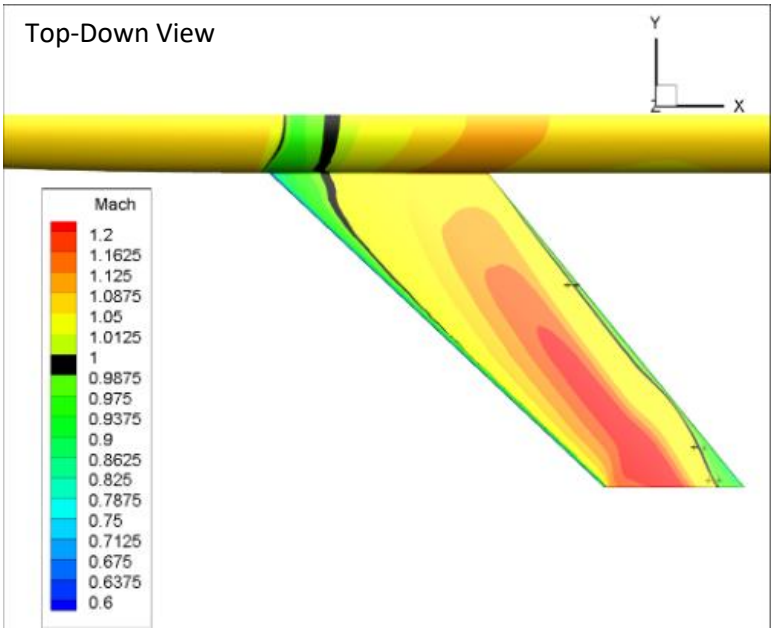

Probes	*CP*	Mach #	Shock Angle (º)	*CP**
1a	-0.003	1.016	37	-0.22
1b	0.054	0.975		
2a	-0.001	1.010	25.1	-0.07
2b	0.060	0.969		
3a	-0.010	1.017		
3b	0.066	0.968		

Figure 96. Swept Wing, Cylindrical Body M=1.05 Solution

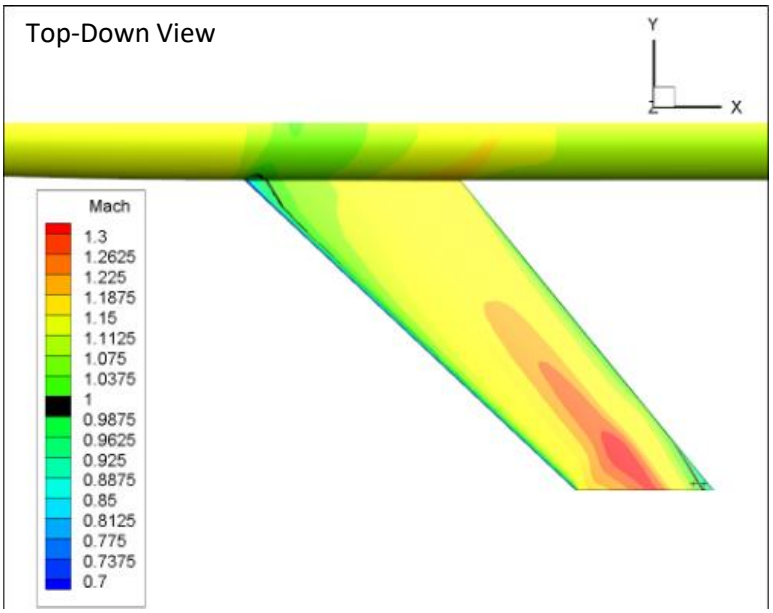

Probes	*CP*	Mach #	Shock Angle (º)	*CP**
1a	0.063	1.016	30	-0.13
1b	0.132	0.969		

Figure 97. Swept Wing, Cylindrical Body M=1.1 Solution

In this geometry, a shock first develops in the Mach 0.95 solution with one occurring on the body and appearing to spill onto the wing while another occurs at the wing-tip almost normal to the wing-tip edge. As the freestream Mach number is increased, the two wing shocks appear to merge, and the body shock disappears. As will be shown in the comparable body geometry, a bow shock forms at the nose of the body in the Mach 1.05 solution. Thus, for the Mach 0.98 solution, there are no body shocks at all. The shocks then progress further toward the trailing edge of the wing until the shocks are no longer visible.

The only case that appears to be relatively close at having the shock angle and local Mach number Mach cone angle coinciding is probe 4 of the Mach 0.98 solution. The Mach cone angle would be 15.94 degrees whereas the shock angle there is approximately 15.2 degrees. As for critical pressure coefficient predictions, the subsonic solution data appears to agree quite well with the exception of the probe data closer to the body on the wing. Given the thickness of the black region here and the relatively tame Mach number drop, this may not be a shock.

h. Swept Wing, Cylindrical Comparable Body

In this section are the CFD solutions (all flow) for the Swept Wing, Comparable Body geometry. This section consists of Fig. (98)-Fig. (105) which include figures and the tabulated values of the probe data collected. Refer to Chapter 3, Part e. for instructions on how to read these.

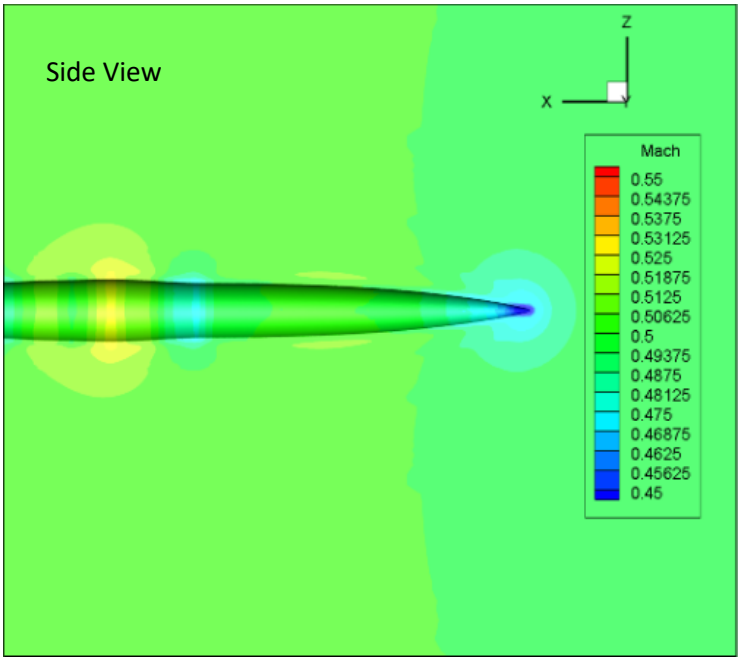

Figure 98. Swept Wing, Cylindrical Comparable Body M=0.5 Solution

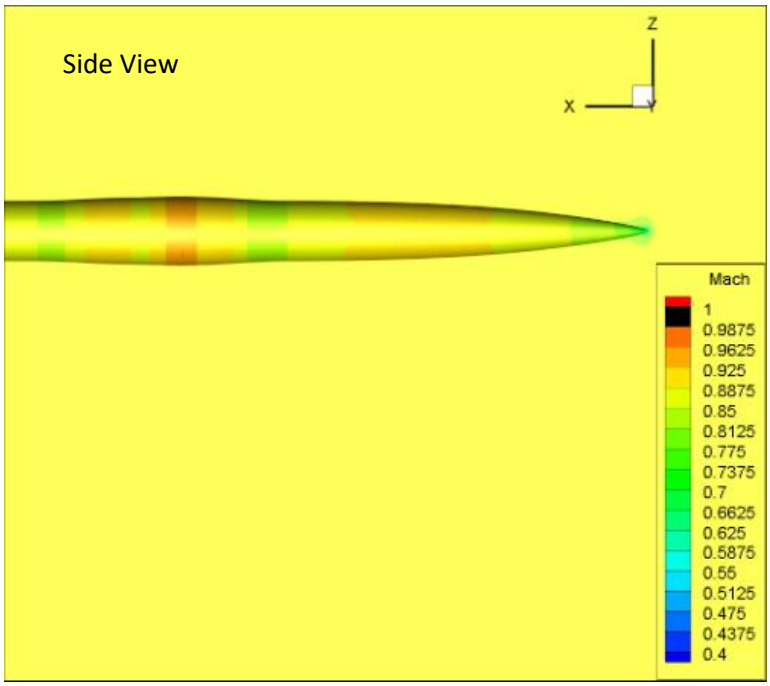

Figure 99. Swept Wing, Cylindrical Comparable Body M=0.88 Solution

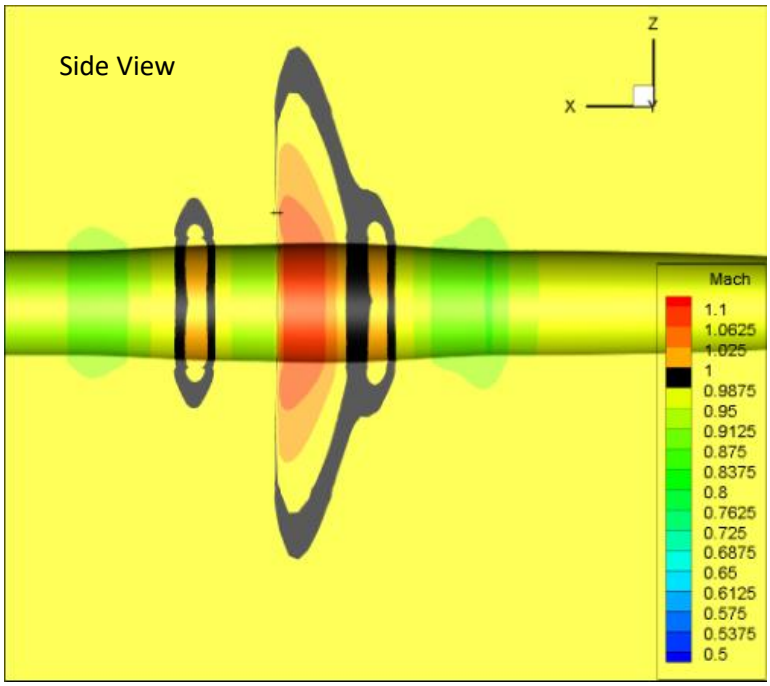

Probes	***CP***	**Mach #**	**Shock Angle (º)**	***CP****
1a	-0.200	1.064	6.6	

1b	-0.003	0.951		(-0.09)-(-0.11)
2a	-0.166	1.033		
2b	-0.053	0.965		

Figure 100. Swept Wing, Cylindrical Comparable Body M=0.95 Solution

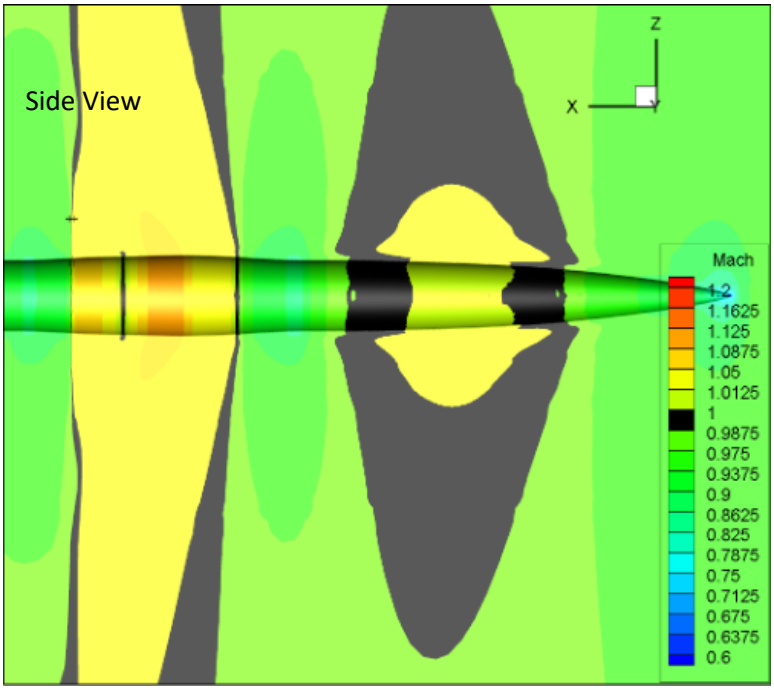

Probes	***CP***	**Mach #**	**Shock Angle (º)**	***CP****
1a	-0.083	1.028	2.3	(-0.03)-(-0.04)
1b	0.005	0.975		
2a	-0.107	1.031		
2b	0.011	0.959		

Figure 101. Swept Wing, Cylindrical Comparable Body M=0.98 Solution

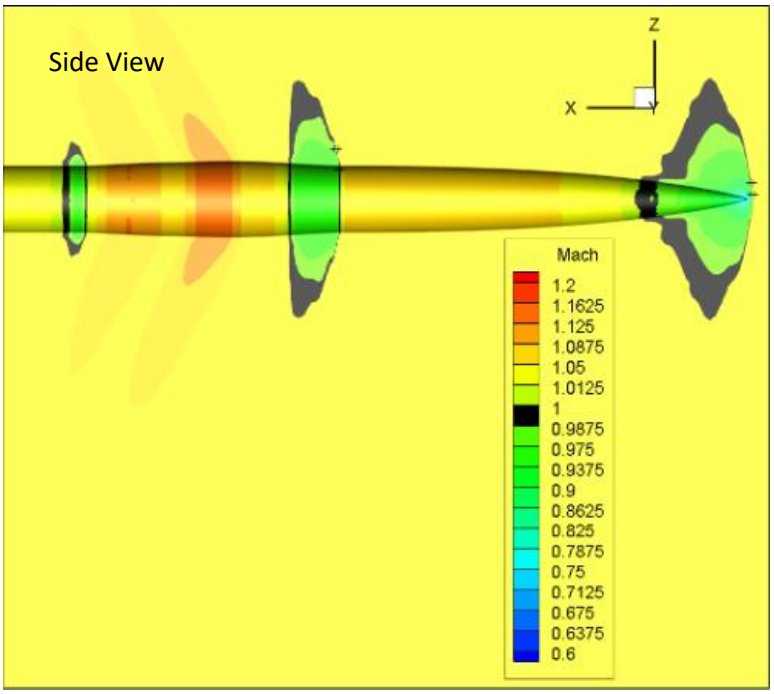

Probes	*CP*	Mach #	Shock Angle (º)	*CP**
1a	0.008	1.044	17.8	N/A
1b	0.115	0.977		
2a	0.025	1.026		
2b	0.115	0.970		
3a	0.013	1.041	9.7	N/A
3b	0.117	0.975		
4a	0.003	1.047		
4b	0.177	0.937		

Figure 102. Swept Wing, Cylindrical Comparable Body M=1.05 Solution

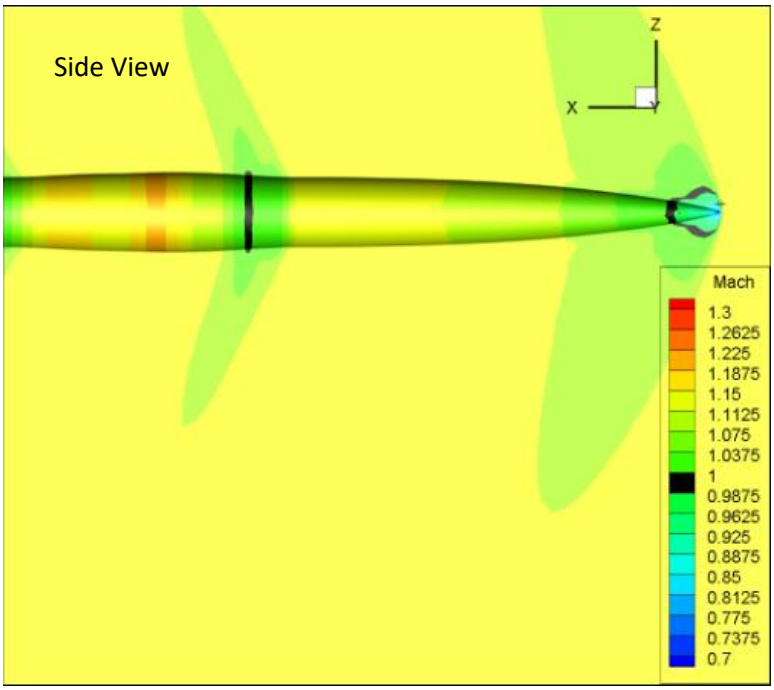

Probes	*CP*	Mach #	Shock Angle (º)	*CP**
1a	0.006	1.095	30	N/A
1b	0.187	0.974		

Figure 103. Swept Wing, Cylindrical Comparable Body M=1.1 Solution

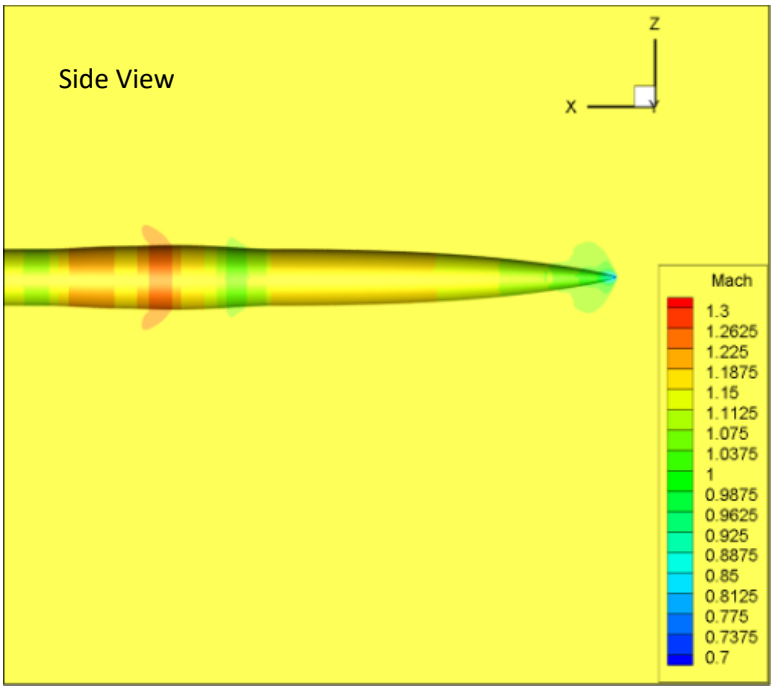

Figure 104. Swept Wing, Cylindrical Comparable Body M=1.15 Solution

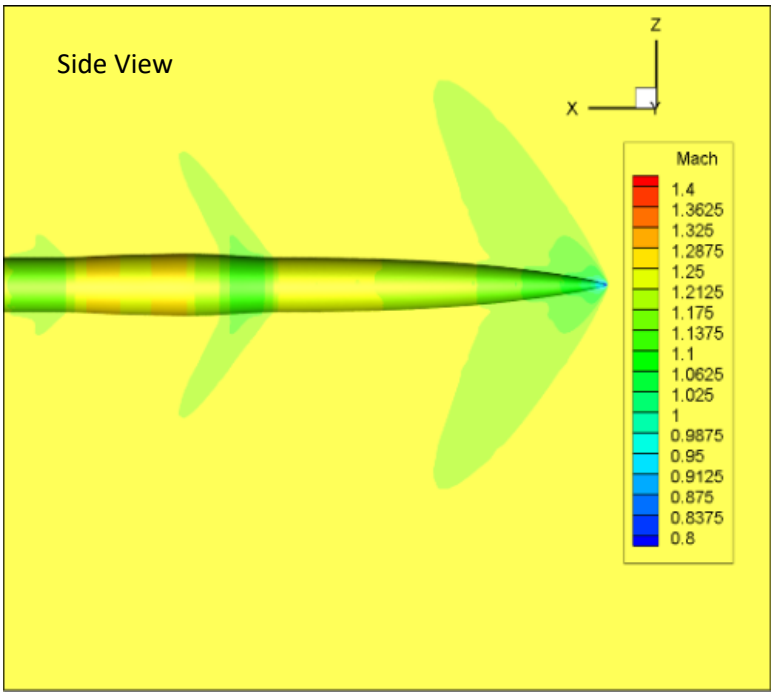

Figure 105. Swept Wing, Cylindrical Comparable Body M=1.2 Solution

This geometry behaves somewhat similarly to the unswept case in that at subsonic freestream conditions, a shock occurs aft of the point of maximum cross-sectional area which eventually moves forward of this point at supersonic conditions. However, this geometry does not appear to produce a shock at the Mach 0.88 conditions. The Mach 1.05 solution does also seem to show a region of supersonic flow aft of the maximum cross-sectional area similar to that of the delta comparable body case. As the Mach number is increased to supersonic, there also appears to be a bow shock that develops and is present in the base and indented body cases as well. Eventually, all shocks seem to disappear on the body.

No shock angles measured in these solutions appear to coincide with any predicted Mach cone angles. The subsonic solutions have their critical pressure coefficients quite well by Küchemann's critical pressure coefficient equation here. No predictions could be made for the supersonic cases.

i. Swept Wing, Indented Body

In this section are the CFD solutions (some surface and some flow) for the Swept Wing, Indented Body geometry. This section consists of Fig. (106)-Fig. (112) which include figures and the tabulated values of the probe data collected. Refer to Chapter 3, Part e. for instructions on how to read these.

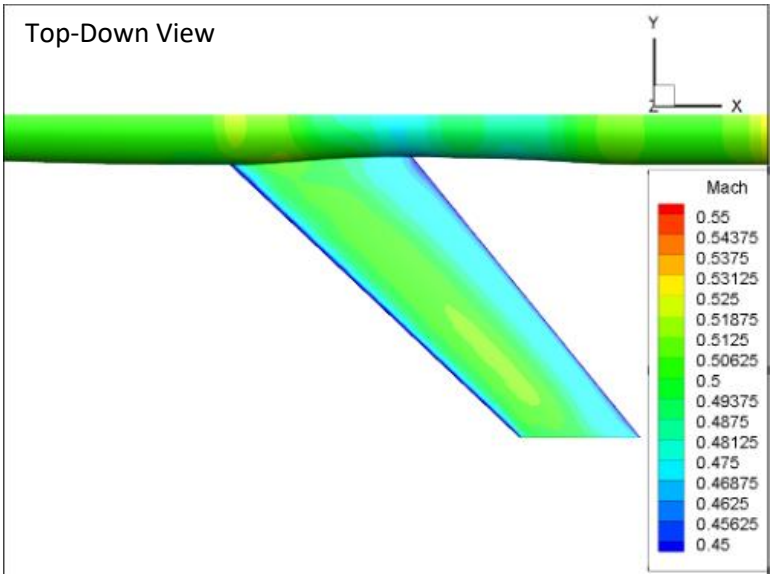

Figure 106. Swept Wing, Indented Body M=0.5 Solution

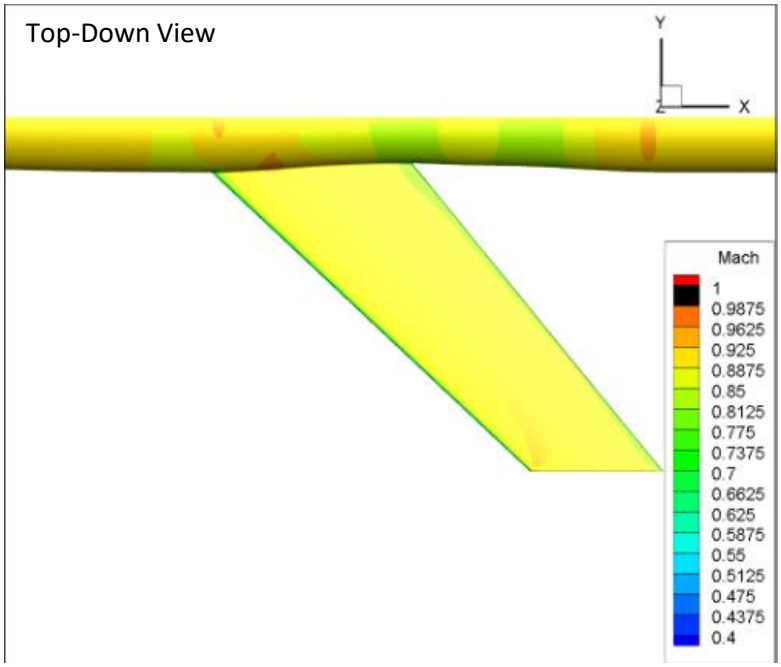

Figure 107. Swept Wing, Indented Body M=0.88 Solution

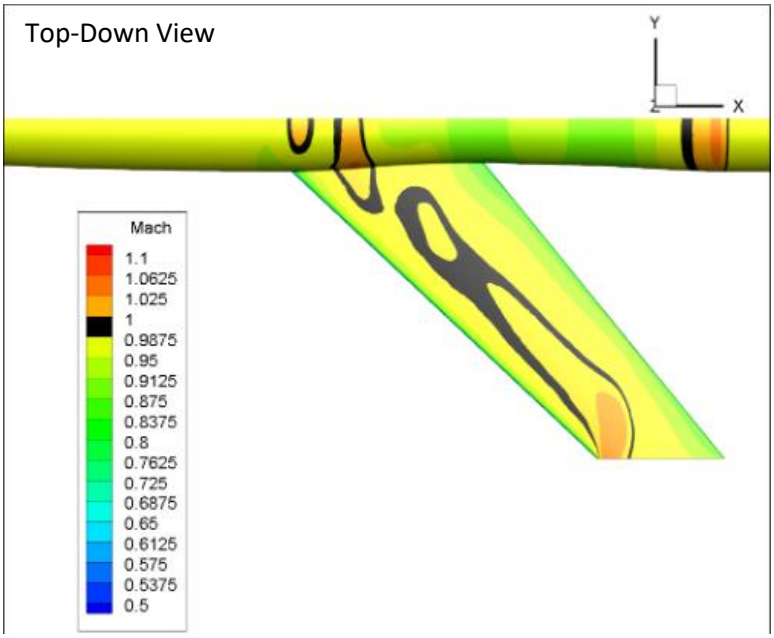

Figure 108. Swept Wing, Indented Body M=0.95 Solution

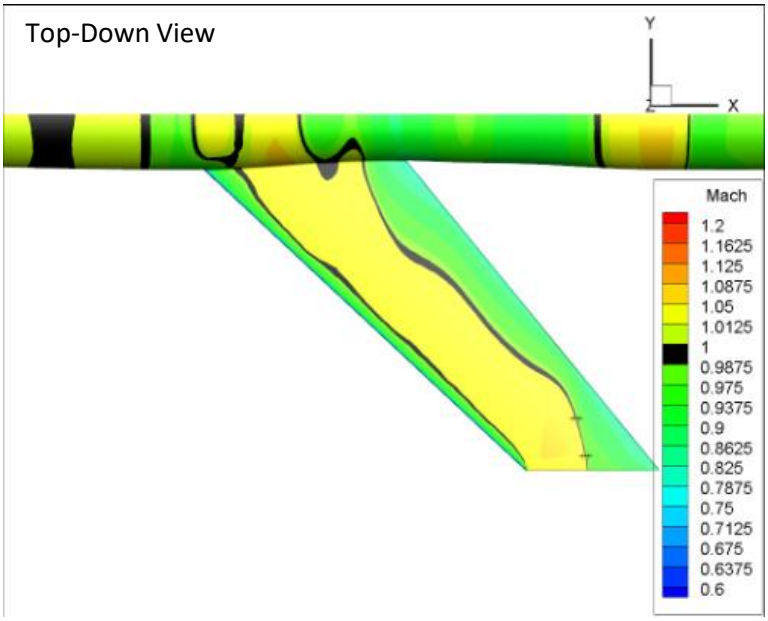

Probes	***CP***	**Mach #**	**Shock Angle (º)**	***CP****
1a	-0.116	1.010	14.7	(-0.07)-(-0.09)
1b	-0.049	0.969		
2a	-0.129	1.016		

2b	-0.047	0.966		

Figure 109. Swept Wing, Indented Body M=0.98 Solution

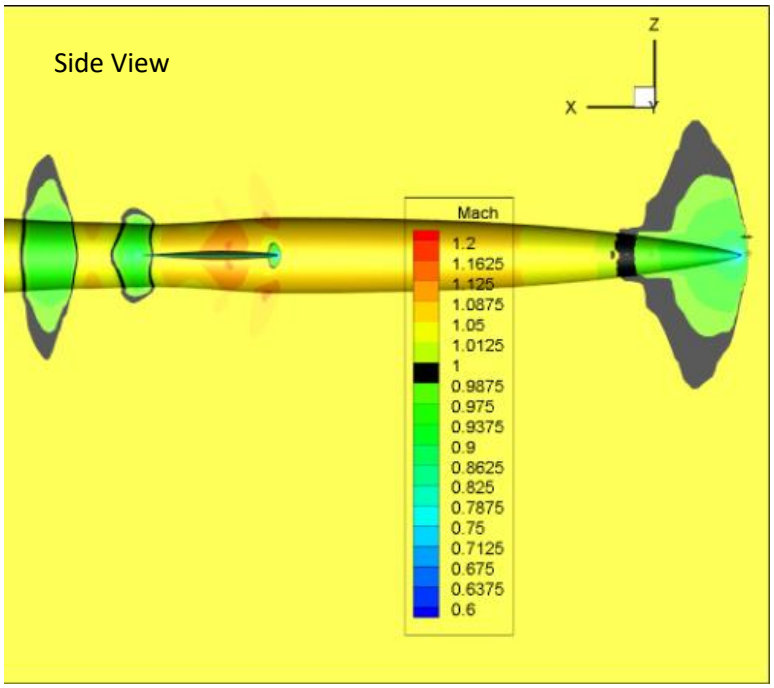

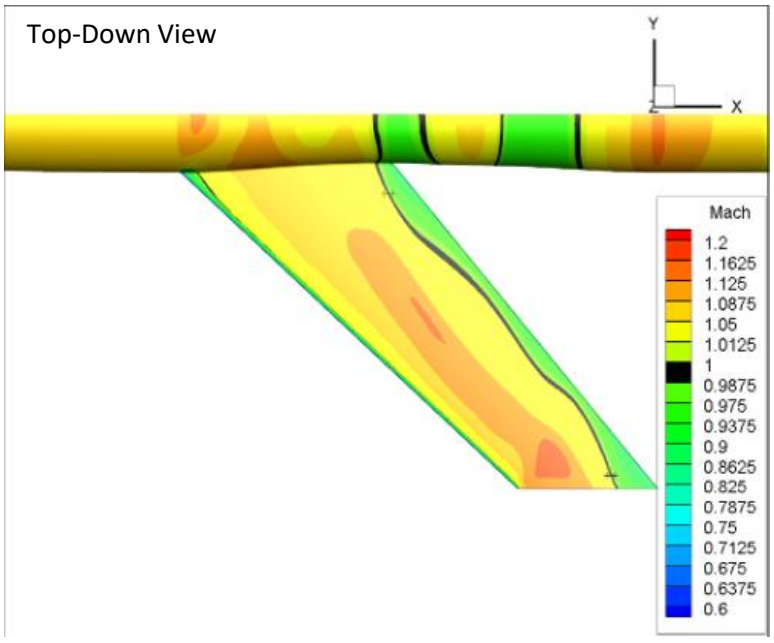

Probes	*CP*	Mach #	Shock Angle (º)	*CP**
1a (Flow)	0.003	1.047	12.5	N/A
1b (Flow)	0.136	0.963		
2a (Flow)	0.001	1.049		
2b (Flow)	0.108	0.980		
3a	-0.005	1.014	25.9	(-0.07)-(-0.10)
3b	0.053	0.976		
4a	-0.002	1.010	21.9	(-0.02)-(-0.04)
4b	0.051	0.976		

Figure 110. Swept Wing, Indented Body M=1.05 Solution

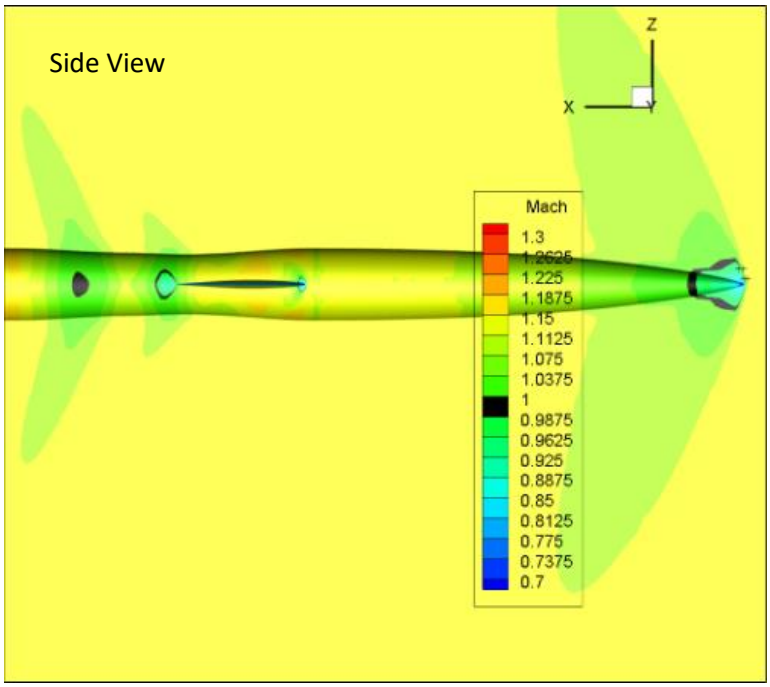

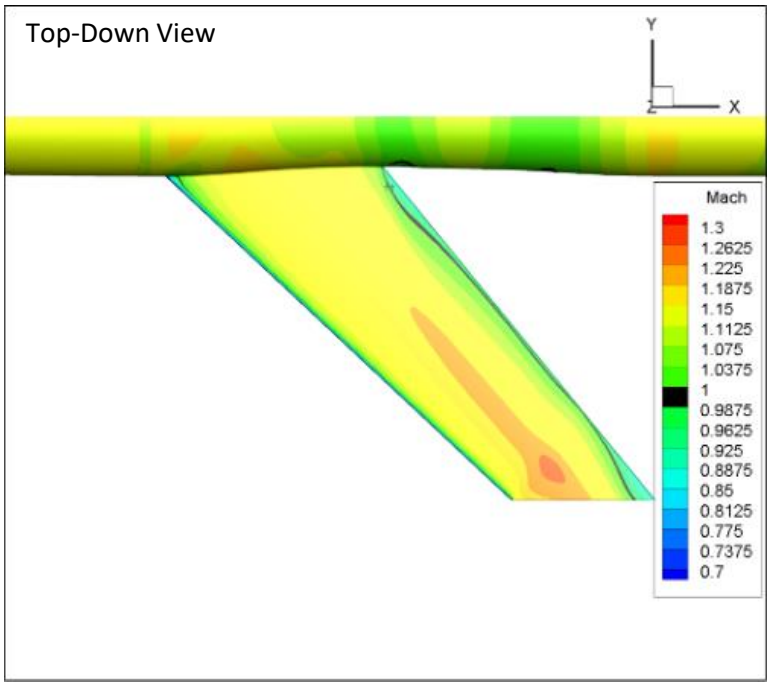

Probes	*CP*	Mach #	Shock Angle (º)	*CP**
1a (Flow)	0.029	1.080	20.4	N/A
1b (Flow)	0.187	0.975		
2a (Flow)	0.002	1.098		
2b (Flow)	0.125	1.011		
3a	0.071	1.010	19	N/A
3b	0.127	0.971		

Figure 111. Swept Wing, Indented Body M=1.1 Solution

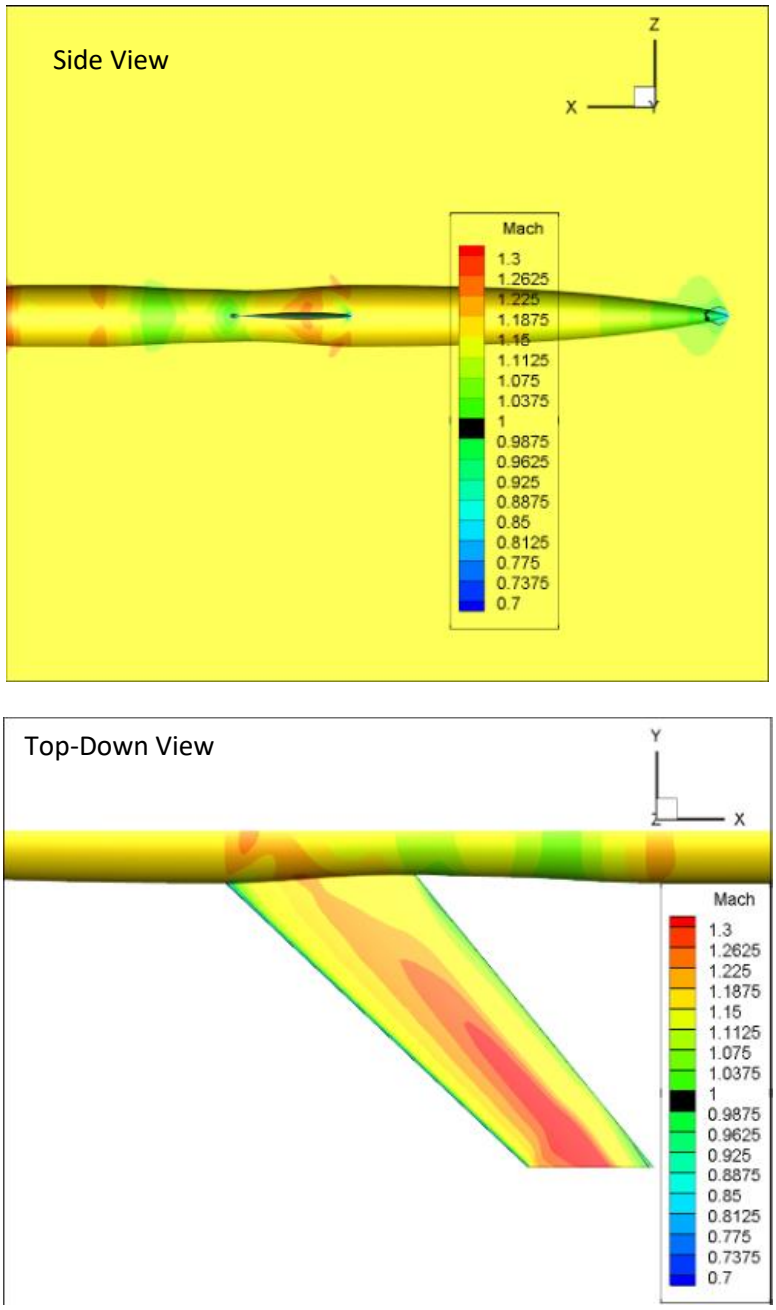

Figure 112. Swept Wing, Indented Body M=1.15 Solution

This geometry appears to be one of the only cases of simplifying the flow by indenting the body. Rather than developing shocks on the body and across the wing at the Mach 0.95 solution, this geometry appears to only develop some points of supersonic

flow on the wing. Even at the Mach 0.98 solution, the only shock developed is at the wing-tip, in a similar manner to the base body case. As the freestream Mach number increases, some relatively unclear shocks develop along the wing and eventually disappear. As shown in the comparable body cases, however, a bow shock develops at the Mach 1.05 case; this is unsurprising at this point. So, it is shown here that the number of and intensity of shocks developed is actually reduced by indenting the body.

Once again, expected Mach cone angles do not coincide with measured shock angles. For the only subsonic solution with shocks present, the critical pressure coefficients are predicted very well as is demonstrated in the Mach 0.98 solution probe data. The supersonic predictions once again do not work.

j. Swept Wing, Curved Body

In this section are the CFD solutions (some surface and some flow) for the Swept Wing, Curved Body geometry. This section consists of Fig. (113)-Fig. (118) which include figures and the tabulated values of the probe data collected. Refer to Chapter 3, Part e. for instructions on how to read these.

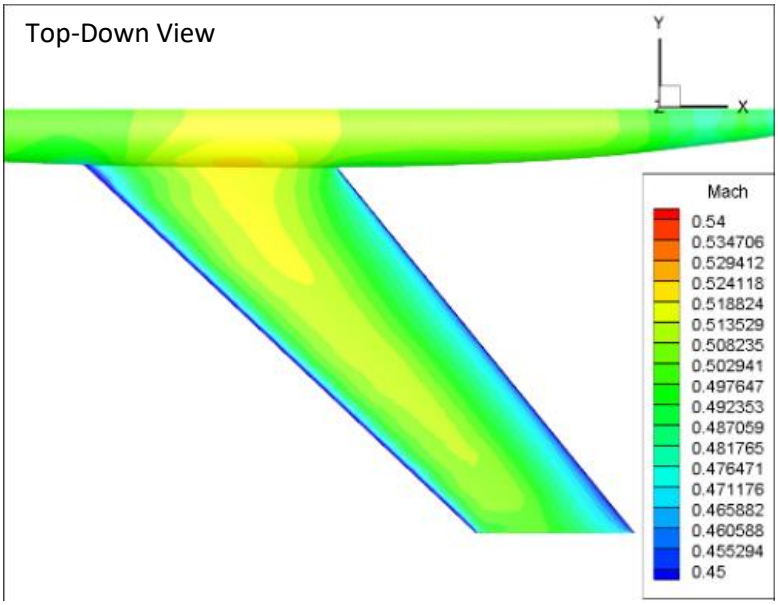

Figure 113. Swept Wing, Curved Body M=0.5 Solution

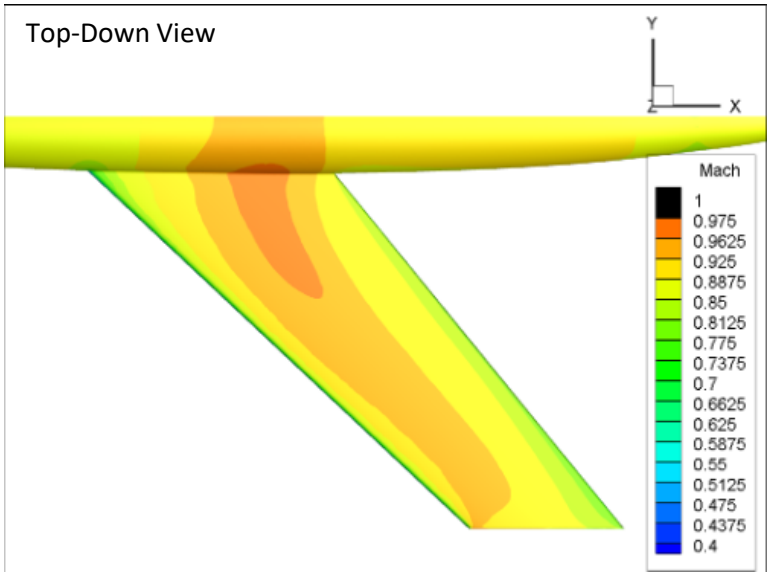

Figure 114. Swept Wing, Curved Body M=0.88 Solution

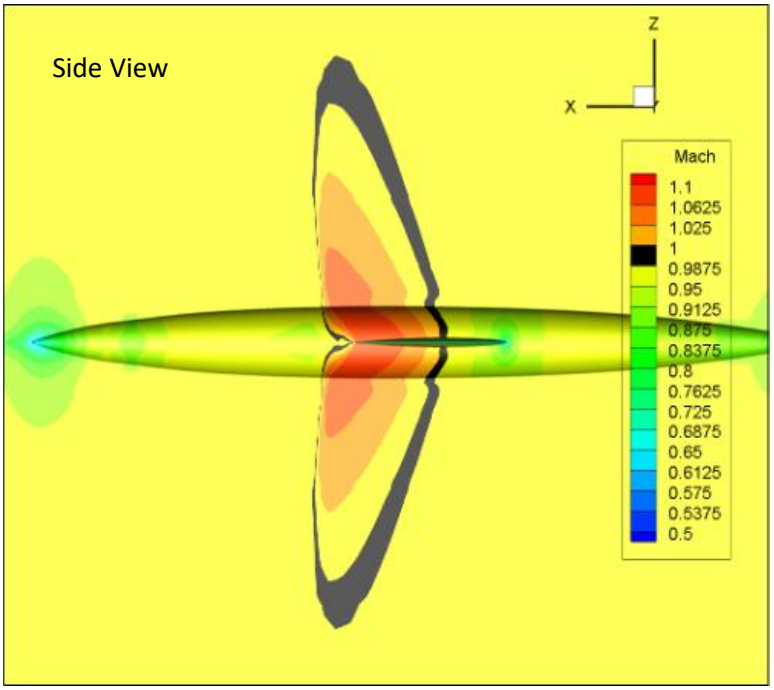

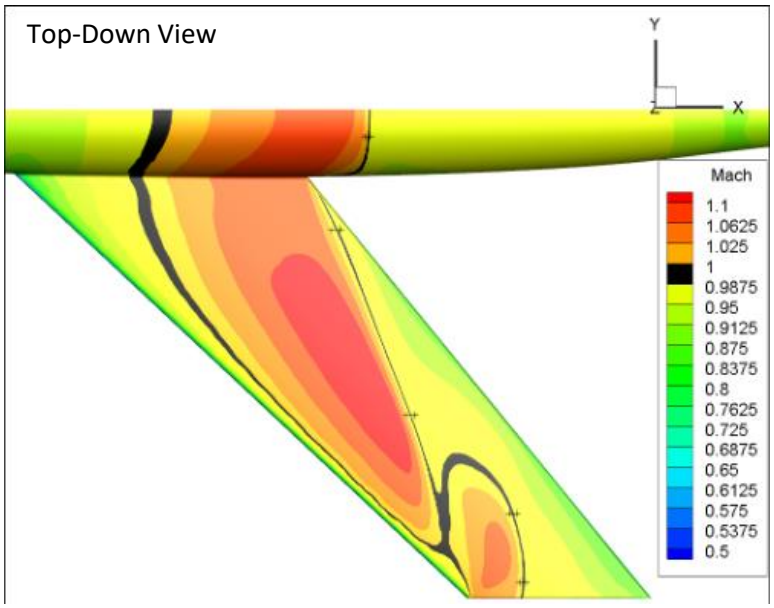

Probes	***CP***	**Mach #**	**Shock Angle (º)**	***CP****
1a	-0.130	1.012	4.2	-0.09
1b	-0.067	0.976		
2a	-0.175	1.017	21.7	(-0.18)-(-0.20)
2b	-0.105	0.974		

3a	-0.208	1.026		
3b	-0.102	0.965		
4a	-0.171	1.006	10.4	-0.11
4b	-0.110	0.969		
5a	-0.172	1.009		
5b	-0.118	0.977		

Figure 115. Swept Wing, Curved Body M=0.95 Solution

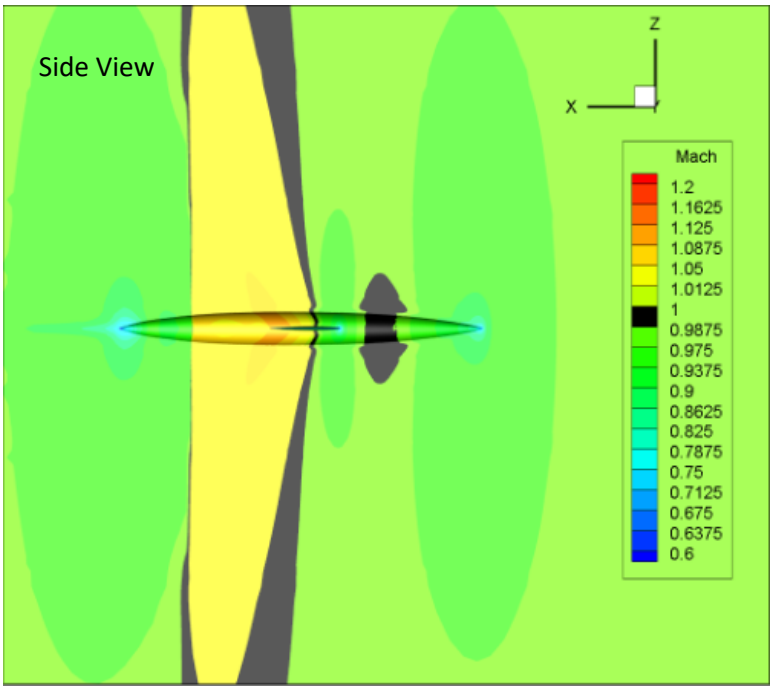

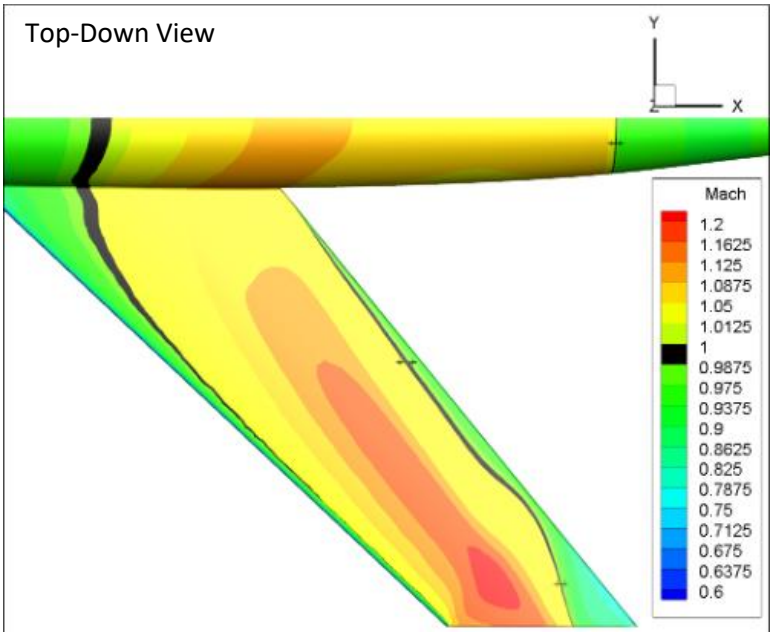

Probes	***CP***	**Mach #**	**Shock Angle (º)**	***CP****
1a	-0.097	1.022	~0	-0.03
1b	0.005	0.961		
2a	-0.110	1.009	35.6	-0.29
2b	-0.056	0.976		
3a	-0.129	1.015	16.7	(-0.09)-(-0.11)
3b	-0.044	0.963		

Figure 116. Swept Wing, Curved Body M=0.98 Solution

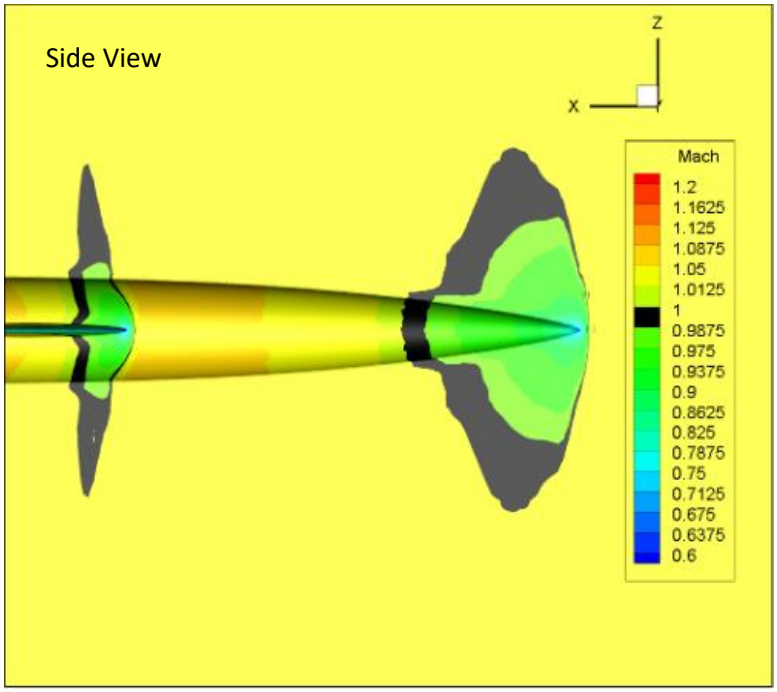

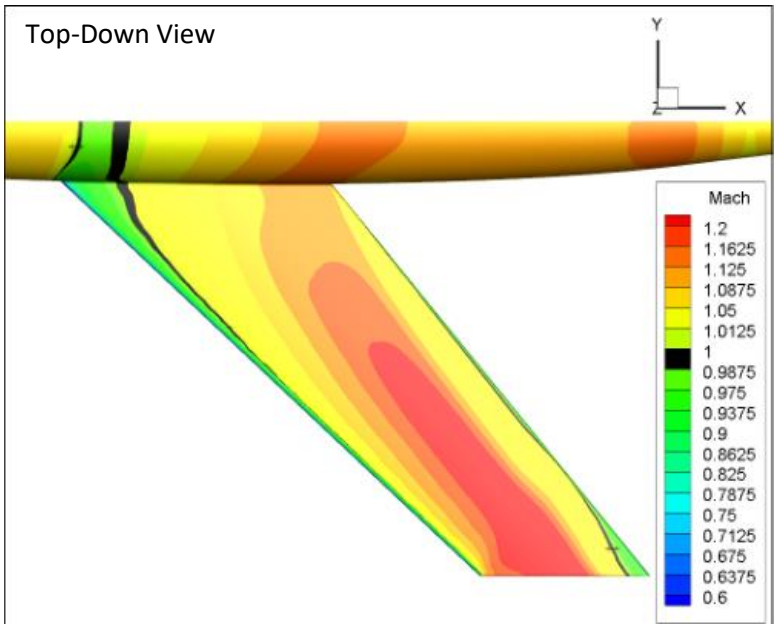

Probes	***CP***	**Mach #**	**Shock Angle (º)**	***CP****
1a (Flow)	0.000	1.049	9	N/A
1b (Flow)	0.153	0.951		
2a (Flow)	0.013	1.041		

2b (Flow)	0.130	0.967		
3a	0.040	1.011	14.1	N/A
3b	0.081	0.985		
4a	0.006	1.004	27.7	-0.10
4b	0.046	0.977		

Figure 117. Swept Wing, Curved Body M=1.05 Solution

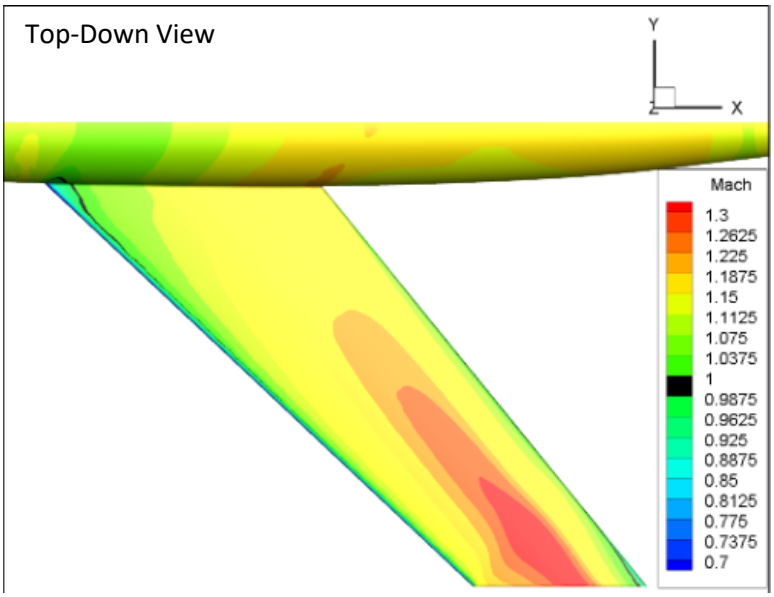

Figure 118. Swept Wing, Curved Body M=1.1 Solution

The swept wing, curved body case is interesting in that it develops shocks in a similar manner to the cylindrical body case. The patterns are almost all the same except that the body shock starts farther back from the wing and the wing shocks are closer to one another. However, at the Mach 0.98 solution, another body shock is seen toward the end of the body. As the Mach number is increased, the shock on the wing eventually disappears. The curved body appears to develop a bow shock at the nose at the Mach 1.05

solution as well. Other than these things, not much else is different between the cylindrical body and curved body cases.

No shock angles measured coincide with any expected Mach cone angles here. The subsonic solutions have the *CP** predictions fall in range of the data collected only for the Mach 0.98 solution and not very fitted to the center of the ranges. This is the first occurrence of the predictions not fitting the data very well.

k. Swept Wing, Curved Comparable Body

In this section are the CFD solutions (some surface and some flow) for the Swept Wing, Curved Comparable Body geometry. This section consists of Fig. (119)-Fig. (126) which include figures and the tabulated values of the probe data collected. Refer to Chapter 3, Part e. for instructions on how to read these.

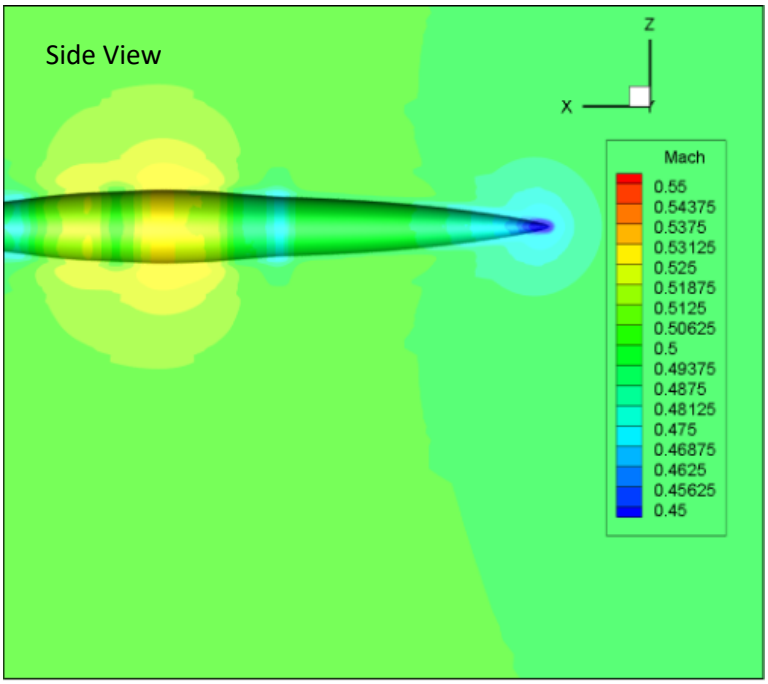

Figure 119. Swept Wing, Curved Comparable Body M=0.5 Solution

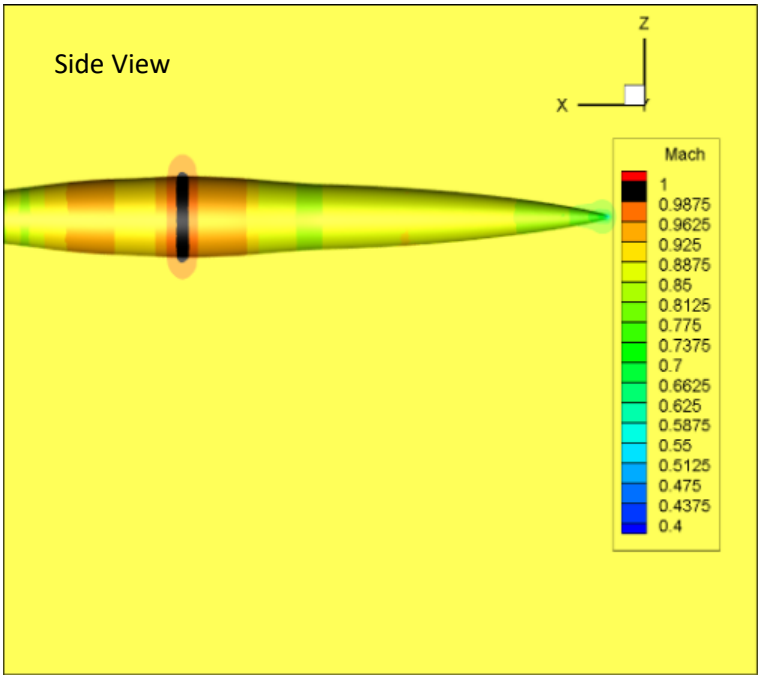

Figure 120. Swept Wing, Curved Comparable Body M=0.88 Solution

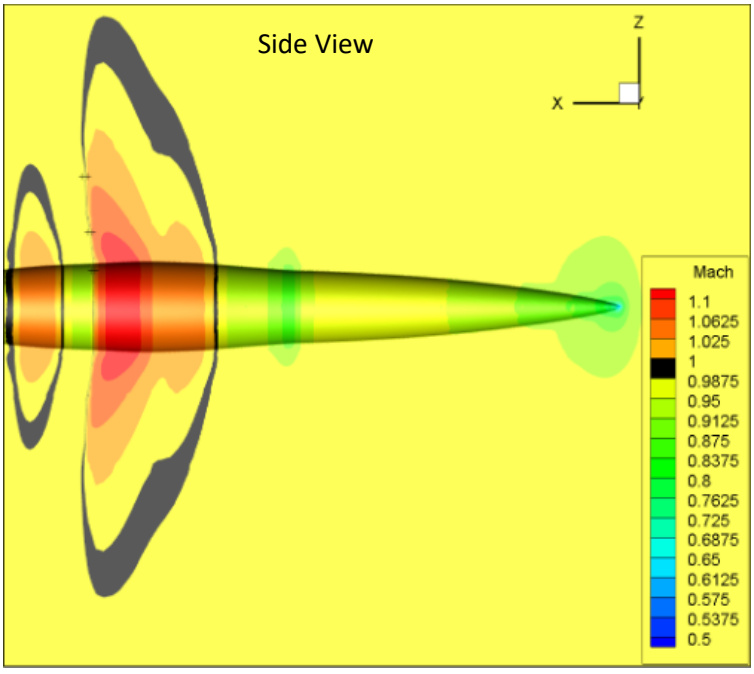

Probes	***CP***	**Mach #**	**Shock Angle (º)**	***CP****
1a	-0.151	1.037	6.6	

1b	-0.034	0.969		(-0.09)-(-0.11)
2a	-0.207	1.069		
2b	-0.006	0.952		
3a	-0.156	1.027		
3b	-0.044	0.961		

Figure 121. Swept Wing, Curved Comparable Body M=0.95 Solution

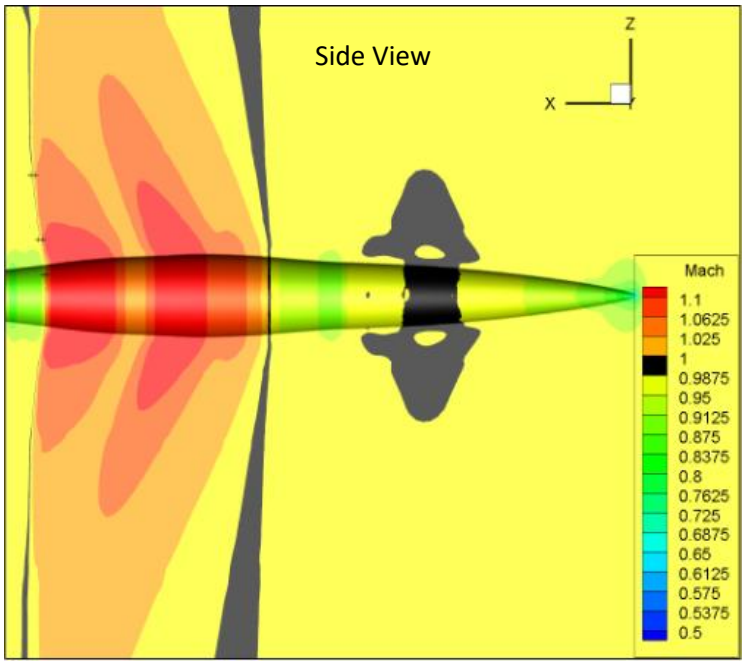

Probes	***CP***	**Mach #**	**Shock Angle (º)**	***CP****
1a	-0.123	1.053	9.2	(-0.09)-(-0.11)
1b	0.044	0.953		
2a	-0.178	1.086		
2b	0.079	0.932		
3a	-0.113	1.031		
3b	0.009	0.953		

Figure 122. Swept Wing, Curved Comparable Body M=0.98 Solution

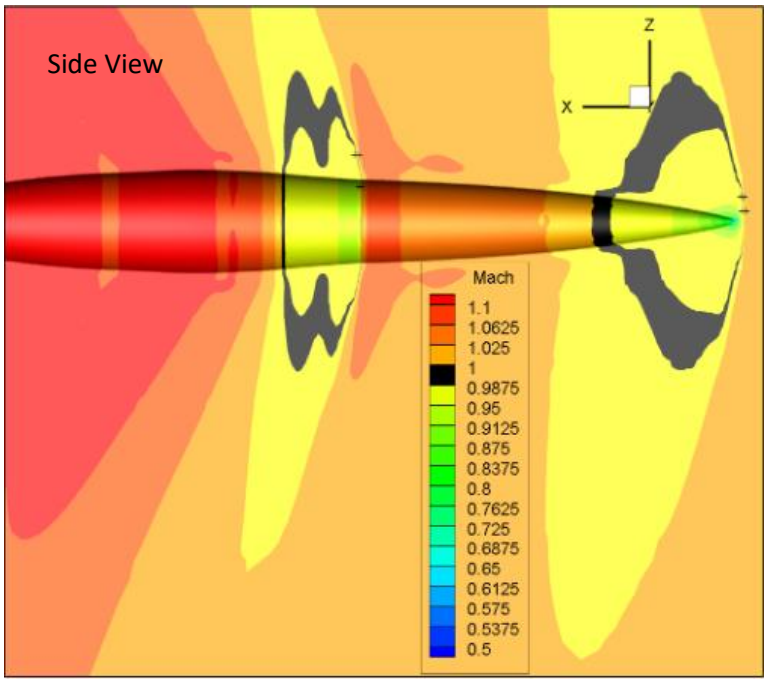

Probes	*CP*	Mach #	Shock Angle (º)	*CP**
1a	0.000	1.049	11.8	N/A
1b	0.120	0.974		
2a	0.004	1.035		
2b	0.102	0.974		
3a	0.009	1.043	7.6	N/A
3b	0.094	0.989		
4a	0.002	1.048		
4b	0.112	0.978		

Figure 123. Swept Wing, Curved Comparable Body M=1.05 Solution

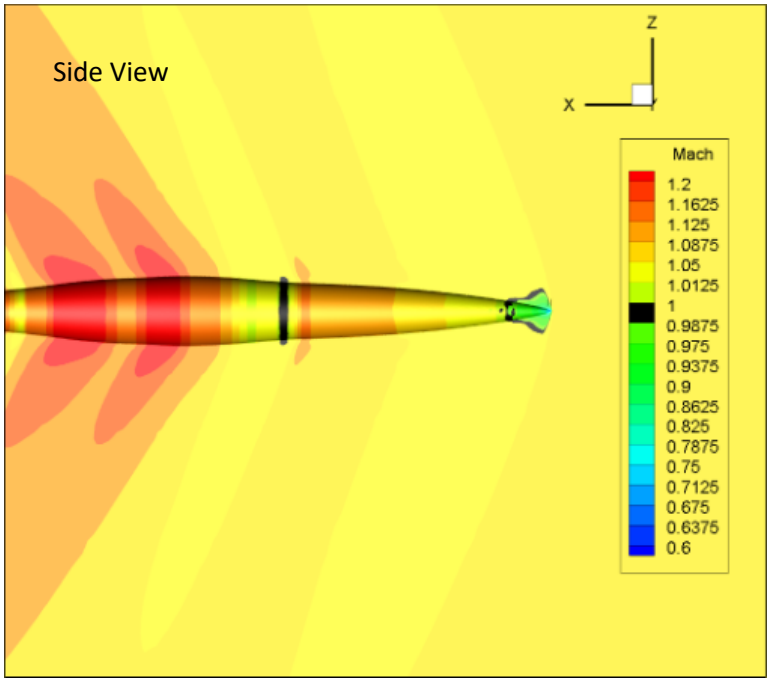

Probes	*CP*	Mach #	Shock Angle (º)	*CP**
1a	0.026	1.081	19.6	N/A
1b	0.218	0.954		

Figure 124. Swept Wing, Curved Comparable Body M=1.1 Solution

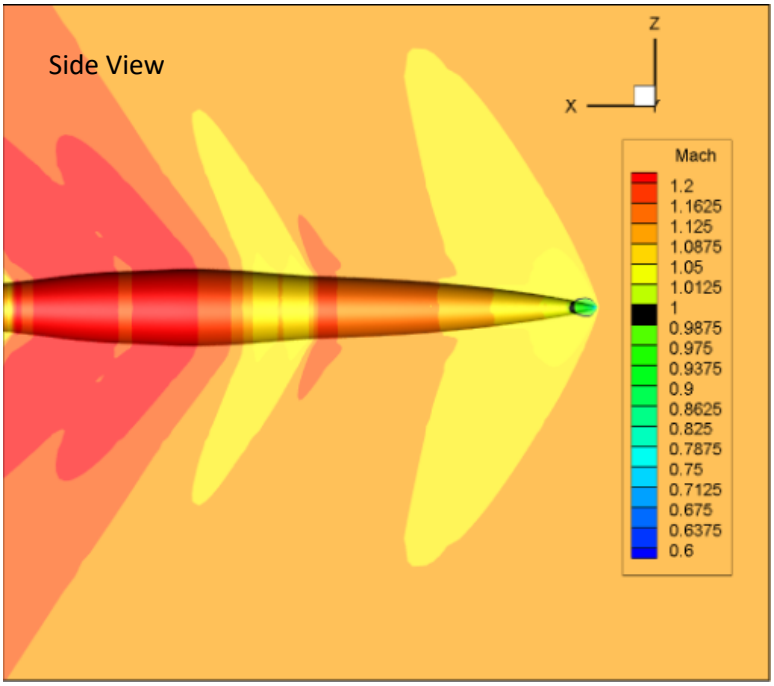

Figure 125. Swept Wing, Curved Comparable Body M=1.15 Solution

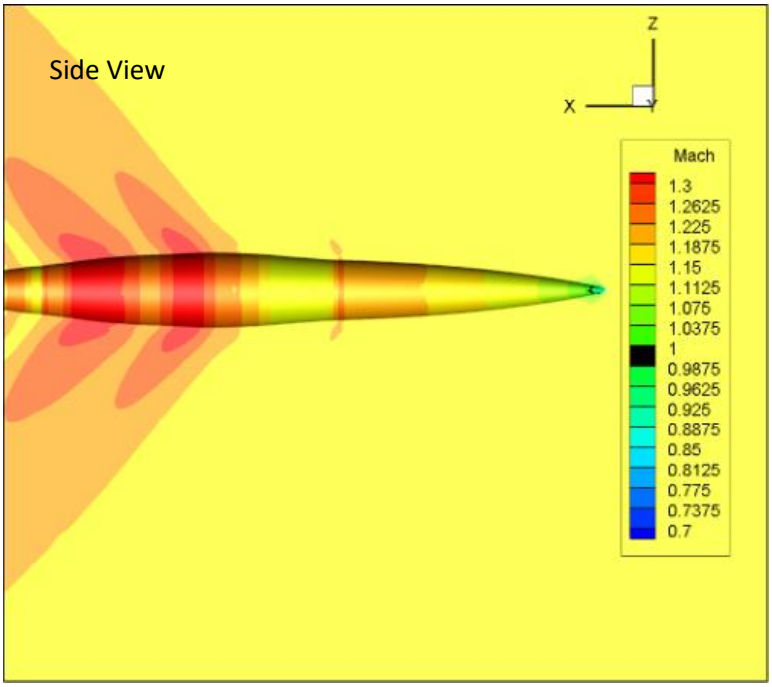

Figure 126. Swept Wing, Curved Comparable Body M=1.2 Solution

The curved comparable body case behaves similarly to many of the other comparable body cases in that the shock begins aft of the point of maximum cross-sectional area and moves forward of it when the freestream Mach becomes supersonic. This solution is not very different in comparison to the cylindrical body case.

Once again, no angles coincide for this geometry. The subsonic solutions are once again fairly accurately predicted by Küchemann's *CP** equation. The supersonic solutions are also once again not able to be predicted given that all the *CP* values obtained are positive (before and after the shock).

There are many similarities between the solutions for the geometries presented by Whitcomb. In terms of Mach cone angles correlating with measured shock angles, there appears to be no consistent correlation. As for the prediction capabilities of Küchemann's *CP** equation, it appears to predict the development of shocks in subsonic conditions but does not appear to do so for any supersonic conditions. However, this is an odd occurrence as none of the Mach values before the shocks develop are greater than the freestream Mach number at supersonic conditions. This would imply positive pressure coefficient values, which the table used here does not cover. This pattern is consistent for all geometries shown arguing in favor of the equation's prediction capabilities at least for a subsonic range of solutions.

In regard to amount of shocks observed and their observed complexity, it would seem that the indented bodies for the unswept and delta cases produce more shocks than the base bodies and in more complex patterns. Along with this, neither of these indented body cases seem to have the shocks disappear at higher Mach numbers like the other

solutions demonstrate. In fact, the shock that does remain in these indented solutions only appears to grow stronger as the freestream Mach number is increased. The only indented case that appears to simplify the surface flow is the swept wing case. In this solution, there is almost never a shock and where there are possible shocks, the intensity is very weak demonstrated by the local Mach number drop over it. These behaviors are an interesting point to compare with the total drag measurements shown in Chapter 5.

CHAPTER 7

VERIFICATION OF RESULTS

There were several questions raised during the production of solutions from SU2 about the reliability of the results because of the complexity of the steps taken. Some of these were answered with solutions such as the boat-tails at the end of the geometries to help with convergence. The two main questions that arose about the accuracy of the results are whether the volume grid has enough points and whether the Mach angles off certain components on the body would cause a contamination of flow on the body downstream. There was particular concern about the swept wing, cylindrical body as the wing-tip could alter the flow downstream. These concerns were addressed with relatively simple solutions.

First, to determine whether a grid had enough points, a grid convergence study was performed for the unswept wing, cylindrical body geometry at a Mach number of 1.2. Three grids were used to determine whether a grid was accurate enough. The grids had total point numbers of ~500,000, ~1,000,000, and ~3,600,000 points. To decide a grid was accurate enough, the grids above and below in size would need to produce values within +/-0.5% in difference. After performing this study, the results in Table 4 were produced showing that the grid size of ~1,000,000 for this model was accurate enough. All other models, however, yielded grid sizes with far more points than the unswept wing, cylindrical body case. So, there is no concern about the reliability of the results from any of the other geometries. Their grid sizes are listed in Table 5 below.

Table 4. Grid Convergence Study of Unswept Wing Cylindrical Body at M=1.2

# of Points	CD0	% Difference
506,108	0.01235	-0.31%
1,009,115	0.01239	
3,624,555	0.01242	0.23%

Table 5. Grid Sizes for Observed Geometries

Model	# of Points
Unswept Wing, Cylindrical Body	1,009,115
Unswept Wing, Comparable Body	3,447,111
Unswept Wing, Indented Body	3,741,469
Delta Wing, Cylindrical Body	3,622,030
Delta Wing, Comparable Body	3,462,535
Delta Wing, Indented Body	3,713,519
Swept Wing, Cylindrical Body	3,853,534
Swept Wing, Comparable Body	3,525,580
Swept Wing, Indented Body	3,884,699
Swept Wing, Curved Body	3,123,678
Swept Wing, Curved Comparable Body	2,491,163

The downstream flow contamination was dealt with by making another model of the swept wing, cylindrical body geometry with an additional three body lengths after the end of the original model. The idea here was that if there were to be any downstream flow contamination, its impact would be reflected in the drag value produced in comparison to the original body. This model was then run at most of the same Mach numbers that the original body was run at and the results of this are shown in comparison in Fig. (127) below. As can be seen there, the two models produce almost exactly the same results and therefore there is no concern about downstream contamination of the flow.

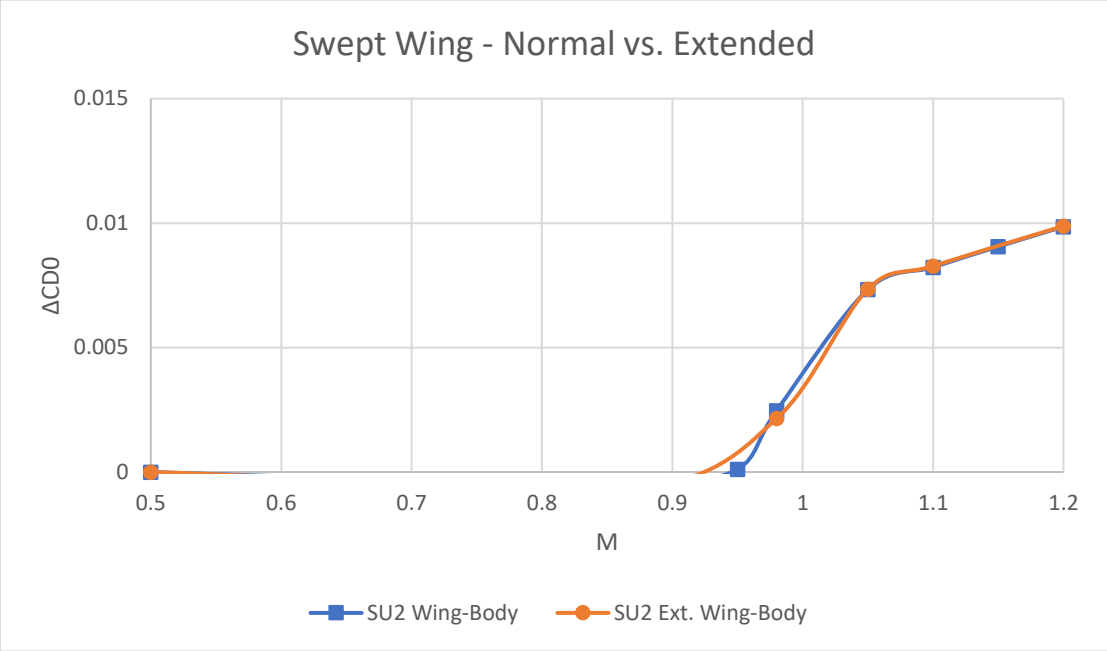

Figure 127. Original Swept Wing, Cylindrical Body & Extended Body Comparison

CHAPTER 8

CONCLUSION

To conclude this report, the questions presented in Chapter 1 are addressed beginning with: 1) asking if the Transonic Area Rule achieves what it claims it does 2) seeking any telltale signs of transonic shock formation that might be found in purely subsonic solutions and 3) determining if any shocks encountered are able to be predicted by Küchemann's *CP** predictions.

a. Does an equivalent body of revolution produce the same transonic drag rise characteristics as the original wing-body combination?

If the Transonic Area Rule were exact, an equivalent body of revolution would produce the same transonic drag rise characteristics as the original wing-body combination. The Transonic Area Rule is clearly not exact based on the results from Chapter 5. It was shown that none of the geometries appear to have had their comparable bodies and base bodies coincide in terms of their drag rise characteristics. In fact, the unswept wing and delta wing cases appear to have had comparable bodies that produced even more drastic drag rise characteristics than the base bodies. The two swept wing cases, however, had comparable bodies that produced a reduced drag rise in comparison. The swept wing behavior is relatively unsurprising in comparison to Whitcomb's results as they too demonstrated this. The interesting trend shown in the SU2 results in comparison to Whitcomb's results are that three of the four base body cases (i.e. not the swept wing, curved body) seem to match data quite well. In all three of these cases, SU2 seems to

have done a fairly good job of matching Whitcomb's data. The comparable bodies of revolution, however, appear to be skewed from Whitcomb's data in all cases.

Using other common wave drag estimation methods to help identify some consistency proved to be somewhat helpful. As discussed before, EDET approximates this wave drag by using empirical data, but appears to overpredict in two of the three cases it was used in. The only exception to this behavior is the delta wing, cylindrical body case where its approximation at Mach numbers between 1 and 1.1 appear to coincide somewhat well with the SU2 results for the base body. The Harris Wave Drag program, on the other hand, seems to have done consistently well at matching data with the SU2 base body data for all cases. It should be noted, however, that the unswept wing and delta wing cases only seem to have data start to coincide at Mach numbers 1.1 and above. Thus, the SU2 solutions match Whitcomb's base body cases fairly well and D2500 follows right behind. EDET overpredicts in most cases and does not coincide with any data particularly well. In all cases the comparable bodies of revolution do not appear to coincide with the base body solutions from SU2.

With these behaviors in mind, it appears that this report would argue that the Transonic Area Rule's first claim does not hold true based on the methods used here. However, it should be noted that the D2500 program makes use of the Supersonic Area Rule, an extension to the Transonic Area Rule. The comparable bodies made by the Supersonic Area Rule, then seem to match the base body data fairly well at Mach numbers 1.1 and slightly greater. Given the results from the surface pressure coefficient measurements as well, it would appear that the unswept wing and delta wing cases have

comparable bodies that yield even stronger shocks than on the base bodies. This may be cause for the increased drag rise.

b. Does indenting the fuselage of a wing-body combination reduce the transonic drag rise experienced in a meaningful manner?

Indenting the body according to the Transonic Area Rule, however, does appear to function similar to how Whitcomb described in terms of reduced drag rise. Though the SU2 indented body does not match Whitcomb's all that well, the comparison between base body and indented body SU2 data shows that over a range of Mach numbers around 1, there is a reduction in drag rise. The exception to this is the swept wing indented body case as the reduction appears to carry on even until the Mach 1.2 case. In the unswept wing and delta wing cases, this reduction stops between a Mach of 1.05 and 1.1 where the indented bodies instead start producing greater drag increments than the base bodies. Thus, SU2 does seem to argue in favor of Whitcomb's advised indentations reducing the transonic drag rise of geometries. However, SU2 does not show this reduction for as high of Mach numbers and the reduction does not seem to be as intense as Whitcomb's.

c. Does indenting the fuselage of a wing-body combination reduce the number of shocks experienced and the intensity of them?

The final claim of the Transonic Area Rule is that the indented bodies reduce the transonic drag rise by reducing the number of shocks, decreasing their intensity, and reducing the complexity of shock patterns. The surface Mach number plots from Chapter 6 show this to not be true for the unswept wing and delta wing cases. In both of these

cases there appear to be more shocks on the body with a far more complex pattern than in the base body case. Along with this, the strength of the shocks produced at the indentation (as demonstrated by the Mach number drop intensities before and after the shock) are stronger than almost any shocks produced on the base bodies. As the freestream Mach number is increased, the base bodies appear to shed their shocks whereas the indented bodies appear to keep the shocks at the indentation and only seem to grow in strength. For the swept wing case, however, almost all of the shocks seem to disappear for any of the Mach number solutions observed (except for the bow shock at the nose of the body). This is interesting to see because the comparable body of revolution demonstrates shock development like the base body does. But once this area development is removed from the body to "cancel" the cross-sectional area added by the wings, the shocks seem to disappear. The flow patterns appear to be similar to the base body case, but no shocks develop. So, although there does appear to be a reduction in the transonic drag rise and a more linear rise at that for the indented bodies, Whitcomb's claim does not appear to hold true for the unswept and delta wing cases. The swept wing case, however, does argue this claim quite well. Given that schlieren surveys are used in Whitcomb's report, this may not be all that surprising and the limited technology of the time may not have allowed as in depth of a look into shock patterns.

d. Are there any telltale signs of shock formation in subsonic solutions?

In terms of telltale signs of shock development from subsonic solutions, there doesn't appear to be much happening. Given how drastically the isobar patterns change from solution to solution, the subsonic isobar patterns do not tell us much more than the

assumed general shape of the isobar patterns at higher Mach number solutions. For example, looking at where the first shock develops in the delta wing, cylindrical body case (Mach 0.95 solution), one can assume this is where a shock would first develop based on the patterns in the Mach 0.5 solution. However, this is purely qualitative and has no real backing. Instead, it may be possible to get an approximate idea of what the shock angle may be whenever it develops based on the subsonic solution isobar patterns. Perhaps more in-depth analysis of these solutions would provide more insight.

e. Are the shocks encountered able to be predicted by Küchemann's *CP** predictions?

Küchemann's *CP** equation does appear to do a good job of predicting shock formation at the subsonic solutions. However, the interesting behavior for these is that the shock formations do not appear to coincide with any particular sweep angle consistently nor the expected Mach cone angle for either the freestream or local Mach numbers. As was demonstrated from Schlichting, when the leading or trailing edge sweeps interact with the expected Mach lines to develop shocks on the wing surface, the shocks are expected to coincide with the expected Mach cone angle[12]. In all cases within this report, shock patterns did not coincide with any expected sweep angle or Mach cone angle. The local pressure coefficient values measured around the shocks fitted to the shock angles in the *CP** equation, however, do seem to agree. Thus, it seems it could be possible to get a general idea of what a shock angle may develop to be from a subsonic solution and determine critical pressure coefficient values fitted to these approximations.

To summarize, it would appear Whitcomb's claim about the Transonic Area Rule comparable bodies of revolution producing similar drag rise characteristics to the base geometries is not backed by CFD solutions or Supersonic Area Rule comparable bodies of revolution (from Harris Wave Drag program). The reduction of transonic drag rise by indenting the body at the wing-body junction does appear to be true, though not as dramatically as Whitcomb's data shows. The complexity of shock patterns does not appear to be simplified due to the indentation, actually becoming more numerous, complex, and intense with the indentation in some cases. For the swept wing case, however, there is a strong claim in favor of this. It would appear that the Transonic Area Rule may favor longitudinally longer wings or something of the like to make the indentation seem less severe in its cross-sectional area change. The subsonic solutions shown seem like they may provide a good idea for approximating at least shock angles for future Mach solutions (more analysis is required). Finally, Küchemann's *CP** equation does appear to yield accurate critical pressure coefficient values based on measured pressure coefficient values for subsonic solutions. At supersonic solutions, however, the predictive capabilities are no longer there. Thus, it appears to do well at predicting initial development of shocks fitted to shock angles rather than Mach cone angles or geometric feature sweeps.

REFERENCES

[1]Ames Research Staff, “Equations, Tables, and Charts for Compressible Flow,” NACA 1135.

[2]Area rule. (2021, January 22). Retrieved April 05, 2021, from https://en.wikipedia.org/wiki/Area_rule

[3]Convair F-102 Delta Dagger. (2021, April 01). Retrieved April 05, 2021, from https://en.wikipedia.org/wiki/Convair_F-102_Delta_Dagger

[4]Feagin, R.C. and Morrison, W.D., “Delta Method, An Empirical Drag Buildup Technique,” NASA CR 151971, December 1978.

[5]Governing equations in su2. (n.d.). Retrieved April 05, 2021, from https://su2code.github.io/docs_v7/Theory/

[6]Harris, R.V., Jr., “An Analysis and Correlation of Aircraft Wave Drag,” NASA TM X-947, March 1964.

[7]Kirkman, J.J. and Takahashi, T.T., "Critical Mach Number Prediction on Swept Wings," AIAA 2017-0266, 2017.

[8]Küchemann, D., “The Aerodynamic Design of Aircraft,” AIAA, Reston, VA, 2012.

[9]Kulfan, B., “A New Supersonic Wing Far-Field Composite Element Wave Drag Optimization Method, ‘FCE’,” AIAA 2008-132, 2008.

[10]Mesh and grid generation software for CFD. (n.d.). Retrieved April 05, 2021, from https://www.pointwise.com/pointwise/software

[11]Neumark, S., “Critical Mach Numbers for Thin Untapered Swept Wings at Zero Incidence,” ARC R&M 2821, 1954

[12]Schlichting, H. and Truckenbrodt, E., “Aerodynamics of the Airplane,” McGraw-Hill. New York, 1979.

[13]Takahashi, T.T., Aircraft Performance and Sizing, Vol. I: Fundamentals of Aircraft Performance, Momentum Press, 2016.

[14]Takahashi, T.T., Aircraft Performance and Sizing, Vol. II: Applied Aerodynamic Design, Momentum Press, 2016.

[15]Von Kármán, T.H., “Compressibility Effects in Aerodynamics,” J. of Aeronautical Sciences, Vol. VIII, No. 9, 1941, pp. 337-56.

[16]Whitcomb, R.T., “A Study of the Zero-Lift Drag-Rise Characteristics of Wing-Body Combinations Near the Speed of Sound,” NACA TR 1273, 1952.

[17]Whitcomb, R. T., “Some Considerations Regarding the Application of the Supersonic Area Rule to the Design of Airplane Fuselages,” NACA RM L56E23a, 1956.

APPENDIX A

WHITCOMB FUSELAGE ORDINATES

TABLE I.—ORDINATES OF BASIC BODY

[All dimensions are in inches]

Cylindrical body	
Station	Radius
0	0
.225	.104
.338	.134
.563	.193
1.125	.325
2.250	.542
3.375	.726
4.500	.887
6.750	1.167
9.000	1.391
11.250	1.559
13.500	1.683
15.750	1.770
18.000	1.828
20.250	1.864
22.500	1.875
43.000	1.875

Curved body	
Station	Radius
0	0
.200	.092
.300	.119
.500	.171
1.000	.289
2.000	.482
3.000	.645
4.000	.788
6.000	1.037
8.000	1.236
10.000	1.386
12.000	1.496
14.000	1.573
16.000	1.625
18.000	1.657
20.000	1.667
22.000	1.652
24.000	1.610
26.000	1.537
28.000	1.425
30.000	1.251
32.000	1.010
32.605	0.940

TABLE III.—ORDINATES OF INDENTED BODIES

[All dimensions are in inches]

With unswept wing	
Station	Radius
22.500	1.875
24.000	1.873
24.500	1.857
25.000	1.807
25.500	1.720
26.000	1.622
26.500	1.521
27.000	1.476
27.500	1.470
28.000	1.487
28.500	1.533
29.000	1.580
29.500	1.642
30.000	1.664
30.500	1.710
31.000	1.743
31.500	1.773
32.000	1.812
32.500	1.837
33.000	1.856
33.500	1.868
34.000	1.875
43.000	1.875

With delta wing	
Station	Radius
22.500	1.875
24.000	1.875
24.500	1.868
25.000	1.856
25.500	1.837
26.000	1.812
26.500	1.773
27.000	1.743
27.500	1.710
28.000	1.664
28.500	1.642
29.000	1.580
29.500	1.533
30.000	1.487
30.500	1.470
31.000	1.476
31.500	1.521
32.000	1.622
32.500	1.720
33.000	1.807
33.500	1.857
34.000	1.875
43.000	1.875

With swept wing	
Station	Radius
22.500	1.875
23.125	1.875
24.125	1.842
25.125	1.787
26.125	1.710
27.125	1.641
28.125	1.592
29.125	1.560
30.125	1.572
31.125	1.611
32.125	1.640
33.125	1.656
34.125	1.688
35.125	1.740
36.125	1.802
37.125	1.850
38.125	1.874
38.375	1.875
43.000	1.875

TABLE II.—ORDINATES OF COMPARABLE BODIES OF REVOLUTION

[All dimensions are in inches]

Comparable to unswept wing on cylindrical body	
Station	Radius
22.500	1.875
23.500	1.875
24.500	1.892
25.000	1.939
25.500	2.012
26.000	2.087
26.500	2.155
27.000	2.182
27.500	2.185
28.000	2.174
28.500	2.145
29.000	2.113
29.500	2.086
30.000	2.054
30.500	2.019
31.000	1.992
31.500	1.968
32.000	1.934
32.500	1.911
33.000	1.894
33.500	1.882
34.000	1.875
43.000	1.875

Comparable to delta wing on cylindrical body	
Station	Radius
22.500	1.875
24.000	1.875
24.500	1.882
25.000	1.894
25.500	1.911
26.000	1.934
26.500	1.968
27.000	1.992
27.500	2.019
28.000	2.054
28.500	2.086
29.000	2.113
29.500	2.145
30.000	2.174
30.500	2.185
31.000	2.182
31.500	2.155
32.000	2.087
32.500	2.012
33.000	1.939
33.500	1.892
34.500	1.875
43.000	1.875

Comparable to swept wing on cylindrical body	
Station	Radius
22.500	1.875
23.125	1.875
24.125	1.907
25.125	1.957
26.125	2.024
27.125	2.080
28.125	2.117
29.125	2.143
30.125	2.135
31.125	2.107
32.125	2.083
33.125	2.071
34.125	2.045
35.125	2.001
36.125	1.946
37.125	1.899
38.125	1.876
38.375	1.875
43.000	1.875

Comparable to swept wing on curved body	
Station	Radius
14.000	1.573
14.300	1.580
14.625	1.595
15.625	1.670
16.625	1.747
17.625	1.836
18.625	1.903
19.625	1.943
20.625	1.966
21.625	1.949
22.625	1.901
23.625	1.857
24.625	1.822
25.625	1.756
26.625	1.664
27.625	1.545
28.625	1.413
29.625	1.292
29.875	1.260
30.000	1.251
32.000	1.010
32.605	0.940

APPENDIX B

TABULATED SU2 CD_0 DATA

Unswept Wing -Cyl. Body			Unswept Wing -Comp. Body			Unswept Wing - Ind. Body		
Mach #	CD0	dCD0	Mach #	CD0	dCD0	Mach #	CD0	dCD0
0.5	0.001898872	0	0.5	0.0012	0	0.5	0.002139	0
0.88	0.002371128	0.000472257	0.88	0.002038	0.00083834	0.88	0.002554	0.000415
0.95	0.005524302	0.00362543	0.95	0.007456	0.00625671	0.95	0.004891	0.002752
0.98	0.009138889	0.007240018	0.98	0.011423	0.01022336	0.98	0.007199	0.005059
1.05	0.012554291	0.010655419	1.05	0.01429	0.01309046	1.05	0.011681	0.009542
1.1	0.01275654	0.010857668	1.1	0.014719	0.01351943	1.1	0.014586	0.012446
1.15	0.012657689	0.010758817	1.15	0.014591	0.01339179	1.15	0.016501	0.014362
1.2	0.012388874	0.010490003	1.2	0.013937	0.01273737	1.2	0.017404	0.015265

Delta Wing - Cyl. Body			Delta Wing - Comp. Body			Delta Wing - Ind. Body		
Mach #	CD0	dCD0	Mach #	CD0	dCD0	Mach #	CD0	dCD0
0.5	0.001427	0	0.5	0.0012201	0	0.5	0.002268	0
0.88	0.001778	0.000351	0.88	0.00251793	0.001297831	0.88	0.002744	0.00047647
0.95	0.007518	0.006091	0.95	0.0101999	0.008979796	0.95	0.005054	0.00278612
0.98	0.011705	0.010278	0.98	0.01401074	0.012790641	0.98	0.007129	0.00486124
1.05	0.012757	0.01133	1.05	0.01507035	0.013850247	1.05	0.011008	0.00874065
1.1	0.011652	0.010225	1.1	0.01399501	0.012774911	1.1	0.013062	0.01079476
1.15	0.010935	0.009508	1.15	0.01303721	0.011817109	1.15	0.014483	0.01221516
1.2	0.010435	0.009008	1.2	0.01225871	0.011038608	1.2	0.015399	0.01313117

Swept Wing -Cyl. Body			Swept Wing Cyl. Body - Comp.			Swept Wing - Ind. Body		
Mach #	CD0	dCD0	Mach #	CD0	dCD0	Mach #	CD0	dCD0
0.5	0.005264	0	0.5	0.000833	0	0.5	0.00528479	0
0.88	0.004665	-0.0006	0.88	0.000828	-4.8E-06	0.88	0.00461062	-0.00067
0.95	0.005375	0.000111	0.95	0.001412	0.000579	0.95	0.00489023	-0.00039
0.98	0.007732	0.002468	0.98	0.002506	0.001673	0.98	0.00540639	0.000122
1.05	0.012597	0.007333	1.05	0.006673	0.00584	1.05	0.00918256	0.003898
1.1	0.013488	0.008224	1.1	0.006599	0.005766	1.1	0.01094898	0.005664
1.15	0.014318	0.009055	1.15	0.006341	0.005508	1.15	0.01264344	0.007359
1.2	0.015117	0.009853	1.2	0.006131	0.005298	1.2	0.01447165	0.009187

Swept Wing -Cur. Body			Swept Wing Cur. Body - Comp.			Swept Wing Cyl. Ext. Body		
Mach #	CD0	dCD0	Mach #	CD0	dCD0	Mach #	CD0	dCD0
0.5	0.006627	0	0.5	0.002334	0	0.5	0.005188	0
0.88	0.00645	-0.00017706	0.88	0.002727	0.000393	0.88	0.004623	-0.00057
0.95	0.008343	0.00171592	0.95	0.004182	0.001848	0.98	0.007338	0.00215
0.98	0.014281	0.00765386	0.98	0.00832	0.005986	1.05	0.012533	0.007345
1.05	0.018766	0.01213908	1.05	0.012698	0.010364	1.1	0.013463	0.008275
1.1	0.018941	0.01231341	1.1	0.01213	0.009796	1.2	0.015069	0.009881
1.15	0.019211	0.01258379	1.15	0.011622	0.009288			
1.2	0.019604	0.01297693	1.2	0.011144	0.00881			

APPENDIX C

SU2 INPUT CFG FILE

```
% ------------ DIRECT, ADJOINT, AND LINEARIZED PROBLEM DEFINITION ------------%
%
% Physical governing equations (EULER, NAVIER_STOKES,
%                               WAVE_EQUATION, HEAT_EQUATION, FEM_ELASTICITY,
%                               POISSON_EQUATION)
SOLVER= EULER
%
% Mathematical problem (DIRECT, CONTINUOUS_ADJOINT)
MATH_PROBLEM= DIRECT
%
% Restart solution (NO, YES)
RESTART_SOL= NO

% ------------------- COMPRESSIBLE FREE-STREAM DEFINITION --------------------%
%
% Mach number (non-dimensional, based on the free-stream values)
MACH_NUMBER= 1.05
%
% Angle of attack (degrees)
AOA= 0.0
%
% Free-stream pressure (101325.0 N/m^2 by default, only Euler flows)
FREESTREAM_PRESSURE= 101325.0
%
% Free-stream temperature (288.15 K by default)
FREESTREAM_TEMPERATURE= 288.15

% ---------------------- REFERENCE VALUE DEFINITION --------------------------%
%
% Reference origin for moment computation
REF_ORIGIN_MOMENT_X = 0.00
REF_ORIGIN_MOMENT_Y = 0.00
REF_ORIGIN_MOMENT_Z = 0.00
%
% Reference length for pitching, rolling, and yawing non-dimensional moment
REF_LENGTH= 1
%
% Reference area for force coefficients (0 implies automatic calculation)
REF_AREA= 0.046380994
%
% Flow non-dimensionalization (DIMENSIONAL, FREESTREAM_PRESS_EQ_ONE,
%                              FREESTREAM_VEL_EQ_MACH, FREESTREAM_VEL_EQ_ONE)
REF_DIMENSIONALIZATION= FREESTREAM_PRESS_EQ_ONE

% ---------------------- BOUNDARY CONDITION DEFINITION -----------------------%
%
% Marker of the Euler boundary (0 = no marker)
MARKER_EULER= ( body, sting )
%
% Marker of the far field (0 = no marker)
MARKER_FAR= ( farfield )
```

```
%
% Marker of Symmetry wall
MARKER_SYM = ( symm )

% ------------------------ SURFACES IDENTIFICATION ----------------------------%
%
% Marker of the surface which is going to be plotted or designed
MARKER_PLOTTING= ( body, sting )
%
% Marker of the surface where the functional (Cd, Cl, etc.) will be evaluated
MARKER_MONITORING= ( body )

% ------------- COMMON PARAMETERS DEFINING THE NUMERICAL METHOD ---------------%
%
% Numerical method for spatial gradients (GREEN_GAUSS, WEIGHTED_LEAST_SQUARES)
NUM_METHOD_GRAD= GREEN_GAUSS
%
% Courant-Friedrichs-Lewy condition of the finest grid
CFL_NUMBER= 10.0
%
% Adaptive CFL number (NO, YES)
CFL_ADAPT= YES
%
% Parameters of the adaptive CFL number (factor down, factor up, CFL min value,
%                                        CFL max value )
CFL_ADAPT_PARAM= ( 0.5, 1.5, 1.0, 100.0 )
%
% Runge-Kutta alpha coefficients
RK_ALPHA_COEFF= ( 0.66667, 0.66667, 1.000000 )
%
% Number of total iterations
ITER= 1000

% ------------------------ LINEAR SOLVER DEFINITION ---------------------------%
%
% Linear solver for the implicit (or discrete adjoint) formulation (LU_SGS,
%                                                 SYM_GAUSS_SEIDEL, BCGSTAB, GMRES)
LINEAR_SOLVER= FGMRES
%
% Preconditioner of the Krylov linear solver (NONE, JACOBI, LINELET, LUSGS)
LINEAR_SOLVER_PREC= LU_SGS
%
% Min error of the linear solver for the implicit formulation
LINEAR_SOLVER_ERROR= 1E-4
%
% Max number of iterations of the linear solver for the implicit formulation
LINEAR_SOLVER_ITER= 4


% --------------------- FLOW NUMERICAL METHOD DEFINITION ----------------------%
% Convective numerical method (JST, LAX-FRIEDRICH, ROE-1ST_ORDER,
%                              ROE-2ND_ORDER)
```

```
%                              ROE-2ND_ORDER)
CONV_NUM_METHOD_FLOW= ROE
%
% Monotonic Upwind Scheme for Conservation Laws (TVD) in the flow equations.
%           Required for 2nd order upwind schemes (NO, YES)
MUSCL_FLOW= NO
% Slope limiter (VENKATAKRISHNAN)
SLOPE_LIMITER_FLOW= VENKATAKRISHNAN
%
% 2nd and 4th order artificial dissipation coefficients
JST_SENSOR_COEFF= ( 0.5, 0.02 )
%
% Time discretization (RUNGE-KUTTA_EXPLICIT, EULER_IMPLICIT, EULER_EXPLICIT)
TIME_DISCRE_FLOW= EULER_IMPLICIT

% ---------------------------- CONVERGENCE PARAMETERS ---------------------------%
% Convergence criteria (CAUCHY, RESIDUAL)
%
CONV_CRITERIA= RESIDUAL
%
%
% Min value of the residual (log10 of the residual)
CONV_RESIDUAL_MINVAL= -11
%
% Start Cauchy criteria at iteration number
CONV_STARTITER= 10
%
% Number of elements to apply the criteria
CONV_CAUCHY_ELEMS= 100
%
% Epsilon to control the series convergence
CONV_CAUCHY_EPS= 1E-6

% ------------------------- INPUT/OUTPUT INFORMATION --------------------------%
%
% Mesh input file
MESH_FILENAME= SW_Ext.su2
%
% Mesh input file format (SU2, CGNS, NETCDF_ASCII)
MESH_FORMAT= SU2
%
% Mesh output file
MESH_OUT_FILENAME= mesh_out.su2
%
% Restart flow input file
SOLUTION_FILENAME= solution_flow.dat
%
% Restart adjoint input file
SOLUTION_ADJ_FILENAME= solution_adj.dat
%
% Output tabular format (CSV, TECPLOT)
```

```
TABULAR_FORMAT= TECPLOT
%
% Output file convergence history (w/o extension)
CONV_FILENAME= history
%
% Output file restart flow
RESTART_FILENAME= restart_flow.dat
%
% Output file restart adjoint
RESTART_ADJ_FILENAME= restart_adj.dat
%
% Output file flow (w/o extension) variables
VOLUME_FILENAME= flow
%
% Output file adjoint (w/o extension) variables
VOLUME_ADJ_FILENAME= adjoint
%
% Output Objective function gradient (using continuous adjoint)
GRAD_OBJFUNC_FILENAME= of_grad.dat
%
% Output file surface flow coefficient (w/o extension)
SURFACE_FILENAME= surface_flow
%
% Output file surface adjoint coefficient (w/o extension)
SURFACE_ADJ_FILENAME= surface_adjoint
%
% Writing solution file frequency
WRT_SOL_FREQ= 1000
%
% Writing solution file frequency for physical time steps (dual time)
WRT_SOL_FREQ_DUALTIME= 1
%
% Writing convergence history frequency
WRT_CON_FREQ= 1
%
% Writing convergence history frequency (dual time, only written to screen)
WRT_CON_FREQ_DUALTIME= 10
%
% Output rind layers in the solution files
WRT_HALO= NO
%
% Screen output
SCREEN_OUTPUT= (INNER_ITER, RMS_DENSITY, RMS_ENERGY, LIFT, DRAG)
%
% Output files
OUTPUT_FILES = (RESTART, SURFACE_TECPLOT, TECPLOT)
% History Output
%
HISTORY_OUTPUT = (ITER, RMS_RES, AERO_COEFF)
```